Faculty of Mathematics and Physics
Charles University, Prague

Measurement and QCD analysis of inclusive dijet mass cross section in $p\bar{p}$ collisions at $\sqrt{s} = 1.96\,\mathrm{TeV}$

Alexander Kupčo

Doctoral thesis

July, 2003

Measurement and QCD analysis of inclusive dijet mass cross section in $p\bar{p}$ collisions at $\sqrt{s} = 1.96$ TeV

Alexander Kupčo

Institute of Physics
Academy of Sciences of the Czech Republic

Supervisor: Professor Jiří Chýla

Abstract

The thesis presents the first DØ measurement of inclusive dijet mass cross section in $p\bar{p}$ collisions at $\sqrt{s} = 1.96$ TeV using $48\,\mathrm{pb}^{-1}$ of Run II data. The error is dominated by the systematics coming from the error on jet energy scale. A good agreement between data and NLO QCD predictions is found. The dijet sample is also used to study the difference in azimuthal angle $\Delta\phi$ between the two leading jets. Preliminary results on measurement of the $\Delta\phi$ distributions in four dijet mass bins are presented. It is shown that $\mathcal{O}(\alpha_S^3)$ perturbative QCD predictions fail to describe the distributions in the regions $\Delta\phi \sim \pi$ and $\Delta\phi < 2\pi/3$.

Prohlašuji, že jsem disertační práci napsal samostatně a výhradně s použitím citovaných pramenů. Souhlasím se zapůjčováním práce.

V Praze, dne 7. července 2003 Alexander Kupčo

to my parents Alexandra Kupčová and Vladimír Kupčo
and to Jana Kašparová

Acknowledgements

The thesis would not be possible without work of several hundreds of people involved in the DØ experiment. However, in the collaboration of this size, it is impossible to mention all the people that were contributing to it. I would like to thank Michael Begel, John Krane, Christophe Royon, Markus Wobisch, and Marek Zieliński. They were guiding, and sometimes even pushing, the analysis at its various stages.

I want to thank my supervisor Jiří Chýla. His help, especially with QCD theory and its history, was invaluable. I'm also grateful for the opportunity to be involved in the DØ experiment. It would not be possible without consistent support I got from the Institute of Physics, Academy of Sciences of the Czech Republic, Prague. The work was also supported in part by the project LN00A006 of the Ministry of Education of the Czech Republic, by the NATO Science Fellowships program, and by a common grant of the National Science Foundation and the Grant Agency of the Czech Republic.

Contents

1 Introduction **1**

2 Aspects of perturbative QCD **5**

2.1 Ultra-violet divergences and running α_S 8

2.2 Treatment of infrared (IR) singularities 10

2.3 QCD improved parton model 14

3 The DØ detector **19**

3.1 Calorimeter 21

3.1.1 Central calorimeter (CC) 24

3.1.2 End-cap calorimeter (EC) 25

3.1.3 Inter Cryostat Detector (ICD) 25

3.1.4 Calorimeter readout and treatment of hot cells 26

4 Hadron final states - jets **29**

4.1 DØ Run II cone algorithm 33

4.2 Cone jets at NLO QCD – R_{sep} parameter 38

5 Jet energy scale **39**

6 Luminosity **44**

6.1 Structure of the Tevatron beam 44

6.2 Luminosity Monitor 44

6.3 Method of luminosity measurement 45

6.4 Normalisation uncertainty 50

7 Jet triggers **51**

7.1 Trigger turn-on points 54

8 Data sample **57**

9 Event selection and associated efficiencies **59**

9.1 Central dijet sample 59

9.2 Jet identification criteria 60
9.2.1 Efficiencies of jet selection criteria 67
9.3 Vertex cut 73
9.3.1 Vertex cut efficiency 76
9.4 Cut on missing transverse energy 77
9.5 Jet distributions in the central dijet sample 81
9.6 Instantaneous luminosity profile 85

10 Jet and dijet mass resolutions 89
10.1 Jet transverse momentum resolution 90
10.1.1 Data sample and event selection criteria 91
10.1.2 Raw jet p_T resolution 93
10.1.3 Soft radiation correction 94
10.1.4 Particle jet imbalance 99
10.1.5 Jet resolution - final result 100
10.1.6 Closure test 103
10.2 Jet angular resolution 104
10.3 Dijet mass resolution 107

11 Inclusive dijet mass cross section 110
11.1 Master formula 110
11.2 Raw dijet mass spectrum – trigger turn-on points 110
11.3 Calorimeter east-west asymmetry 112
11.4 Unsmearing method 114
11.5 Results 119
11.6 NLO calculation of the dijet mass cross section 125
11.7 Comparison with theory 128

12 $\Delta\phi$ distribution 130

13 Summary 134

References 135

1 Introduction

Hadron-hadron interactions with jets with high transverse momentum probe the structure of matter and space at small distances. The Tevatron, as the world's highest energy hadron-hadron collider, provides an excellent opportunity to study such interactions. The collider is located in Fermi National Accelerator Laboratory in Batavia, Illinois. The Tevatron was providing proton and anti-proton beams with energy $E_{\mathrm{beam}} = 900\,\mathrm{GeV}$ during the so called Run Iwhich ended in 1996. The Tevatron was upgraded in 1996-2001 and Run II started in March 2001. The main purpose of the upgrade was to increase collider luminosity. Also the beam energy was slightly increased. Nowadays, the Tevatron accelerates protons and anti-protons to 980 GeV. Jets produced at the Tevatron in Run I reached transverse momenta[1] up to $p_T \sim 500\,\mathrm{GeV}$ which roughly corresponds to the distance scale of $10^{-4}\,\mathrm{fm}$. Using high p_T jet data we can test whether the matter really behaves according to the predictions of QCD up to this scale.

The analysis focuses on the measurement of the inclusive dijet mass cross section in $\mathrm{p\bar{p}}$ interactions at center of mass energy $\sqrt{s} = 1.96\,\mathrm{TeV}$. The new data taken with the upgraded DØ detector corresponding to the integrated luminosity of $\mathcal{L} = 48.0\,\mathrm{pb}^{-1}$ are used. The dijet mass spectrum is measured for masses from 115 to about 1000 GeV in the central region of calorimeter. It means that the data test the proton structure roughly in $0.06 \lesssim x \lesssim 0.5$ region, where x is fractional momentum of proton carried by parton, for momentum transfers Q of $10^3\,\mathrm{GeV}^2 \lesssim Q^2 \lesssim 10^5\,\mathrm{GeV}^2$, where $Q \simeq p_T$. Fig. 1 shows the relative contributions of various parton channels to the dijet mass cross section as a function of dijet mass M_{JJ}. The dominant channel at high masses (i.e. also at large x) is the quark-quark channel. The second one, still relatively important, is the quark-gluon channel. Quark distribution functions at large x are well constrained already by the data from lepton deep inelastic scattering experiments. This is not the case of the gluon distribution

[1] Notation with $c = 1$ is used in the text. Consequently, the momentum and mass have the unit of energy.

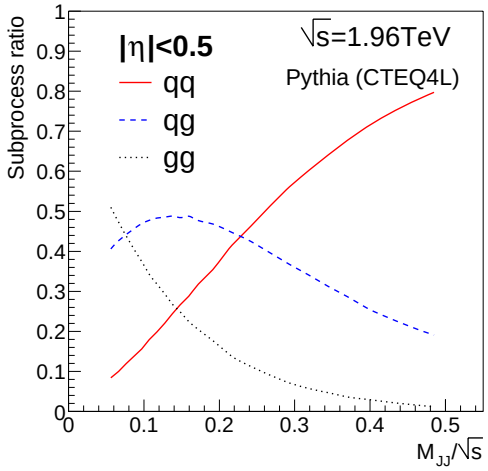

Figure 1: Relative contributions of various parton initial state channels to the dijet mass cross section. Calculated using PYTHIA with CTEQ4L [1] PDF. Renormalization and factorization scales were set to p_T of the scattered parton.

function (see Fig. 7). Constrain at large x from the other experiments is only indirect through the evolution of parton distribution functions (PDF) according to the Altarelli-Parisi evolution equations. Therefore, the high p_T jets data bring us an unique information about the gluon PDF at large x. In fact, the excess of high p_T jets observed by the CDF Collaboration [2] could be partially absorbed by an increase of gluon distribution function at large x without spoiling the agreement of perturbative QCD (pQCD) predictions with the data from the other experiments.

As was pointed out above, events with high p_T jets probe the properties of matter up to 1 TeV scale which makes the data suitable for various searches of new physics. For example, the DØ Run I measurements of the dijet angular distribution [3] and of the dijet mass cross section [4] were used to search for quark compositeness. Depending on the type of the compositeness model, the data excluded the quark substructure up to scales of about 2.5 TeV. On the contrary, the CDF measurement [5] prefers the 1.6 TeV compositeness scale.

Dijet mass spectrum can be also used to search for various heavy resonances such as excited quarks q′ or excited vector bosons W′ and Z′. They would appear in the spectrum as a mass peak. So far, no such resonances were found in the data neither by the UA2 [6], the CDF [7], or the DØ Collaboration [8].

The signals of new physics should appear as an excess of events with high p_T jets in the central region of the calorimeter. New massive objects would be almost in the rest and they would decay isotropically. However, the measurement in the forward region is also important for new searches. The signal would be much smaller compared to the QCD background since the QCD cross section is dominated by the scattering at small angles. But the data in the forward region fix PDFs and thus reduce the uncertainty connected with PDFs.

The question is what improvements can the Run II data bring to the above mentioned Run I results. The small 9% increase of the beam energy translates into the increase in the production of dijet events with mass above 800 GeV by more than factor of 2 as follows from the next-to-leading order (NLO) predictions (Fig. 2). Concerning the statistics of high p_T jets, the current DØ Run II sample used in this analysis with integrated luminosity of $\mathcal{L} = 48.0\,\mathrm{pb}^{-1}$ is therefore already comparable with the Run I dijet sample with luminosity of $\sim 100\,\mathrm{pb}^{-1}$. The plan is to collect in Run II several inverse femtobarns. The statistics of high p_T jets in Run II is expected to be more than order of magnitude larger than in Run I. This will improve our knowledge of proton structure at large x. It will also increase the reach of various searches of new physics. For instance, new Run II measurements on high p_T jets can be used to decide whether the excess of high p_T jets seen by the CDF Collaboration in Run I is real.

The inclusive dijet sample can be also used to test perturbative QCD predictions for multijet processes. In particular, the distribution of the opening angle between the two leading jets $\Delta\phi$ in the plane perpendicular to the beam was measured in this analysis on the same dijet sample as the inclusive dijet mass spectrum. In the case of back-to-back jets ($\Delta\phi \sim \pi$), the $\Delta\phi$ distribu-

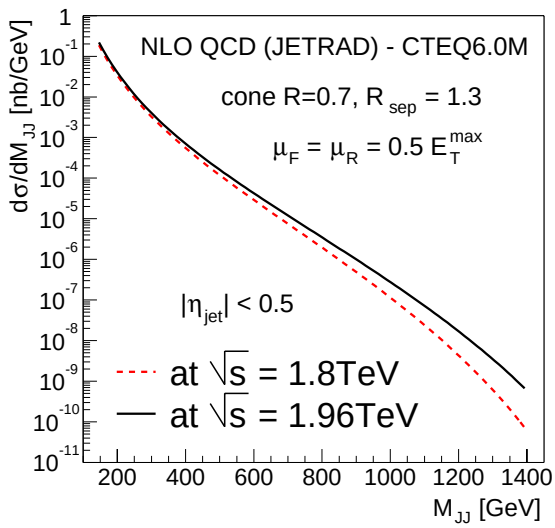

Figure 2: Central inclusive dijet mass cross sections at $\sqrt{s} = 1.8\,\mathrm{TeV}$ and $\sqrt{s} = 1.96\,\mathrm{TeV}$. Calculated with JETRAD [9] using CTEQ6.0M [10] parton distribution functions.

tion is sensitive to the soft parton radiation. QCD resummation calculations of collinear and soft parton emission could be tested on such data. On the other hand, the description of cases when the opening angle between the two jets is small requires taking into account parton final states with four and more partons. For instance, NLO calculations of $2partons \to 3partons$ could be compared with the data in this region of $\Delta\phi$.

2 Aspects of perturbative QCD

A short review of history and birth of Quantum Chromodynamics (QCD) as a theory of strong interaction is given in the beginning of this section. Most of the historical facts were taken from [11, 12] and not from my direct studies of the original papers. Then the basic aspects of perturbative QCD relevant for the next-to-leading order (NLO) calculations are discussed. The focus is put on the concept of running coupling constant, the mechanism of cancellation of infra-red singularities, parton distribution functions, and the general structure of cross section formula.

The term *color* appeared in the context of quark model of hadrons. Quark model, proposed by Zweig [13] and Gell-Mann [14] in 1964, explained the observed hadron spectra as irreducible representations of SU(3) group with a fundamental triplet composed of fermions with spin $\frac{1}{2}$. These three fermions (nowadays called *quarks*) carry a fractional electric charge ($\frac{2}{3}$ or $-\frac{1}{3}$) and a fractional baryon number of $\frac{1}{3}$. In this model, baryons consist of 3 quarks. Baryon multiplets are then obtained from the irreducible decomposition of the tensor product of three quark triplets

$$3 \otimes 3 \otimes 3 = 10 \oplus 8 \oplus 8 \oplus 1\,. \tag{1}$$

Proton, neutron, Λ, Ξ^-, Ξ^0,Σ^0, and $\Sigma^\pm$ form spin $\frac{1}{2}$ baryon octet while baryons Δ, $\Sigma^\star$, $\Xi^\star$, and Ω with spin $\frac{3}{2}$ form decuplet. However, the baryon wave functions in the quark model are fully symmetric which is in conflict with fermion statistics. In order to obey the Pauli principle of exclusion, a new quantum number *color* was introduced[2] . Quarks carry one of the three fundamental colors. Baryons are then constructed as a colorless singlets with fully antisymmetric wave functions in this model.

Introduction of color quantum number solved the problems of fermion statistics. But the model did not explain why the observed hadrons are color

[2]Greenberg used different language of parastatistics in his original work [15]. But his formulation was equivalent to the introduction of the color quantum number.

singlets. It did not also address dynamics connected with the color charge. It was Nambu who proposed in 1965 [16, 17] that the color confinement is caused by the "superstrong" interaction acting between quarks. He even proposed that this force is mediated by an color octet of vector fields that corresponds to the eight generators of $SU_c(3)$ group[3]. Nambu pinpointed the fundamental principle of Quantum Chromodynamics eight years before QCD was formulated.

New insights into the structure of nucleon were revealed by a series of experiments at the Stanford Linear Accelerator Center in late 1960's. Namely, it was the data on deep inelastic scattering (DIS) of electrons on nucleons [18, 19]. The observed weak dependence of structure function F_2 on the size of transfered momentum Q^2 suggested that electrons are scattered on almost free point-like particles. Based on those results, Feynman formulated the *parton model*. According to this model, nucleons consist of point-like particles, called *partons*. He introduced the concept of parton distribution function (PDF) $d_i(x)$ which describes the probability density of finding a parton of type i inside the nucleon that carries fractional momentum x of the nucleon. Nucleons in interactions with large momentum transfer then behave as a flux of free partons. The total cross section is given as an incoherent sum of the cross sections of individual parton scattering on the incoming electron. The structure function F_2 is directly related to the PDFs in the parton model by equation

$$F_2(x) = \sum_i x e_i^2 d_i(x) \,, \tag{2}$$

where e_i is the electric charge of parton of type i. There is no dependence on Q which just reflects the fact that the partons are considered to be free particles. The parton model did not specify which particles the partons actually are. Detailed analyses of the DIS data, namely the relation between F_1 and F_2 structure functions, revealed that the charged partons are fermions

[3]Index c was introduced in order to distinguish SU(3) color symmetry from the SU(3) symmetry in quark model.

with spin $\frac{1}{2}$. The data were also suggesting that a certain amount of nucleon momentum is carried by neutral partons.

The picture of nucleon structure became more confusing. On one side nucleons in DIS look like a bag of point-like particles while according to the quark model of hadrons they consist of three confined quarks. The question was whether there is some relation between quarks and partons. But the most puzzling question was which type of force makes partons to behave almost like a free particles in interactions with large momentum transfer while it prevents them to escape from a nucleon. In other words, the strong interaction must be small at short distances while it must be large enough at the scale of the typical nucleon size ($\sim 1\,\mathrm{fm}$) in order to keep partons inside the nucleon. For comparison, the effective renormalised electron charge in quantum electrodynamics (QED) has a completely different behaviour; it increases with the decreasing distance. It was found by Gross and Wilczek [20] and independently by Politzer [21] in 1973 that such behaviour of coupling constant is present in non-abelian field theories (we will come back to the concept of running coupling constant in section 2.1). Although their calculations were only perturbative, and thus valid only at short distances, the fact that the coupling constant increases with increasing distance gave a hope that such theories could explain confinement. Three months later, Gross and Wilczek published in [22] a Lagrangian which specified the type of strong interaction between quarks. The theory of strong interactions was formulated as a non-abelian gauge theory with local internal $\mathrm{SU}_c(3)$ symmetry. As in the case of the Nambu model, the interaction between color charges is mediated by an octet of gauge fields coupled to the generators of $\mathrm{SU}_c(3)$ group. The dynamics of the theory is dictated by the requirement of the local gauge invariance with respect to the SU(3) transformations in the space of color charge. Particles of this gauge field are massless vector bosons, we call them *gluons* today. In contrary to the abelian QED, gluons also carry color charge. This is a direct consequence of non-abelian structure of SU(3) group and local gauge invariance of the theory. As a result, in addition to the quark-quark-gluon

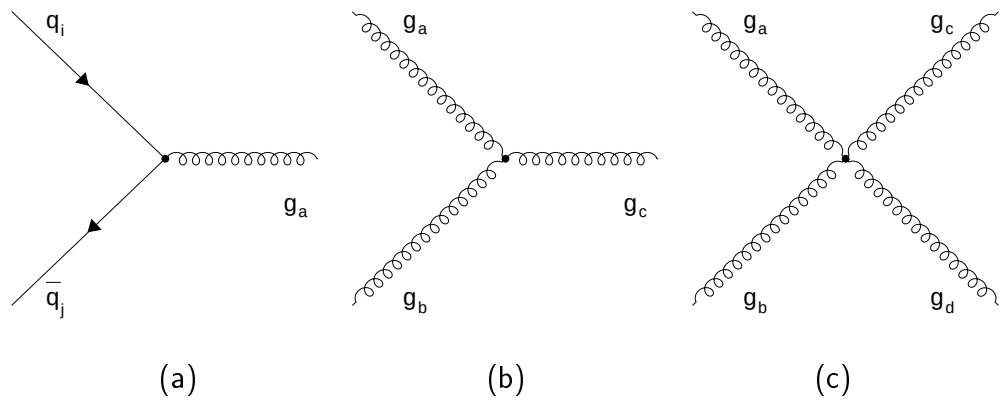

Figure 3: QCD interaction vertexes.

interaction (Fig. 3a), there are also three (Fig. 3b) and four (Fig. 3c) gluon self-interaction present in the theory. This gluon self-interaction is responsible for the different behaviour of the strong and electromagnetic coupling constants at small distances.

The theory was named Quantum Chromodynamics by Gell-Mann according to the name of strong charge, *color*. Quarks were identified with the charged partons in the parton model and gluons with the neutral partons. QCD, as a theory with asymptotic freedom, explained the observed weak Q^2 dependence of the structure functions in DIS. However, QCD also predicts the magnitude of violation of this scaling. An excellent agreement of measured Q^2 dependence of DIS structure functions with QCD perturbative calculations is a strong experimental evidence in favour of QCD. Nowadays, the picture of strong interactions as described by QCD is supported with a large amount of data from lepton-lepton, lepton-hadron and hadron-hadron colliders.

2.1 Ultra-violet divergences and running α_S

Two kinds of infinities appear in perturbative QCD (pQCD) calculations. One is associated with the divergence in the integration over large values of momenta in the loop diagrams. These ultra-violet (UV) divergences are dealt

with renormalization procedure. The divergences are absorbed by redefining the coupling constant, masses, and wave functions. This renormalizability is an important feature of QCD. Not all field theories do allow to perform renormalization consistently.

The renormalization procedure inevitably introduces a scale μ on which the redefined quantities depend. Although observable quantities do not depend in principle on this scale, truncation of the perturbative expansion violates this independence. Nevertheless, the requirement of observables to be independent on μ constrains the μ dependence of renormalised quantities. Renormalised strong coupling constant $\alpha_S(\mu)$ satisfies[4]

$$\frac{\mathrm{d}\alpha_S(\mu/\Lambda)}{\mathrm{d}\ln(\mu/\Lambda)} = -b\,\alpha_S^2(\mu/\Lambda)\,[1 + c\,\alpha_S(\mu/\Lambda) + \ldots]\,. \tag{3}$$

Since the scale μ has a dimension of energy, α_S, as a dimensionless quantity, must be a function of scale μ divided by some additional parameter Λ that has also a dimension of energy. In case of massless quarks the first two coefficients b and c in the expansion series are determined only by the number of quark flavors n_f and the number of colors N_c

$$b = \frac{11N_c - 2n_f}{6\pi} \quad \text{and} \quad c = \frac{1}{2\pi}\frac{51N_c - 19n_f}{11N_c - 2n_f}\,. \tag{4}$$

In case of ordinary QCD with $N_c = 3$, coefficient b is positive for $n_f < 17$. The leading order solution of Eq. 3 (i.e. when only the leading term in α_s on the right side of the equation is taken into account) for $b > 0$ is

$$\alpha_S(\mu/\Lambda) = \frac{1}{b\,\ln(\mu/\Lambda)}\,. \tag{5}$$

We see that α_S decreases with increasing μ and that it converges to zero in the limit of $\mu \to \infty$. As was discussed earlier, this type of behaviour of strong coupling constant, called *asymptotic freedom*, is crucial to understand

[4]The coupling constant α_S also depends on coefficients in front of higher order terms of perturbative expansion on the right side of Eq. 3. These coefficients are not uniquely defined and an arbitrary value can be assigned to them. This feature of higher order calculations is discussed in [11].

the weak Q^2 dependence of form factors in DIS data. On the contrary, α_S becomes large as μ approaches the scale Λ. This behaviour of α_S gives a hope that color confinement could be explained within the framework of QCD. Scale Λ determines the region in which the perturbative theory is not adequate. It should be of the order of a typical scale on which the non-perturbative phenomena appear, i.e. of the order of 1 fm which corresponds to $\Lambda \sim 0.2\,\mathrm{GeV}$.

The strong coupling constant α_S was measured by numerous experiments at different scales from $\sim 1.7\,\mathrm{GeV}$ up to $\sim 250\,\mathrm{GeV}$. The observed scale dependence [23] is in excellent agreement with the expectations of QCD as given by Eq. 3.

2.2 Treatment of infrared (IR) singularities

The second type of singularities in pQCD is connected with the long distance behaviour of QCD. The divergences appear in the integration over small values of loop momenta (therefore the name *infrared*) or whenever two partons in the final state are collinear or one of the final state partons is soft. This is a general property of gauge invariant theories with massless gauge fields. The IR divergences are treated in completely different way than the UV ones. Instead of redefining quantities, they are cancelled if all physically indistinguishable initial and final states are properly taken into account in the definition of physics observables.

The cancellation of IR divergences is demonstrated on the simple example of NLO cross section calculation of $\mathrm{e}^+\mathrm{e}^- \to$ *hadrons* process. The leading order term (Fig. 4) is finite and the corresponding cross section is[5]

$$\sigma_{LO} = \sum_i \frac{4\pi\alpha^2 e_i^2}{3s^2}\,, \tag{6}$$

where $\sqrt{s}$ is the center of mass (CMS) energy, α is the fine structure constant, and e_i is the electric charge of a particular quark of type i. The LO cross

[5]Contribution of the channel with virtual Z^0 is ignored. It is not relevant for the discussion of IR singularities.

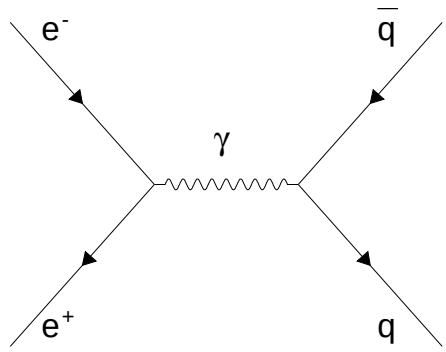

Figure 4: LO diagram for $e^+e^- \to$ *hadrons* process.

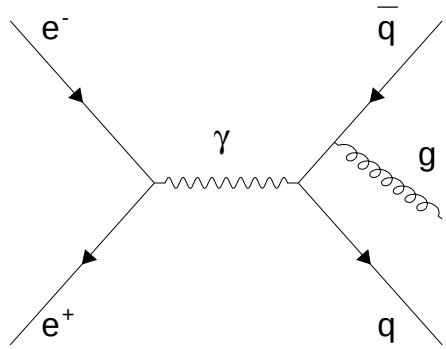

Figure 5: LO diagram for $e^+e^- \to q\bar{q}g$ process.

section for $e^+e^- \to q\bar{q}g$ process (Fig. 5) is given by

$$\frac{d\sigma_{q\bar{q}g}}{dx_1 x_2} = \sigma_{LO} \frac{2\alpha_S}{3\pi} \frac{x_1^2 + x_2^2}{(1-x_1)(1-x_2)} \tag{7}$$

where $x_1 = 2E_1/\sqrt{s}$ and $x_2 = 2E_2/\sqrt{s}$ are the quark and anti-quark fractional energies to the total CMS energy $\sqrt{s}$. This process, which contributes to the total e^+e^- cross section in order of $\mathcal{O}(\alpha_S)$, is divergent whenever a gluon is emitted collinearly with a quark on anti-quark or if a gluon is radiated with zero energy. Consequently, the total cross section is infinite. The LO, tree level, QCD prediction of production of three partons in the e^+e^- interaction is $+\infty$!

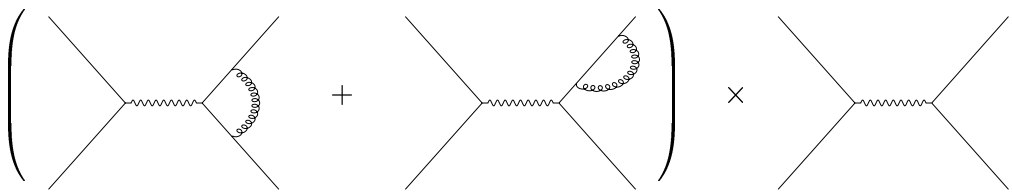

Figure 6: Interference terms that contributes to $e^+e^- \to q\bar{q}g$ cross section in order of $\mathcal{O}(\alpha_S)$.

Fixing the number of partons in the final state is unphysical in a sense that perturbative QCD gives infinite cross sections in that case. There is no way how to distinguish single quark from the state of collinear quark and gluon if they carry the same 4-momentum and the same quantum numbers. Therefore, also $\mathcal{O}(\alpha_S)$ diagrams with $q\bar{q}$ final state need to be taken into account. Such diagrams have a gluon in the internal loop. The corresponding matrix element is of the order $\mathcal{O}(\alpha_S)$, which would lead to the $\mathcal{O}(\alpha_S^2)$ contribution to the total e^+e^- cross section, however the interference term with LO $e^+e^- \to q\bar{q}$ diagram (Fig. 6) gives a contribution of the order of $\mathcal{O}(\alpha_S)$. The "cross section" of this process with virtual gluon is also singular. But the interference is destructive which makes it negative.

By regularising the divergences (for example by introducing non-zero gluon mass m_g), it can be shown [24] that the virtual singularities cancel with collinear and soft ones. NLO cross section of $e^+e^- \to hadrons$ process is thus finite even in the limit of $m_g \to 0$

$$\sigma_{NLO} = \sigma_{LO}\left(1 + \frac{\alpha_S}{\pi}\right) . \tag{8}$$

The cancellation of IR divergences, as was shown in the above example, is generalised in *Kinoshita-Lee-Nauenberg theorem* (KLN). According to this theorem, mass singularities disappear if all possible states degenerate with the particular initial and final states are taken into account [11]. Two states of particles are considered degenerate (or physically indistinguishable) if they carry the same quantum numbers and the same 4-momentum.

KLN theorem ensures that total cross sections in pQCD are finite. On the other hand we would like to calculate more detailed information of the final state. As we saw earlier, asking that a certain number of partons is present in the final state is not meaningful in pQCD. Particles are therefore combined into groups (called *jets*) in such a way that collinear partons are assigned to one jet. Various prescriptions how to reconstruct jets from partons exists. These, so called *jet algorithms*, are discussed in more details in section 4. The concept of jets is illustrated here on the cone algorithm which is used in this measurement of the inclusive dijet mass spectrum. Partons within a cone of radius R are assigned to one jet in this algorithm. In case of e^+e^- interactions, the cone is drawn in the space of azimuthal and polar angle ϕ and ϑ: $\Delta R = \sqrt{\Delta\phi^2 + \Delta\vartheta^2}$. It is clear that two collinear partons are combined into one jet and hence the same jets are found in two mutually indistinguishable states [6]. This allows to compute differential cross sections as a function of jet quantities. It makes also sense to ask for a certain fixed number of jets to be present in the final state; the cross sections for $e^+e^- \to 2jets$ and $e^+e^- \to 3jets$ processes are finite although not necessary positive. If the cone size is small enough, the negative contribution of virtual gluon cross section overcomes the positive contribution of the three parton cross section and the two jet cross section can become negative eventually.

Numerical QCD NLO programs, such as JETRAD [9] used for the NLO calculation of the inclusive dijet mass spectra, need to treat the cancellation of IR divergences properly. JETRAD uses the so called phase space slicing method. It introduces parton resolution parameter $s_{\min}$. Two partons are considered to be unresolved if their invariant mass is smaller than $\sqrt{s_{\min}}$. Giele and Glover, the authors of JETRAD, calculated in [25] the structure of soft, collinear, and virtual singularities as a function of this cut parameter $s_{\min}$. The singularities cancel each other and the cross sections for production

[6] This is true at least in NLO calculations with up to 3 partons in the final state. If more partons are present in the final state, this simple geometric definition must be accompanied by sets of rules that define what to do in the cases when the cones overlap. Infrared safety of cone algorithm than depends on details of this splitting/merging procedure.

of the resolved partons are finite. JETRAD is then a Monte Carlo generator of these resolved partons on which the jet algorithms can be run.

2.3 QCD improved parton model

Production of high p_T jets is described within the quark parton model as scattering of individual partons. Schematic formula for the cross section calculation reads[7]

$$\sigma_{A+B} = \sum_{a,b,c_1,c_2,\ldots} \int \mathrm{d}x_a \, d_{a|A}(x_a) \int \mathrm{d}x_b \, d_{b|B}(x_b) \sigma_{a+b->c_1+c_2+\ldots} \,, \tag{9}$$

where parton distribution function $d_{a|A}(x_a)$ describes the probability to find inside hadron A a parton of type a carrying a fractional momentum x_a and similarly for PDF $d_{b|B}(x_b)$. Free partons a and b are scattered at large momentum transfer (i.e. small time scale) and the outgoing partons does not feel any force. But when a parton covers a distance typical to the hadron size ($\sim 1\,\mathrm{fm}$), it starts to feel the color of the hadron remnant. Increasing strong force prevents the color to escape from the remnant. At some point the color connection between the remnant and the scattered parton is broken by the production of $\mathrm{q\bar{q}}$ pairs. These newly created partons are then reorganised into colorless hadrons. In the end, an energy flow steeply peaked in the directions of hard outgoing partons is observed in the final state. These collimated showers of particles are called jets. There are also some particles radiated between the nucleon remnants and jets. These are the remains of the color connection between the parton and the remnant. The above picture is a base for hadronization models. The most widely used hadronization models are the Lund string model implemented in PYTHIA [26, 27], cluster hadronization implemented in HERWIG [28], or a simple model of independent fragmentation in ISAJET [29].

[7] Final state configuration is not specified in the formula. In that case all, only those configuration of partons $c_1, c_2, \ldots$ that gives desired final state configuration should be considered only.

How is this picture affected by QCD? First of all, QCD allows us to compute higher order corrections to cross sections of hard parton scattering $\sigma_{a+b->c_1+c_2+...}$. As was discussed in section 2.1, renormalization procedure introduces scale dependence of observables in higher orders of perturbative calculations.

The second aspect concerns parton distribution functions. Partons in nucleons are not free, although they behave like almost free in interactions with high momentum transfer. The fact that the partons are not free means that they could be off shell, i.e. they could have non-zero virtualities $q^2 - m^2$, where q is parton 4-momentum and m is the mass of the parton. PDF are therefore also functions of parton virtualities. Perturbative QCD is not suitable for calculation of PDFs because this requires the knowledge of nucleon structure at large distances. However, as in the case of running α_S, it predicts the dependence on the virtuality. In leading order, the virtuality dependence of quark, anti-quark, and gluon distribution functions $q_i(x, M)$, $\bar{q}_i(x, M)$, and $G(x, M)$ is given by the so called *Altarelli-Parisi evolution equations* [11]:

$$\begin{aligned}
\frac{\mathrm{d}q_i(x,M)}{\mathrm{d}\ln M} &= \frac{\alpha_S(M)}{\pi}\left[\int_x^1 \frac{\mathrm{d}y}{y} P_{qq}^{(0)}\left(\frac{x}{y}\right) q_i(y,M) + \int_x^1 \frac{\mathrm{d}y}{y} P_{qG}^{(0)}\left(\frac{x}{y}\right) G(y,M)\right] \\
\frac{\mathrm{d}\bar{q}_i(x,M)}{\mathrm{d}\ln M} &= \frac{\alpha_S(M)}{\pi}\left[\int_x^1 \frac{\mathrm{d}y}{y} P_{qq}^{(0)}\left(\frac{x}{y}\right) \bar{q}_i(y,M) + \int_x^1 \frac{\mathrm{d}y}{y} P_{qG}^{(0)}\left(\frac{x}{y}\right) G(y,M)\right] \\
\frac{\mathrm{d}G(x,M)}{\mathrm{d}\ln M} &= \frac{\alpha_S(M)}{\pi}\left[\int_x^1 \frac{\mathrm{d}y}{y} P_{Gq}^{(0)}\left(\frac{x}{y}\right) \sum_{i=1}^{n_f} [q_i(y,M) + \bar{q}_i(y,M)] + \right. \\
&\qquad \left. + \int_x^1 \frac{\mathrm{d}y}{y} P_{GG}^{(0)}\left(\frac{x}{y}\right) G(y,M)\right] , \qquad (10)
\end{aligned}$$

where the scale M should be interpreted as a maximal virtuality of the parton that enters the hard scattering matrix element. Structure function $q_i(x, M)$ therefore corresponds to the probability to find a quark of flavour i with a fractional momentum x and with a virtuality up to M. $P_{qq}^{(0)}$, $P_{qG}^{(0)}$, $P_{Gq}^{(0)}$, and $P_{GG}^{(0)}$ are the leading order QCD branching functions. For instance, $P_{qG}^{(0)}(x)$ describes the probability to find a quark inside gluon that would carry a fractional momentum x of the the original gluon momentum. Leading order branching functions are uniquely determined. But the NLO ones $P^{(1)}$ are

in principal arbitrary. The situation is similar to the case of a perturbative expansion of α_S. The higher order terms (not explicitly shown in Eq. 3) are arbitrary numbers. Selection of particular values defines *renormalization scheme* (RS) while selection of $P^{(1)}$ defines *factorization scheme* (FS). QCD thus modifies general cross section formula (9) to

$$\sigma_{A+B} = \sum_{a,b,c_1,c_2,\ldots} \int \mathrm{d}x_a \, d_{a|A}(x_a, \mu_{F1}, FS_1) \int \mathrm{d}x_b \, d_{b|B}(x_b, \mu_{F2}, FS_2) \cdot$$
$$\cdot \; \sigma_{a+b->c_1+c_2+\ldots}(s, x_a, x_b, \mu_R, RS, \mu_{F1}, FS_1, \mu_{F2}, FS_2) \,, \qquad (11)$$

where we have introduced μ_F for factorization scale (i.e. maximum allowed virtuality M) in order to distinguish it from renormalization scale μ_R. In higher orders of pQCD, parton can be emitted in the initial state. However, parton collinear radiation (up to particular virtuality M) is already taken into account in the evolution equations and it is therefore already included in PDF. These collinear emissions should be excluded from hard matrix elements in order not to double count them which makes the cross section for hard parton scattering also dependent on factorization scales and factorization schemes.

We don't know how to determine PDFs from first principles which makes QCD less predictive. However an important feature of QCD is the universality of PDFs. The proton structure is the same if it collides with leptons or hadrons. Although different experiments measure nucleon structure functions at different scales of virtualities they should be connected via the evolution equations. The fact that observed scale dependence of structure functions agrees with the predictions based on QCD evolution equations is a strong experimental evidence for QCD.

Two main groups CTEQ [1] and MRST [30] perform so called global analysis of various data from different experiment in order to produce parton distribution functions. Parton structure functions are parameterised at some initial scale M_0. For a given set of parameters and a given value of parameter Λ, evolution equations (10) allows to compute PDF at any x and virtuality M and to make prediction on the value of a particular observable. These

parameters together with Λ are then fitted to give the best description of the selected set of data. The problem was how to assign an error on PDF and consequently the error on the prediction. Groups were usually producing several global fits and the difference between them was treated as an error. A consistent treatment of error on PDF global fits becomes available only recently, like for CTEQ6 [10]. It is an important step towards the precision comparison of QCD predictions with the data.

CTEQ6.0 contains 41 sets of PDFs: $S_0, S_1^+, S_1^-, \ldots, S_{20}^+, S_{20}^-$. S_0 is the best fit. The remaining 40 sets are used for the estimate of PDF error. They correspond to the plus and minus directions in the space of fitted parameters along each eigenvector of the Hessian matrix. The uncertainty ΔX on a particular observable X can be calculated according to the formula

$$(\Delta X)^2 = \sum_{i=1}^{20} \left[\frac{X(S_i^+) - X(S_i^-)}{2} \right]^2 . \tag{12}$$

Fig. 7 shows the uncertainty on up quark and gluon PDFs in CTEQ6.0M. Solid lines correspond to the ratio of $S_i^\pm$ PDFs to the best fit S_0. The shaded region represents the PDF uncertainty calculated according to Eq. 12. As was already pointed out in the introduction, current data constrain quark PDFs quite well even at large x while gluon PDF is constrained very weakly for $x \gtrsim 0.5$.

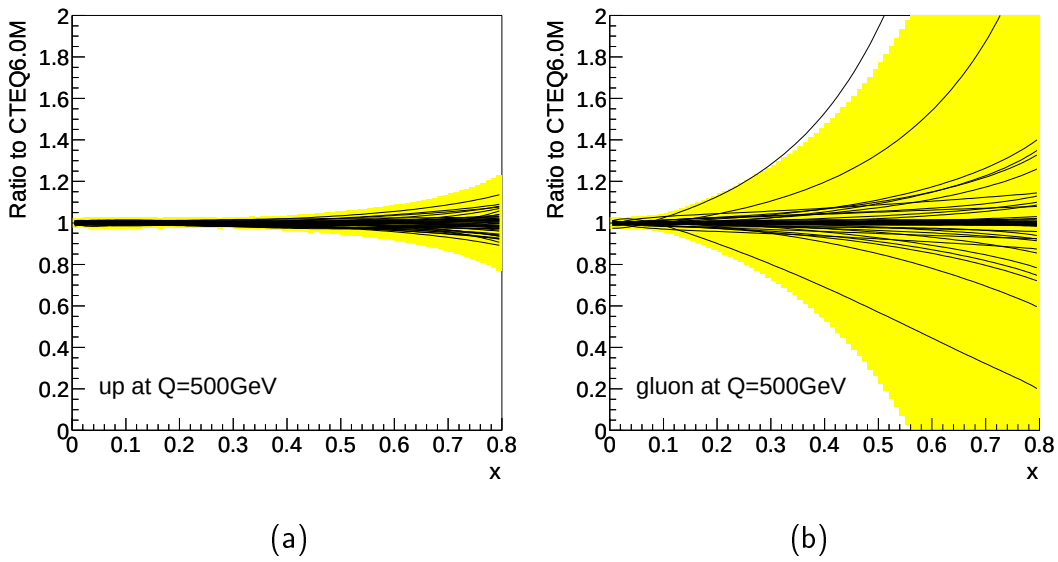

Figure 7: CTEQ6.0M uncertainties on up quark (a) and gluon (b) parton distribution functions.

3 The DØ detector

The DØ detector [31], displayed on Fig. 8, is a general purpose detector intended to study high energy proton anti-proton interactions produced by the Tevatron.

The tracking system is installed next to the beam. It consists of the Silicon Microstrip Tracker (SMT) and the Central Fiber Tracker (CFT) placed in the 2 T magnetic field. The curvature of the charged particle tracks allows us to determine particle transverse momenta. The tracks are also used to reconstruct primary and secondary vertexes in the interaction.

Calorimeter is located behind the magnet. There are three main calorimeter parts: the central cryostat (CC) and two end-cap cryostats (EC). The space between the cryostats is filled by the Inter-Cryostat Detector (ICD) and Massless Gap Detector. The electromagnetic part of the calorimeter captures photons and electrons and the hadrons are absorbed in the hadronic part. The calorimeter is an essential tool for jet detection and a more detailed description is given in the next subsection. The Central Preshower (CPS) and the Forward Preshower (FPS) detectors are placed between the magnet and the calorimeter. These thin scintillator-based detectors are designed to enhance the electron and photon identification.

High energy muons that penetrate through the calorimeter are detected by the muon system. Three different layers together with the toroid magnetic field between the first two layers allow us to reconstruct muon tracks and to measure muon momenta. The central muon tracking system consists of 94 proportional drift tube chambers. The forward muon tracking system consists of mini-drift tubes. The muon drift detectors are complemented by layers of pixel scintillator counters. The counters are used for muon triggering, elimination of cosmics, rejection of out-of-time scattered particles, and identifying low p_T muons.

The Forward Proton Detector is a new detector dedicated to diffractive physics in Run II. It consists of 9 momentum spectrometers composed of 18 roman pots that are installed between 23 and 59 meters from the DØ

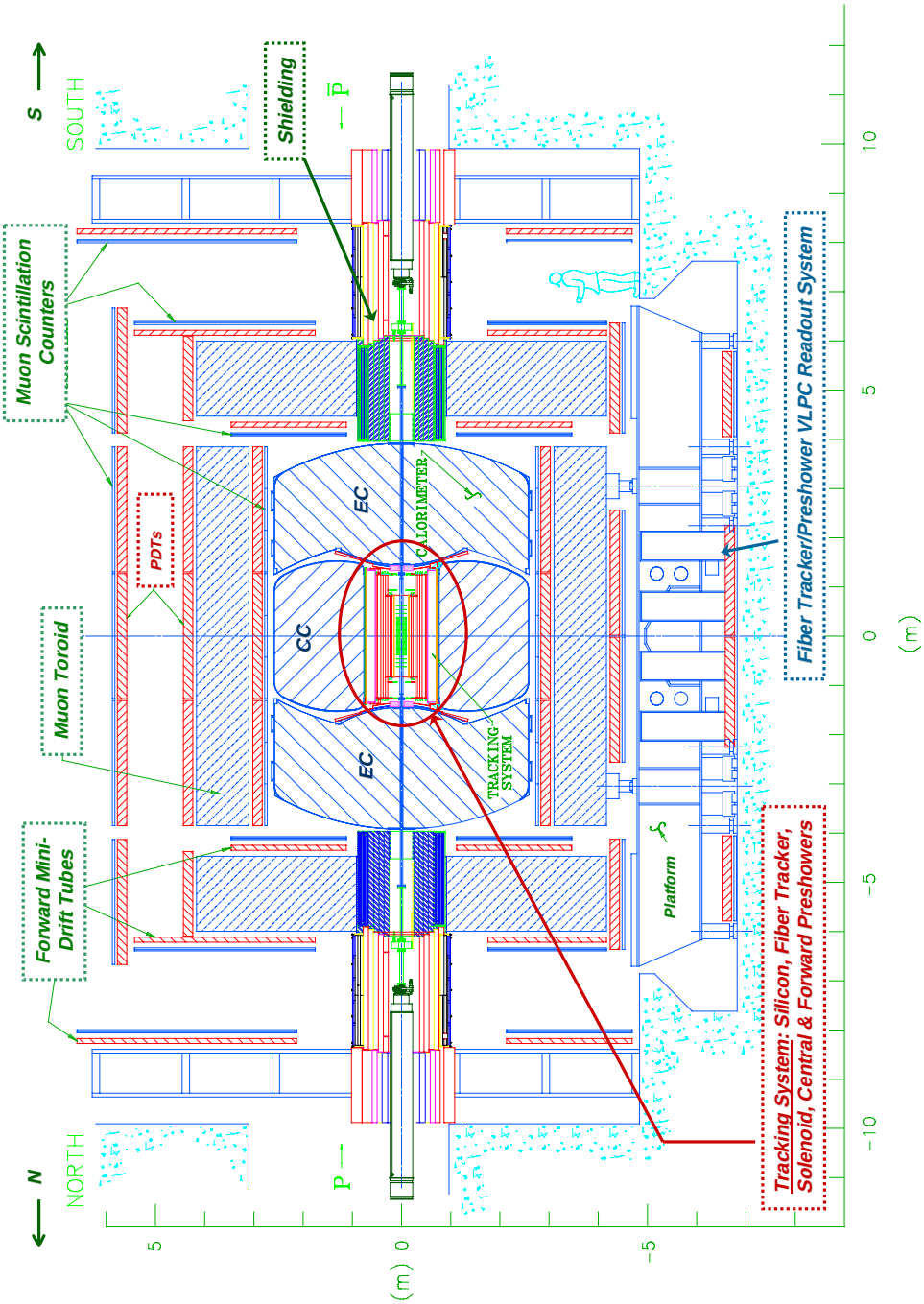

Figure 8: Global view of the DØ detector.

interaction point inside the Tevatron tunnel. The detector tracks the protons and anti-protons that were scattered at very small angles.

The DØ detector is supplemented by the Luminosity Monitor (LM) detector designed to measure the luminosity. Its function is described in section 6. Another essential part is the detector read-out and trigger system. More detailed information about the DØ Data Acquisition System (DAQ) relevant for the dijet mass cross section measurement is given in section 7 on jet triggers.

3.1 Calorimeter

Calorimeter provides energy measurement and identification for electrons, photons, taus, and jets. In addition, it is used to determine the transverse energy balance in an event. It also helps with muon identification. The minimum ionising signal from muons in the calorimeter can be used to improve the measurement of muon momenta.

The main calorimeter task, in general, is to absorb deposited energy and measure the overall energy flow in the interaction. Calorimeter is a large bulk of material (uranium, copper, and steel in the case of the DØ calorimeter) that absorbs the outgoing particles combined with an active medium (liquid argon in the case of the DØ calorimeter) that samples the electromagnetic and hadronic showers. Almost all of known elementary particle are captured in the calorimeter. Only weakly interacting neutrinos and high energy muons escape from the calorimeter. Muons are detected by the muon detectors located behind the calorimeter. A presence of neutrino in the event is indicated by the overall transverse energy imbalance.

The DØ calorimeter (Fig. 9) consists of three main modules: the central cryostat (CC) and two end-cap cryostats (EC). Each cryostat is divided longitudinally into three sections: the electromagnetic (EM), the fine hadronic (FH), and the coarse hadronic (CH). The module is comprised of layers of uranium (in the EM and FH part) and copper or stainless steel (CH) absorber plates. The space between the plates is filled by liquid argon that serves as

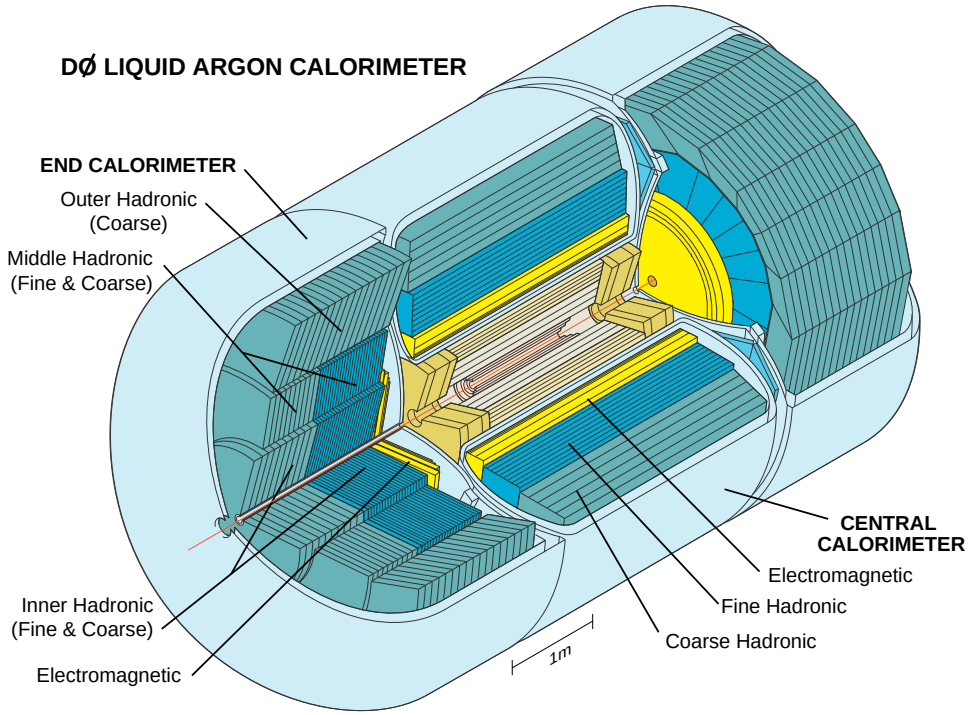

Figure 9: The DØ calorimeter, from [32].

active medium to sample ionization produced in the electromagnetic and hadronic showers. In order to partially recover for the response losses, the space between the cryostats is filled with the Inter-Cryostat Detector and the Massless Gap Detector.

Calorimeter *cell*, displayed in Fig. 10, is a basic unit the signal is collected from. It consists of an absorber plate followed by the gap filled by liquid argon. The read-out electronics is inserted in the liquid argon gap. The metal plate is grounded while the positive high voltage (typically $2.0 - 2.5\,\mathrm{kV}$) is brought to the resistive surface of the signal boards. The negative ions and electrons drift towards the electronics surface in this electric field; the electron drift time across the 2.3 mm gap between the absorber and the electronics surface is 450 ns. The whole calorimeter has about 50 000 read-out channels.

A typical cell size in terms of azimuthal angle ϕ and pseudorapidity η (related to polar angle ϑ by the equation $\eta = -\ln\tan(\vartheta/2)$) is $\Delta\phi \times \Delta\eta =$

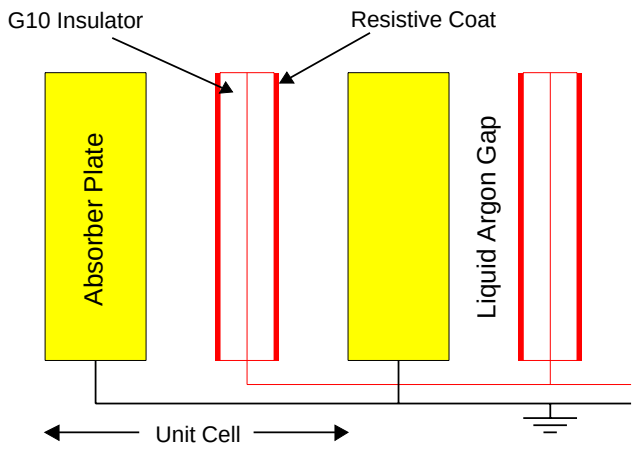

Figure 10: Schema of calorimeter cell, from [32].

0.1×0.1. The third layer of the electromagnetic part, where electrons and photons deposit about 65% of their energy, is two times smaller in order to improve the resolution in position of electrons and photons. Cells at large pseudorapidities ($|\eta| > 3.2$) are another exception. These cells are larger than the normal ones. Cells are arranged into *projective towers*, Fig. 11. The term projective means that the cell centers in the tower lie on the ray originating from the geometrical center of the detector. The towers are semi-projective rather than truly projective; tower boundaries are perpendicular to the beam in the central part and towers have a 'staircase' shape.

DØ calorimeter was designed as a compensated calorimeter. It means that calorimeter response to the electromagnetic objects should be the same as for hadronic ones. The response of the DØ calorimeter to electrons and pions is nearly the same for energies above 30 GeV; the measured e/π ratio is less than 1.05 for these energies. The hadronic and electromagnetic parts of the calorimeter shower significantly fluctuate jet by jet. For compensated calorimeters, the detector response does not depend on whether the jet shower is dominated by the electromagnetic or hadronic part. Consequently, the response of compensated calorimeters is Gaussian. It can be

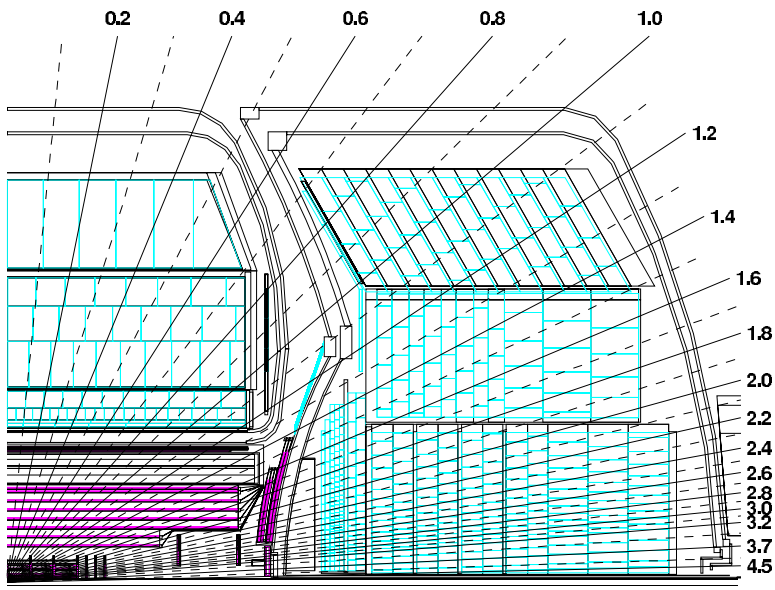

Figure 11: Layout of calorimeter cells and projective towers, from [32].

characterised by a mean value (jet energy scale, see section 5) and by the width (see section 10.1 on jet p_T resolution).

3.1.1 Central calorimeter (CC)

The central cryostat covers the region up to $|\eta| \lesssim 1$ but the boundary of the last projective tower for which all EM, FH, and CH layers are contained in the central calorimeter corresponds to $|\eta| = 0.7$. Towers at larger pseudorapidities extend to the end caps.

The electromagnetic part of the central calorimeter has four layers. Their thickness in units of radiation length X_0 is approximately 2.0, 2.0, 6.8, and 9.8. The first two layers sample the early stages of the electromagnetic shower development where photons and π^0s differ statistically. Electromagnetic objects deposit most of their energy (typically 65%) in the third layer. As was mentioned before, the transversal segmentation of this layer is made twice finer ($\Delta\phi \times \Delta\eta = 0.05 \times 0.05$) in order to improve the resolution in position of reconstructed EM objects. A full EM module comprises $20.5X_0$ and $0.76\lambda_I$,

where λ_I is the nuclear interaction length.

The hadronic part consists of three layers in the fine hadronic section and one layer in the coarse hadronic section. The corresponding depths are 1.3, 1.0, 0.9, and $3.2\lambda_I$. Total calorimeter thickness $7.2\lambda_I$ including the EM part is large enough to absorb almost all released energy. According to the Run I study [32], based on the NuTeV collaboration measurement of charged pions energy losses as a function of the nuclear interaction length and on Monte Carlo simulation of the calorimeter, less than 0.5% of energy escapes from central calorimeter for $E_T \sim 400\,\mathrm{GeV}$ jets.

3.1.2 End-cap calorimeter (EC)

Two mirror-like end-cap cryostats are attached to the north and south ends of the central calorimeter. They cover the region $0.7 < |\eta| < 4.5$. The electromagnetic part has 4 layers with thickness of 2.3, 2.6, 7.9, and $9.3X_0$. The hadronic part consists of three separate modules (see, Fig. 9). The inner hadronic module, located just behind the electromagnetic module, comprises of 4 fine hadronic layers ($1.1\lambda_A$ each) and one coarse hadronic layer ($4.1\lambda_A$). The middle hadronic (MH) module has ring shape and it surrounds the inner hadronic module. There are also 4 fine hadronic layers ($0.9\lambda_A$ each) and one coarse hadronic layer ($4.4\lambda_A$) in MH ring. The furthest from the beam is located the outer hadronic module. Its absorbator plates are made from steel. They are inclined at an angle of about 60° with respect to the beam axis.

3.1.3 Inter Cryostat Detector (ICD)

Significant amount of dead material is located in the gaps between central and end-cap cryostats. The gaps cover the region $0.8 \leq |\eta| \leq 1.4$. In order to correct for the energy losses deposited in this uninstrumented material, several scintillator-based counters were placed in to the gaps. These counters are intended to help to reconstruct the EM showers. Two scintillator arrays called the Inter Cryostat Detectors are mounted on the EC calorimeters.

The size and position of the scintillator tiles correspond to the position of calorimeter towers. ICD is supplemented by single-cell like structure, called the Massless Gap detector. The massless gap cells are installed both in CC and EC.

3.1.4 Calorimeter readout and treatment of hot cells

The only part of calorimeter that was upgraded in Run II is the readout electronics. The reason is the much shorter time between crossings of proton and anti-proton bunches which is 396 ns now but it could be as short as 132 ns in different running mode of the Tevatron. Detailed description of the calorimeter electronics upgrade is given in [33, 34].

Drift current between the absorber plate and the resistive surface of the cell electronics board induces an image charge on copper pads located on the other side of the resistive coat. Collected charge is integrated and transformed proportionally to voltage pulses. The pulses are then transfered to the baseline subtraction (BLS) board. The rise time of the pulse (~ 430 ns) corresponds to the electron drift time in the liquid argon gap. The lifetime of pulse decay is 15 μs which is much larger than the time between bunch crossings. The preamplifier output is therefore differentiated with a time constant of 250 ns. The shaped signal is then sampled in its peak value.

The BLS boards also subtract from signal so called *pedestal* value which is an average cell signal when no beams are present in the beam pipes. The pedestals are measured regularly roughly every second day in special calibration runs. In addition, BLS boards store the signal noise for each individual cell. It is obtained from the spread of signal values during the pedestal calibration. Real signal, during normal data taking, is then calculated as a measured signal minus the particular cell pedestal. In the end, only cells which show signal in absolute value bigger than a certain multiple of the cell noise σ are readout. Negative energy signals are also allowed. This mode of calorimeter readout is called *zero suppression mode*. The data used in this analysis were all taken with 1.5σ zero suppression limit but later on, dur-

ing the reconstruction process, all cells up to 2.5σ limit were removed. The analog signal from BLS is carried to the first two levels of trigger system. If event fires any of the triggers the analog signal is digitised an readout by the third level of the trigger system. Calorimeter signal is not exactly proportional to the deposited charge. These nonlinearities are measured using the calibration pulser system. The calorimeter cell energies are corrected for this effect during the reconstruction process.

Various hardware errors like failure in baseline subtraction or high voltage discharge can occur. They result usually in unrealistically high energies (positive or negative). Such calorimeter cells are called *hot cells*. Obviously we want to exclude them from further data processing. The hot cells are identified in several levels. Cells that show too high pedestals or noise during the pedestal calibration run are marked as hot and they are removed from the calorimeter readout. Another identification of hot cells is performed on event by event basis during the data reconstruction by NADA (New Anomalous Deposit Algorithm) [35, 36]. NADA is looking for isolated high energy cells. If all the nearest neighbours of such cell show energy smaller than some threshold NADA marks the cell as a hot. Cell neighbours are defined as those belonging to a cube surrounding a particular cell. Cube size in (η, ϕ) plane is 0.3×0.3 and 3 calorimeter layers in depth, i.e. only cells that have some contact with the hot cell candidate are considered. The NADA criteria used in the case of the analysed data are:

1. Calorimeter cell with transverse energy smaller than $-1\,\mathrm{GeV}$ is always marked as a hot cell.

2. If the cell transverse energy is between $1\,\mathrm{GeV}$ and $5\,\mathrm{GeV}$, the cell is treated as a hot one as long as there is no neighbour cell with $E_T > 100\,\mathrm{MeV}$. The condition is not applied for cells from the first and the last EM layers, the ICD and the Massless Gap layers, and the first fine hadronic and the last coarse hadronic layers.

3. If the cell transverse energy E_T^{cell} is between $5\,\mathrm{GeV}$ and $500\,\mathrm{GeV}$, the

cell is marked as a hot as long as there is no neighbour cell with $E_T > 0.02E_T^{\text{cell}}$. The criterion is applied for all calorimeter layers.

4. Calorimeter cell with transverse energy bigger than 500 GeV is always marked as a hot cell.

Hot cells identified by NADA are then removed from the list of cells. They are not considered at all in the jet reconstruction or in the calculation of missing transverse energy.

4 Hadron final states - jets

Jets, as introduced in section 2.2, are useful tool that allows us to characterise parton final states in pQCD calculations. The concept can be extended to describe hadron final states and to describe final states as they appear in the detector. Various levels at which the jets can be defined are illustrated in Fig. 12. We speak about *parton jets* (jets formed from partons in the fixed order of pQCD calculation, or jets formed from partons after parton showering), *particle jets* (jets formed from particles in the final state of interaction), or about *detector jets* (usually jets formed from calorimeter towers). Perturbative QCD allows us to calculated jet cross sections at parton level. However, parton hadronization is a non-perturbative phenomenon. Jet properties at particle level need to be model (some widely used hadronization models are listed in section 2.3). The most important feature which makes the jet concept useful is that the jet properties (like energy and direction) are strongly correlated between various levels. This allows us to compare various measured jet distributions with theoretical predictions of perturbative QCD.

Jets are not fundamental objects; there are different ways how to define them. The detailed description how to construct jets is called *jet algorithm*. The main feature of a jet algorithm is how well it preserves the correlations of jet properties between various levels. It should also be suitable from experimental and theoretical points of view. Namely, the algorithm should not depend on the detector parameters (like calorimeter cell size) and it should be insensitive to soft and collinear emission of partons. There are plenty of jet algorithms used in high energy physics. They can be divided roughly into two groups.

Cone algorithms are based on geometrical definition. Jet is formed by a group of partons (particles, or calorimeter towers) that belong to a cone of given radius R. In e^+e^- interactions, the cone is drawn in the space of azimuthal angle ϕ and polar angle ϑ

$$\Delta R = \sqrt{\Delta^2\phi + \Delta^2\vartheta}\,. \tag{13}$$

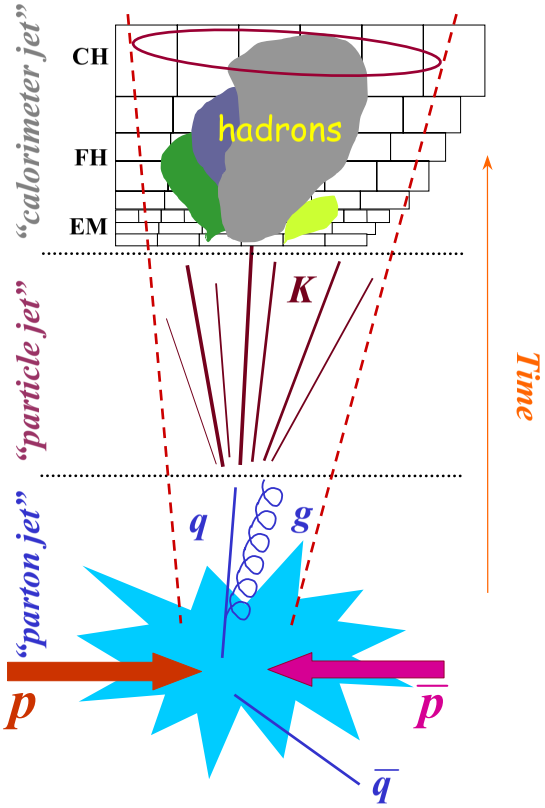

Figure 12: An illustration of the different levels the jets can be defined at.

However, the center of mass system (CMS) of the incident partons is moving along the beam axis in hadron-hadron collisions. Therefore, the polar angle is replaced by pseudorapidity $\eta \equiv -\ln\tan(\vartheta/2)$

$$\Delta R = \sqrt{\Delta^2\phi + \Delta^2\eta}\,. \tag{14}$$

which makes the distance ΔR invariant under Lorentz boosts along the beam. A prescription according to which the jet properties are calculated from the assigned particles is called *recombination scheme*. Most of schemes used by experiments are based on *Snowmass scheme* [37]:

$$E_T^{\rm jet} = \sum_i E_{Ti}\,, \quad \eta^{\rm jet} = \frac{\sum_i \eta_i E_{Ti}}{\sum_i E_{Ti}}\,, \quad \phi^{\rm jet} = \frac{\sum_i \phi_i E_{Ti}}{\sum_i E_{Ti}}\,. \tag{15}$$

Jets in this scheme are by definition massless. This was also the case of the Run I jets. The Run II cone algorithm is using *E-scheme* where the jet 4-momentum is given by sum of 4-momenta of the associated particles.

Cone algorithms have been the most used algorithms in hadron-hadron experiments. The advantage of cone algorithms is their simple geometrical interpretation. However, the problem starts when the cone jets overlap each other and the jet splitting and merging procedure has to be designed very carefully to avoid the problems with soft and infrared singularities. In addition, jet splitting and merging at hadron level has to be modelled in NLO QCD calculations and an ad-hoc parameter R_{sep} has to be introduced for cone algorithms on parton level [38].

Cone size R is an arbitrary parameter of the jet algorithm. Typical values used in the data analyses lie in the interval of $0.5 - 0.7$; this analysis uses $R = 0.7$ in particular. It roughly correspond to the observed size of particle sprays induced by the hard scattered partons. Another motivation for this choice of cone sizes is theoretical. NLO predictions for cone sizes $R \sim 0.7$ exhibit the smallest dependence on the choice of renormalization and factorization scales as is illustrated in Fig. 13. A scale dependence of NLO QCD prediction (JETRAD) of the central inclusive dijet mass cross sections ($|\eta_{jet}| < 0.5$) for various cone sizes are displayed in this plot for

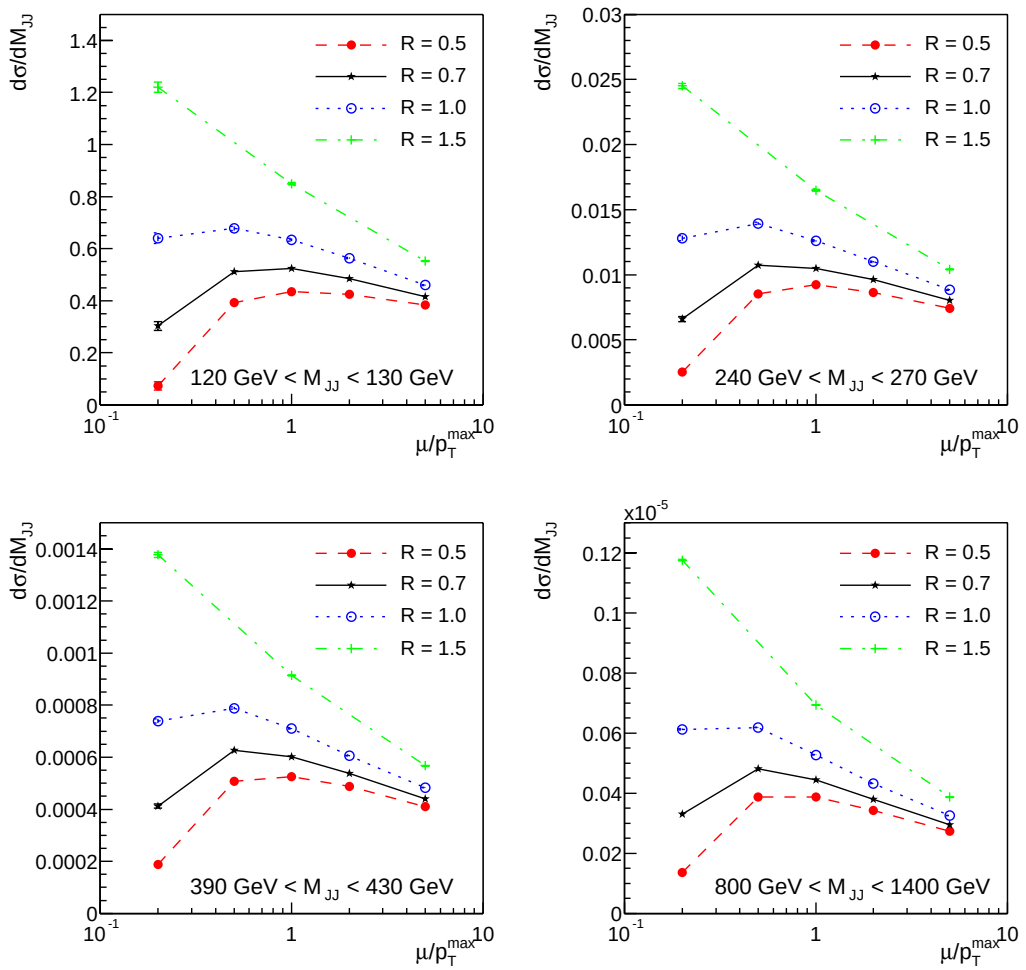

Figure 13: Scale dependence of NLO QCD prediction (JETRAD) of central inclusive dijet mass cross section ($|\eta_{jet}| < 0.5$) for various cone sizes in different mass bins. The factorization and renormalization scales are set equal ($\mu_F = \mu_R = \mu$); p_T^{max} is the transverse momentum of the leading jet. NLO calculation is done using CTEQ6.0M parton distribution function; R_{sep} parameter was set to 1.3 (see subsection 4.2).

different mass bins. A scale sensitivity of the calculated cross section is the smallest for $R \sim 0.5 - 0.7$ cones in the entire range of considered masses.

The other class of jet algorithms is the so called *k_T-algorithms*. The algorithms are inspired by the perturbative development of parton shower. Partons in the shower are mostly radiated along the direction of the original parton or they are soft. k_T-algorithm introduces the distance between two particles in such a way that soft or collinear particles are close to each other. The algorithm itself is an iterative procedure where the pair of the closest partons is recombined into one particle in single step. The iteration stops when the distance of the closest pair is bigger than some cut D [8]. The remaining recombined particles are then called jets. Such jets do not have a fixed geometric shape and their size is controlled by the parameter D.

The k_T-algorithms do not suffer from the theoretical problems as the cone algorithms. They are by construction infrared and collinear safe in all orders of pQCD. Every particle is uniquely assigned to jet which eliminates the problems with splitting and merging jets. Although k_T-algorithms are quite common in lepton-lepton and lepton-hadron collider experiments they have been used in hadron-hadron experiments only recently [39, 40]. k_T-algorithms are not discussed further in this thesis because the analysis works with cone algorithm only. Reader can find more information on k_T-algorithms in [41, 42, 43].

4.1 DØ Run II cone algorithm

A detailed description of DØ Run II cone algorithm used in the analysis is given in this section. The algorithm is similar to the one DØ was using in Run I but there are few important changes that improve behaviour of the algorithm on parton level. E-scheme recombination is used instead of the old scheme in which the jets were massless. The Run II cone algorithm also

[8] There are also other types of k_T-algorithms that do not require any additional parameters. k_T-algorithms can be also run in the mode with fixed number of jets in the final state. In that case the recombination continues until the desired number of jets is reached.

introduces an additional starting seeds compared to the Run I algorithm. These changes are based on the recommendations of the Run II jet physics group [44] and the Jet Definition Group Les Houches [45, 46].

Jets are formed from calorimeter projective towers only and no track information is used currently. A projective tower consists of calorimeter cells with a signal 2.5σ above the cell noise (see section 3.1.4). The Lorentz 4-momentum P_{tower} assigned to the calorimeter tower is computed as a sum of 4-momenta of associated cells

$$P_{tower} \equiv (E_{tower}, \vec{p}_{tower}) = \sum_{cell} P_{cell} \,, \tag{16}$$

where the cell 4-momentum P_{cell} is determined from the measured cell energy E_{cell} and the direction $\vec{n}_{cell}$ that points from the primary vertex of the interaction to the cell

$$P_{cell} \equiv E_{cell}\,(1, \vec{n}_{cell}) \;, \quad |\vec{n}_{cell}| = 1 \,. \tag{17}$$

The z-axis corresponds to the beam direction in the above definition. The jet 4-momentum P_{jet} is then just a sum of the 4-momenta of the associated towers

$$P_{jet} \equiv (E_{jet}, \vec{p}_{jet}) = \sum_{tower} P_{tower} \,, \tag{18}$$

where only towers with positive energy are considered. As was already pointed out, this recombination scheme is different from the one used in the Run I cone algorithm which was based on the Snowmass algorithm (Eq. (15)). Namely, the jets in the old recombination scheme were considered to be massless and the scheme was giving a recipe how to obtained the jet transverse energy and direction. On the contrary, the E-scheme, as defined by Eq. 18, fully specifies the jet 4-momentum and jets are no longer massless. Because jets are massive, the true jet rapidity y

$$y = \frac{1}{2} \ln \frac{E + p_z}{E - p_z} \tag{19}$$

is not the same as pseudorapidity η. The main reasons why this recombination scheme was chosen for Run II cone algorithm are its simplicity, implicit

4-vector form, and the fact that it satisfies *the boundary stability* condition[9]. In addition to the jet physics rapidity y and pseudorapidity η, the detector pseudorapidity η_{det} is used to characterise the jet position in the calorimeter. It is computed from the calorimeter cell coordinates as seen from the geometrical center of the detector.

The Run II cone algorithm is an iterative procedure which proceeds in the following steps:

1. The calorimeter towers with the transverse energy bigger than $E_T^{\rm seed} = 0.5\,{\rm GeV}$ are the staring seeds of the algorithm.

2. A small cone of radius $R = 0.3$ is drawn around the seed in space $\phi \times y$. All positive towers within the cone form a seed protojet.

3. The seed protojet 4-momentum is calculated according to Eq. 18. Again, new cone is drawn around this direction and the towers within the new cone are used to calculate the new direction of the seed protojet. This procedure continues until the protojet direction becomes stable.

4. Stable seed protojets with identical direction are treated as one seed protojet.

5. The seed protojets serve as a starting points for finding stable jet directions. The same iterative procedure as in step 3 is applied for the cone of a given radius R. Stable cones are called *protojets*. Again, stable protojets with identical direction are treated as one protojet.

6. Midpoints between protojet pairs (triplets, and so on) are used as the additional starting seeds. The midpoint position is defined in terms of jet 4-momenta P_1, P_2, ..., as

$$P_{mid} = P_1 + P_2\,, \quad P_{mid} = P_1 + P_2 + P_3\,, \quad \cdots\,. \tag{20}$$

[9]Boundary stability means that jet kinematic boundaries are independent on the details of the final state configuration. For example, the maximum jet scalar E_T should be smaller than $\sqrt{s}/2$ which is true for Run I algorithm only in the limit of collinear partons (massless jets). Boundary stability is essential in order to perform soft gluon resummations [45].

Only sufficiently close protojets within the distance of $2R$ are considered for midpoints since only those can overlap.

7. Stable positions for the midpoint seeds are found in the same way as in the fifth step. Again, stable protojets with identical direction are treated as one protojet.

8. Found protojets are ordered in transverse momentum. The protojet with the highest p_T that overlaps with another protojet is identified.

9. The two protojets are merged if they share more then 50% of transverse momentum of the softer one otherwise they are split. New merged protojet contains all towers from both protojets and it does not have the cone shape anymore. In the case of splitting, every single shared tower is assigned to the closer protojet. The 4-momenta of split and merged jets are recomputed according to Eq. 18. New protojet list is ordered again and the procedure continues until no overlapping jets remain.

10. Protojets with transverse momentum smaller than 8 GeV are removed from the list of protojets.

11. The protojets in the final list are then called jets.

The introduction of starting seeds significantly speeds up the algorithm and the concept is essential to be able to reconstruct the jets in the event in an acceptable time. However, it was pointed out that seeds, together with the split/merge procedure, introduce a sensitivity to the infrared and collinear parton emission for the Run I cone algorithm at next-to-next-to-leading order (NNLO) level [44]. For example, the two well separated partons in Fig. 14a form two jets. A soft gluon radiated in addition between those two partons with transverse energy just above the seed threshold E_T^{seed} forms additional jet that contains other two partons (Fig. 14b). Thus there would be only one jet in the final state after splitting and merging procedure. The

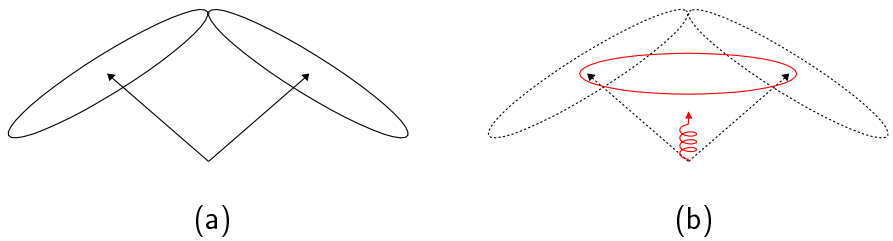

Figure 14: Demonstration of infrared sensitivity of cone algorithm with starting seeds. While there are two jets in the final state in the case of well separated partons (a) only one jet is found if an additional soft gluon is emitted between those two partons with transverse energy just above the seed threshold E_T^{seed} (b).

number of jets in the final state is sensitive to the soft gluon emission above the seed threshold E_T^{seed}. Calculated NNLO jet cross sections depends on $\log(E_T^{\text{seed}})$ [47]. Consequently, the limit $E_T^{\text{seed}} \to 0$ cannot be performed; the algorithm is not IR safe in NNLO.

The best solution of the problem would be not to use the seeds at all, i.e. to use every single calorimeter tower as a starting seed. However, this would slow the code too much. The number of jets in the final state found by the cone algorithm is mostly sensitive to the soft radiation between jets. Therefore the Run II cone algorithm introduces additional starting seeds in the midpoints between stable protojet. Because of this feature, the Run II algorithm is called *midpoint* algorithm or *Improved Legacy Cone Algorithm* (ILCA). Studies in [44] showed that this algorithm has much smaller sensitivity to the IR radiation. It produces very similar results as seedless algorithm without significant slowdown of the reconstruction code. Improved IR safety of the ILCA is important for future comparison of NNLO calculations with the data.

4.2 Cone jets at NLO QCD – R_{sep} parameter

NLO QCD final state of hadron-hadron interaction contains up to three partons. Jets are formed either from individual partons or from two close partons (for partons up to the distance $\Delta R_{1,2} < 2R$). Jet never contains three partons[10] because the event must be balanced in transverse momentum and one of them is well separated in azimuthal angle ϕ from the remaining two. The splitting and merging procedure used at the detector level cannot be applied in the NLO calculations simply because the shared energy between the two parton protojets is either 100% ($\Delta R_{1,2} < R$) or zero ($\Delta R_{1,2} > R$).

The splitting and merging procedure has to be modelled in NLO calculations. It is done by introducing a phenomenological parameter R_{sep} that controls the maximum distance of the partons that can be merged into one jet [38]. Two partons can form a jet only if their distance is smaller than $\Delta R_{1,2} < R_{sep}R$. If the distance is larger the two partons are treated as two separate jets. The case $R_{sep} = 1$ corresponds to no merging while the case $R_{sep} = 2$ corresponds to no splitting. Realistic value of the parameter R_{sep} lies between those two extremes.

NLO theory itself cannot determine the value of R_{sep}. It has to be obtained from data or Monte Carlo studies. Two methods were used in Run I [48]. The R_{sep} parameter was obtained in the first method by overlaying two experimental jets and determining at which distance the jets were merged. The second method was based on the parametrisation of measured jet shapes as a function of jet transverse energy leading to an analytic determination of R_{sep}. It was found that the value lies in the interval 1.2–1.4 and that $R = 1.3$ gives the best description of the DØ cone jet split/merge procedure. No such study was done for DØ Run II cone algorithm yet. Since the split/merge procedure is the same as in Run I we can expect the actual value of parameter R_{sep} for Run II cone is close to the Run I value.

[10] The statement is correct only for the cone sizes $R < 2\pi/3$. This is essentially true for all experiments where the cone size less than one is usually used.

5 Jet energy scale

Before any comparison between data and theory, the jet energies, as measured by the DØ detector, must be corrected to the particle level, i.e. to the original energy of the jets that are entering the detector. This *jet energy scale* (JES) correction is essential for any data analysis that works with jets. The DØ experiment formed a group that is responsible for the determination of JES. The resulted scale produced by JES group [49] (version `v04-01-00`) was used as an input to the dijet analysis. This chapter outlines how the energy scale is obtained. Also the most important aspects of the final energy scale correction relevant for the dijet mass analysis are discussed here.

The jet energy E_{det}, as reconstructed by the cone algorithm, is corrected to the particle level E_{ptcl} according to the formula

$$E_{ptcl}(E_{det}, \eta, R, \mathcal{L}) = \frac{E_{det} - \mathcal{O}(R, \eta, \mathcal{L})}{R_{jet}(E_{det}, \eta, R)\, S(R, \eta, E_{det})}\,, \tag{21}$$

where η, R, and $\mathcal{L}$ are the jet pseudorapidity, the cone radius, and the instantaneous luminosity, respectively. The correction consists of three parts that are discussed in the following.

Offset $\mathcal{O}(R, \eta, \mathcal{L})$ corrects for the energy deposited in the cone that is not directly associated with the $p\bar{p}$ interaction itself (uranium noise, pile-up from the previous beam crossings or additional minimum bias interaction in the current beam crossing). In general, it depends on the place where the jet hits the calorimeter (η), the cone size R, and the instantaneous luminosity $\mathcal{L}$. So far, the luminosity dependence is omitted. Although the maximum instantaneous luminosity achieved during the data taking ($3.5 \times 10^{31}\,\mathrm{cm}^{-2}\,\mathrm{s}^{-1}$) is about twice time larger than in Run I, the pile-up and additional minimum bias interactions are about 3 times smaller in Run II. This is because the Tevatron collides 36 proton and anti-proton bunches now while it was only 6 in Run I. Currently, the offset correction is determined from the measured average transverse energy density deposited in the calorimeter during a special minimum bias run. The energy density is flat in the central region of

the calorimeter ($|\eta| < 0.8$); it varies between 0.8 and 0.9 GeV/$\Delta\eta \times \Delta\phi$ per event. For the jets of cone $R = 0.7$, the transverse energy not associated with the hard p$\bar{\text{p}}$ interaction is about 1.3 GeV. The offset correction is important for the low-p_T jets while it is small for jets above 100 GeV. The error on the offset correction is considered to be the same as the correction itself in the current version of JES.

Response $R_{jet}(E_{det}, \eta, R)$ corrects the jet energy for the response of the calorimeter to particles that constitute the jet. Although the DØ calorimeter is nearly compensated, the response to jets is smaller than one due to non-linear calorimeter response to particles with low energy and dead material in front of the calorimeter.

The correction is determined from the transverse energy imbalance in photon+jet events using the so called missing E_T projection fraction method. It requires the calorimeter to be calibrated for electro-magnetic objects. This EM scale is obtained independently of the jet energy scale. DØ uses the known masses of resonances like Z, J/Ψ, or π^0 for this purpose. The cross section for the production of photon+jet events is small compared to the regular jet+jet QCD production. The photon+jet sample contains therefore only relatively low-p_T objects. The jet response is measured for the central and the end caps cryostats separately in the first step. The CC, where p_T is roughly the same as energy, covers the low energy region while the end caps cover the high energy end. The response in CC and EC parts is not necessarily the same. A cryostat factor F_{cry}, defined as the ratio of EC response to CC response, is calculated in the second step. This factor is assumed to be independent on energy due to similar construction of the cryostats. However, there is only one overlapping point at energy of 70 GeV between CC and EC responses in the current data sample. The cryostat factor is therefore determined with large error; the actual value is $F_{cry} = 0.926 \pm 0.022$. Since it is measured only in one data point, 7.4% error is assigned to F_{cry} for now. The response after the cryostat factor correction is

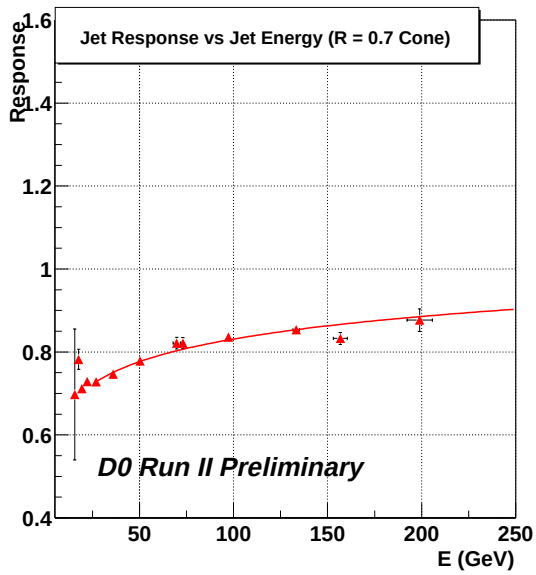

Figure 15: Jet response after the cryostat factor correction for a cone size of 0.7, from [49].

displayed on Fig. 15 for a cone size of $R = 0.7$. The highest energy at which the response is measured is 200 GeV. The jet response at higher energies is given just by the extrapolation of the fit. It means that only the region with a dijet mass $M_{JJ} \lesssim 140$ GeV is corrected using the JES measured in the central part of calorimeter in the case of the inclusive dijet mass spectrum. The largest part of the dijet mass spectrum is covered by the JES measured in the end caps ($\sim 140 - 400$ GeV) or even only by extrapolated JES ($M_{JJ} \gtrsim 400$ GeV).

The jet response in the intercryostat region is determined separately using the same method as in the case of CC and EC. This correction (calculated as a difference from the CC response) is applied as an additional multiplicative factor for jets with $0.6 < |\eta| < 1.55$. The ICD correction is maximal at $|\eta| \sim 1.25$. It is about 0.75 for this particular pseudorapidity which is much larger than in Run I where the ICD correction factor was about 1.1. It is caused

by a known bug in the calibration of the ICD in the p13 release of the DØ reconstruction software. The energies reported by the ICD detector are four times smaller as they should be. The ICD scale was fixed in the p14 release. However, the analysis and the jet energy scale uses data reconstructed with the p13 release. Because of the bug, the measurement in this analysis is restricted only to the central calorimeter region.

No study of correlations between the errors coming from the response fit and cryostat and ICD factors determination was performed so far. The errors are added in quadrature assuming no correlations.

Showering $S(R, \eta, E_{det})$ corrects for the energy that dissipates from the cone during the shower development in the detector. The correction is determined from the jet profiles in the photon+jet sample. It is larger for smaller cones. It also increases with jet pseudorapidity because the forward cones have smaller absolute sizes (expressed in units of length, meters). In the case of central jets with a cone size of $R = 0.7$, the correction is small; the value is 0.993.

The JES corrections together with their errors are shown in Fig. 16 for central jets ($\eta = 0$) as a function of jet energy E_{det}. It decreases from 28% at $E_{det} = 40\,\mathrm{GeV}$ to 5% at $500\,\mathrm{GeV}$. The error on JES is dominated by systematics. The overall error (statistical and systematic errors added in quadrature) is about 10% for energies up to $200\,\mathrm{GeV}$. Then it increases monotonely to 15% at $500\,\mathrm{GeV}$. The pseudorapidity dependence of JES is displayed in Fig. 17 for $R = 0.7$ jets with $E_{det} = 100\,\mathrm{GeV}$. The corrections and errors are roughly constant for pseudorapidities up to ~ 0.6. However, in the intercryostat region, the correction becomes larger than 60% and also the error is much higher. As was already pointed out, this big magnitude of JES and its error in the ICD region was the main reason why the analysis is restricted to central dijets only with rapidity $|y_{jet}| < 0.5$.

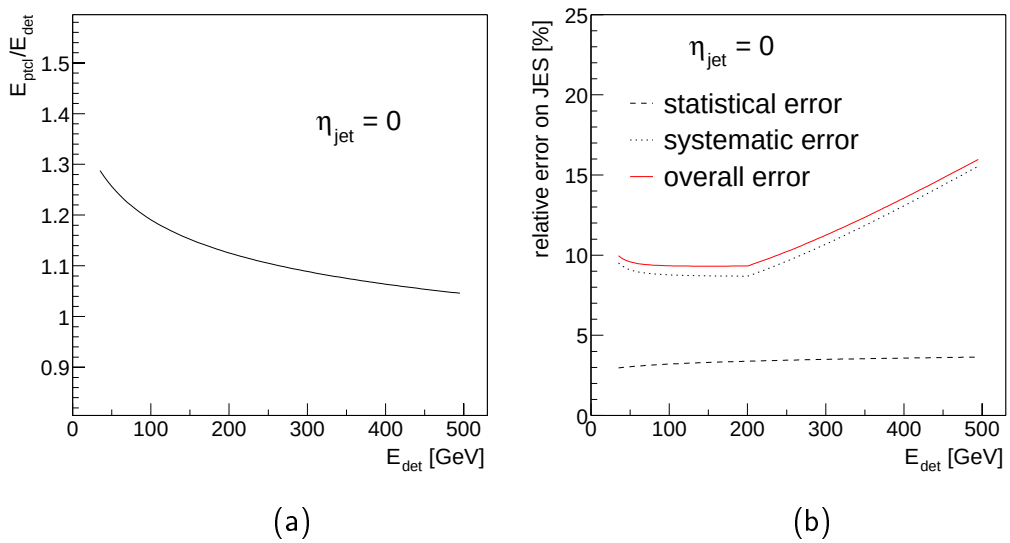

Figure 16: JES correction (a) with the error (b) for central jets with cone size of $R = 0.7$.

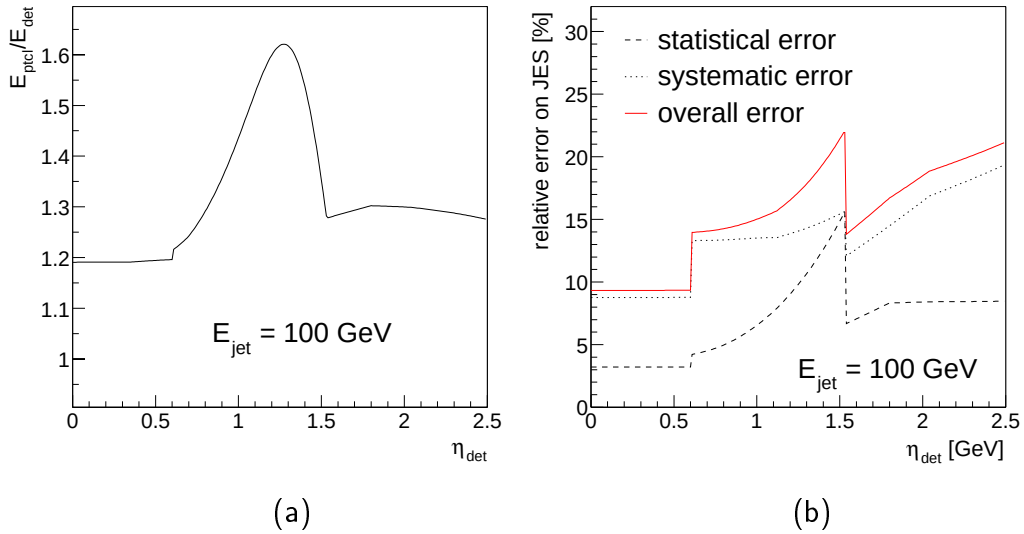

Figure 17: JES correction (a) and error (b) as a function of pseudorapidity for $R = 0.7$ jets with $E_{det} = 100\,\mathrm{GeV}$.

6 Luminosity

Any cross section analysis requires the precise knowledge of the total integrated luminosity that corresponds to the analysed data sample. This section summarises how the luminosity is measured in the DØ experiment, more detailed information can be found in [50, 51, 52, 53].

6.1 Structure of the Tevatron beam

A short description of the Tevatron time structure relevant for the luminosity measurement is given in this part. The Tevatron operates at a *radio frequency* (RF) of 53.104 MHz. One turn corresponds to 1113 RF *buckets* and the revolution frequency is thus 47.713 kHz. A group of seven buckets is called a *tick*; there are 159 ticks in one turn. Protons and anti-protons are grouped into bunches. A bunch can be located in the first bucket of the tick only. The Tevatron is running currently in the so called 36×36 mode with 36 ticks populated by proton bunches and 36 ticks populated by anti-proton bunches. There are at least two empty ticks (396 ns) between the two subsequent bunches. The basic beam properties, like number of protons and anti-protons in a bunch, vary between different bunches. Consequently, the instantaneous luminosity corresponding to the crossing of two bunches depends on the tick number. The difference could be more than factor of 2. Therefore the luminosity is measured tick by tick in the DØ experiment.

6.2 Luminosity Monitor

In principle, luminosity can be determined directly from the beam properties. However, the beam parameters are not known with such precision that would allow us to compute luminosity with a reasonable error. Normalisation in the DØ experiment is therefore obtained from the rate of a monitor process and the known cross section for this process.

The detector used for luminosity measurement in the DØ experiment is called *Luminosity Monitor* (LM). It is a counter detector of $p\bar{p}$ collisions.

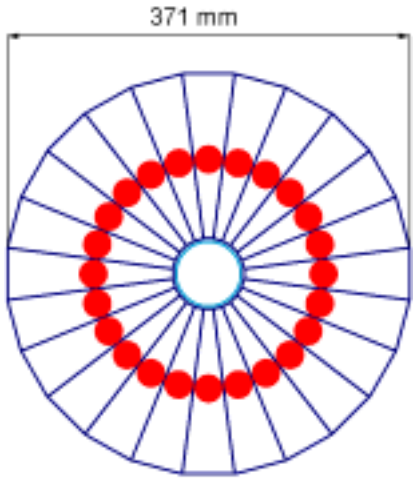

Figure 18: One disk of the Luminosity Monitor, from [53]. The solid circles represent the location of the photomultiplier tubes.

The LM consists of two disks built from 24 wedges of plastic scintillators read-out via photomultipliers (Fig. 18). The disks are placed near the beam pipe on both sides of the detector just in front of the end-cap calorimeter cryostats (Fig. 19). The detector covers $2.7 < |\eta| < 4.4$.

The LM uses the time difference between hits in the north and south disks to distinguish real collisions from the halo interactions. Muon produced by proton halo interaction gives the signal in north disk and about 9 ns later it hits the south disk. Similarly, the anti-proton halo will first interact with the south disk and then with the north one. The outgoing particles from regular proton anti-proton interaction arrive in both disks roughly at the same time (Fig. 20). The time difference between the hits is used to determine the z position of the interaction vertex.

6.3 Method of luminosity measurement

The time coincidence of the hits in the two LM disks gives the evidence of a $p\bar{p}$ interaction. The rate of the coincident signals together with the known

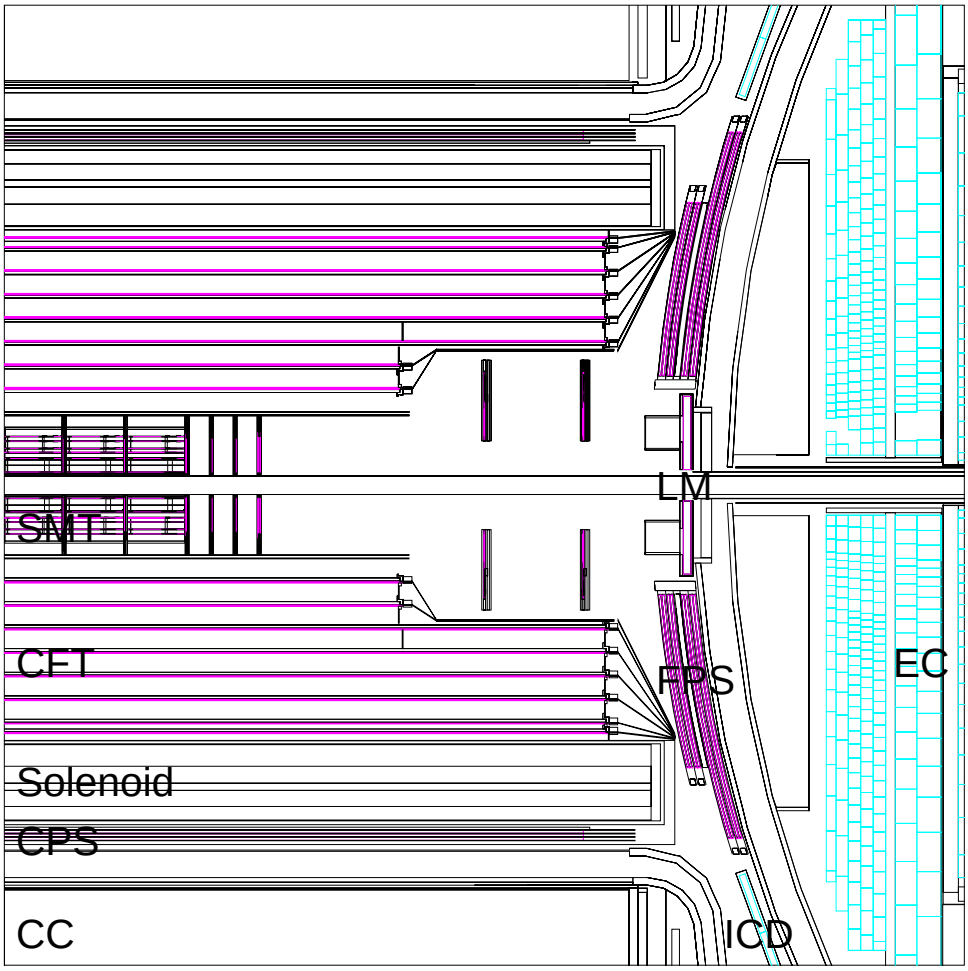

Figure 19: Cut-view of the central part of the DØ detector, from [53]. The Luminosity Monitor (LM) is placed close to the beam pipe just in front of the end-cap cryostats (EC).

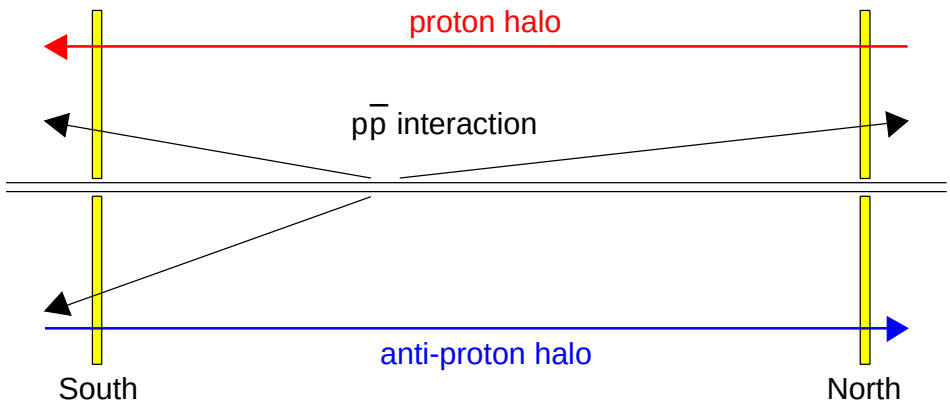

Figure 20: Hits in the Luminosity Monitor disks produced by regular p$\bar{\text{p}}$ interaction, proton halo, and anti-proton halo.

p$\bar{\text{p}}$ cross section σ and LM acceptance and efficiency determine the delivered luminosity. For this purpose, *luminosity constant* σ_{eff} is introduced. It is an effective total p$\bar{\text{p}}$ cross section that takes into account the LM acceptance and efficiency.

The probability that n p$\bar{\text{p}}$ interactions occur in one beam crossing is given by the Poisson distribution

$$P(n) = \frac{\mu^n}{n!} e^{-\mu} \,, \tag{22}$$

where μ is the average number of p$\bar{\text{p}}$ interactions per crossing. The probability that at least one interaction occurs (i.e. LM sees a coincidence) is then

$$P(n > 0) = 1 - P(0) = 1 - e^{-\mu} \,. \tag{23}$$

This probability is measured by the Luminosity Monitor. It is a ratio of the number of LM coincidences N_{LM} to the total number of beam crossings N_{cross}

$$P(n > 0) = \frac{N_{LM}}{N_{cross}} \,. \tag{24}$$

The value of μ can be determined from this measurement using Eq. 23

$$\mu = -\ln\left(1 - \frac{N_{LM}}{N_{cross}}\right) . \tag{25}$$

The average number of interactions μ that give signal in the LM is related to the instantaneous luminosity $\mathcal{L}$ and the effective $p\bar{p}$ cross section σ_{eff} by the equation

$$\mu f_{cross} = \mathcal{L}\sigma_{eff} , \tag{26}$$

where f_{cross} is the beam crossing frequency. A combination with Eq. 25 yields

$$\mathcal{L} = -\frac{f_{cross}}{\sigma_{eff}} \ln\left(1 - \frac{N_{LM}}{N_{cross}}\right) . \tag{27}$$

In practice, the proton and anti-proton bunches in the beam do not have the same properties and μ changes between the collisions of different bunches. The luminosity needs to be measured independently for each tick, i.e. for each of the 159 possible beam crossings. The total delivered luminosity is then a sum of the individual tick luminosities

$$\mathcal{L}_{\text{delivered}} = -\frac{f_{cross}/159}{\sigma_{eff}} \sum_{i=1}^{159} \ln\left(1 - \frac{N_{LM_i}}{N_{cross}/159}\right) , \tag{28}$$

where N_{LM_i} is the number of LM positive signals for a given tick of number i. The beam crossing frequency is $f_{cross} = 7.586\,\text{MHz}$, i.e. RF divided by seven (the number of buckets in one tick).

The integration time over which the LM signals are counted must be large enough to have enough statistics in Eq. 28. On the other hand, the interval must be short enough to be able to consider the luminosity constant. The time period over which the luminosity is measured in DØ is called *luminosity block* and it lasts for 60 s under normal circumstances. Each luminosity block is indexed by an integer number called *luminosity block number* (LBN) which is increasing by one every new luminosity block.

Each data file is opened and closed on the luminosity block boundaries[11] and the corresponding range of LBNs is stored in the meta-data description of

[11] It is not true for the first data file in the run. A run starts on a luminosity block boundary but the file is opened when the first event passes the trigger.

the file on SAM. SAM (Sequential data Access via Meta-data) is the system used in the DØ Collaboration for data handling [54]. The information about LBN and tick number is also recorded for each event. The luminosity for a given data sample can be derived from these pieces of information [55, 56].

The delivered luminosity measured from Eq. 28 has to be corrected for the dead time of the DØ detector and other losses in the data acquisition system (DAQ). For this purpose, the triggers are grouped into the so called *exposure groups*. Triggers within one exposure group have the same dead time. If any trigger in the exposure group is busy, none of them is allowed to fire. For each tick number of i, the number of ticks N_{EGi} for which the exposure group was alive is counted. Correction to Eq. 28 is then straightforward:

$$\mathcal{L}_{\text{triggered}} = -P_{\text{trigger}} \frac{f_{cross}/159}{\sigma_{eff}} \sum_{i=1}^{159} \frac{N_{EGi}}{N_{cross}/159} \ln\left(1 - \frac{N_{LM_i}}{N_{cross}/159}\right), \quad (29)$$

where P_{trigger} is prescale factor applied on particular trigger. Prescale controls how often a given trigger is allowed to fire. For example, prescale of 10 means that the trigger is allowed to fire only every tenth tick[12]. Losses in the DAQ are accounted for by monitoring minimum bias and zero bias triggers. Zero bias trigger is fired by the accelerator clock, i.e. it fires every tick. In addition, minimum bias trigger requires also the positive signal from the LM. These two triggers are not biased by any other condition at higher levels of the trigger system which makes them suitable for monitoring the DAQ losses. The correction to the triggered luminosity is given as a ratio of the recorder number of minimum bias and zero bias events ($N^{\text{rec}}_{\text{min}}$ and $N^{\text{rec}}_{\text{zero}}$) to the number of events accepted by the first level of trigger system ($N^{\text{L1}}_{\text{min}}$ and $N^{\text{L1}}_{\text{zero}}$):

$$\mathcal{L}_{\text{recorded}} = \frac{N^{\text{rec}}_{\text{min}} + N^{\text{rec}}_{\text{zero}}}{N^{\text{L1}}_{\text{min}} + N^{\text{L1}}_{\text{zero}}} \mathcal{L}_{\text{triggered}} \,. \quad (30)$$

[12]It was found that this approach was not selecting events without bias. Even though certain values of prescale were forbidden (like multiples of 3 and 53) the selected events were not populating all tick numbers evenly. In February 2003, the DØ experiment changed the prescaler. It selects the events randomly now with the average probability given by the particular prescale factor.

6.4 Normalisation uncertainty

The inelastic $p\bar{p}$ cross section can be decomposed into single diffractive σ_{sd}, double diffractive σ_{dd}, and non-diffractive σ_{nd} components. For each type of interaction, the LM has different acceptance A. The luminosity constant σ_{eff} expressed in terms of these cross sections reads

$$\sigma_{eff} = \varepsilon_{\mathrm{LM}} \left[A_{\mathrm{sd}}\sigma_{\mathrm{sd}} + A_{\mathrm{dd}}\sigma_{\mathrm{dd}} + A_{\mathrm{nd}}\sigma_{\mathrm{nd}} \right], \tag{31}$$

where $\varepsilon_{\mathrm{LM}}$ is the efficiency of the LM. Elastic part is omitted because the LM acceptance for elastic interaction is practically zero.

The Run I value of luminosity constant $\sigma_{eff} = 43$ mb is based on the world average of total $p\bar{p}$ cross sections measured at $\sqrt{s} = 1.8$ TeV by the E710 Collaboration [57], the CDF Collaboration [58], and the E811 Collaboration [59]. The CDF Collaboration used its own $p\bar{p}$ cross section measurement in Run I which resulted in a 6.1% difference in normalisation between both experiments. CDF and DØ are discussing how to unify the set of $p\bar{p}$ cross section measurements used for the determination of luminosity. The DØ luminosity constant will be reviewed based on the results of the discussion.

So far, the DØ Collaboration is using in Run II the same value of the luminosity constant as in Run I. However, the geometry of LM and the electronics gains are not the same as in Run I. Relevant measurements of the Run II LM acceptance and efficiency have not been performed yet. Also, the world average $p\bar{p}$ cross section has not been scaled to the Run II CMS energy of $\sqrt{s} = 1.96$ TeV. It is expected that the difference in the luminosity constant between Run I and Run II is not larger than 10% [60]. Therefore, large 10% uncertainty is assigned to the normalisation in the present.

7 Jet triggers

The DØ data acquisition system consists of three levels in order to reduce the rate of interactions from $\sim 2.5\,\mathrm{MHz}$ to the rate ($\sim 50\,\mathrm{Hz}$) acceptable to store data on tapes. Level one (L1) is hardware trigger that makes decisions every possible beam crossing, i.e. with frequency of $7.586\,\mathrm{MHz}$. It was designed to reduce the event rate up to $10\,\mathrm{kHz}$. Level two (L2) reduces the L1 rate by factor of 10. It is combination of hardware and firmware trigger. L2 preprocessors build L2 objects from particular detectors. The information about the L2 objects is collected and passed to the global processor which makes the final decision. Various L1 trigger objects from different detectors can be combined together at this level. If the event passes L2 the detector signal is digitised and the full detector is readout by Level three (L3). L3 trigger is software trigger that is running on dedicated PC cluster. The output rate of L3 is $50\,\mathrm{Hz}$. Events selected by L3 are stored on tapes.

The definition of L1 jet triggers is based on conditions applied on L1 calorimeter towers. For the purpose of triggering, four calorimeter towers are grouped into one. The angular size of L1 calorimeter towers is thus $\Delta\phi \times \Delta\eta = 0.2 \times 0.2$. L1 calorimeter readout differs from the regular one; it is using analog signal from BLS boards directly. The coverage of L1 calorimeter trigger was up to $|\eta| < 2.4$ during the time period that corresponds to the analysed sample. It was extended up to $|\eta| < 3.2$ at the end of January 2003. Jet triggers require that an event has a certain number of towers with a transverse energy above a given threshold. The rate of L1 trigger is controlled by applying a *prescale*. Prescale N means that L1 is allowed to fire only every N-th tick (i.e. every possible bunch crossing, see section 6 on luminosity for more details).

If the L1 trigger fires, the information about L1 calorimeter towers is passed to L2. L2 forms square jets around the seeds that are identified using L1 towers with E_T above some threshold. Two possible jet sizes are available at L2; a jet consists of either 3×3 or 5×5 towers. An event passes L2 jet filter if a jet is found with a transverse energy above a given threshold.

Trigger	L1	L2 (GeV)	L3 (GeV)	Prescale
`CJT5`	1 tower > 5 GeV	none	none	~ 17400
`JT_25TT_NG`	2 towers > 5 GeV	none	1 jet with $E_T > 25$	~ 160
`JT_45TT`	2 towers > 5 GeV	none	1 jet with $E_T > 45$	~ 4.7
`JT_65TT`	3 towers > 5 GeV	1 jet with $E_T > 20$	1 jet with $E_T > 65$	~ 1.3
`JT_95TT`	4 towers > 5 GeV	1 jet with $E_T > 30$	1 jet with $E_T > 95$	No prescale
`JT_125TT`	4 towers > 7 GeV	none	1 jet with $E_T > 125$	No prescale

Table 1: L1, L2, and L3 configurations of jet triggers. The L2 conditions on triggers `JT_65TT` and `JT_95TT` were not applied all the time. They were introduced later on during the data taking. Also the L2 jet size was changed. L2 3×3 jets were used in the beginning. It was switched to 5×5 later on.

A fast simple cone algorithm is run on the precise calorimeter readout at L3. It sums up the transverse energies of towers within the cone of radius $R = 0.7$. Again, L1 towers above some threshold are used as seeds for the simple cone algorithm. No splitting and merging procedure is applied on the simple cones.

L1, L2, and L3 conditions are listed in Tab. 1 for the jet triggers used in the analysis. Trigger `CJT5` is filtering only at L1. It was used as a monitoring trigger for `JT_25TT_NG`. Trigger `JT_125TT` is not used in the analysis. It was kept in the trigger list in case that the collider would delivered higher instantaneous luminosity. However, we were able to run the trigger `JT_95TT` unprescaled all the time. Data from trigger `JT_125TT` are therefore just a subset of trigger `JT_95TT`.

Triggers were not exactly the same during the time period that corre-

Trigger list version	Date	$\mathcal{L}_{\mathrm{JT_95TT}}$ [pb^{-1}]	Changes in jet triggers
CMT-8.20	22/08/2002	4.2	
CMT-8.30	19/09/2002	3.0	no changes
CMT-8.40	04/10/2002	2.8	no changes
CMT-8.41	11/10/2002	7.4	`JT_25TT_NG` and `JT_45TT` are not using the same L1 trigger. They can be run with different prescales from now.
CMT-9.20	30/08/2002	5.3	Calorimeter zero suppression cut increased from 1.5σ to 2.5σ at L3.
CMT-9.30	13/11/2002	7.8	L2 terms added to `JT_65TT` and `JT_95TT`. The L2 jet size was 3×3.
CMT-9.31	04/12/2002	7.7	L2 jet size increased from 3×3 to 5×5.
CMT-9.50	19/12/2002	8.9	no changes
CMT-10.00	07/01/2003	1.0	no changes

Table 2: Trigger list versions which correspond to the data sample together with the list of changes that affected the jet triggers.

sponds to the analysed data sample. The list of trigger versions together with changes that affected jet triggers is given in Tab. 2. L1 conditions remained the same all the time. However, the L2 terms were added to triggers `JT_65TT` and `JT_95TT` in the trigger list version 9.30. L2 3×3 jets were used in the beginning. Starting from the version 9.31 the L2 jet size was increased to 5×5 in order to improve L2 trigger turn-ons. Also L3 triggers underwent changes. The L3 jet filters remained the same all the time but the calorimeter readout mode has changed. The zero suppression cut on calorimeter cells was switched from 1.5σ to 2.5σ in the L3 software starting with the trigger list version 9.20. All these modifications affect the trigger turn-ons and ef-

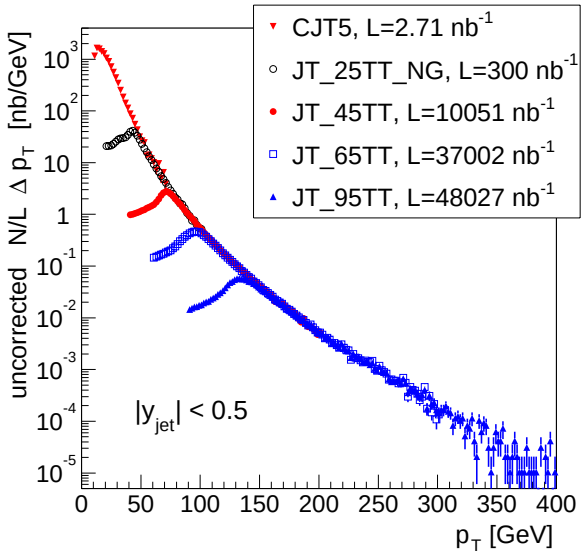

Figure 21: Uncorrected inclusive jet p_T spectra in the central region of the calorimeter for jet triggers. Trigger luminosities take into account possible L1 prescales.

ficiencies. However, the data from a given trigger were used only above the trigger *turn-on point* (the point where the trigger becomes almost 100% efficient). In this sense, there was no need to determine the trigger efficiencies for all different trigger definitions separately. Therefore, the above changes have no direct influence on the cross section measurement. They only affect the position of the turn-on points.

7.1 Trigger turn-on points

Trigger turn-on points are obtained by comparing the central inclusive p_T spectrum in a given trigger to the p_T spectrum in the trigger with a lower p_T cut at L3. Fig. 21 shows uncorrected inclusive p_T spectra for jet triggers in the central region of calorimeter ($|y_{jet}| < 0.5$). Spectra are normalised using trigger luminosities that take into account possible prescales applied at L1. The distributions in Fig. 21 have therefore the units of cross section but

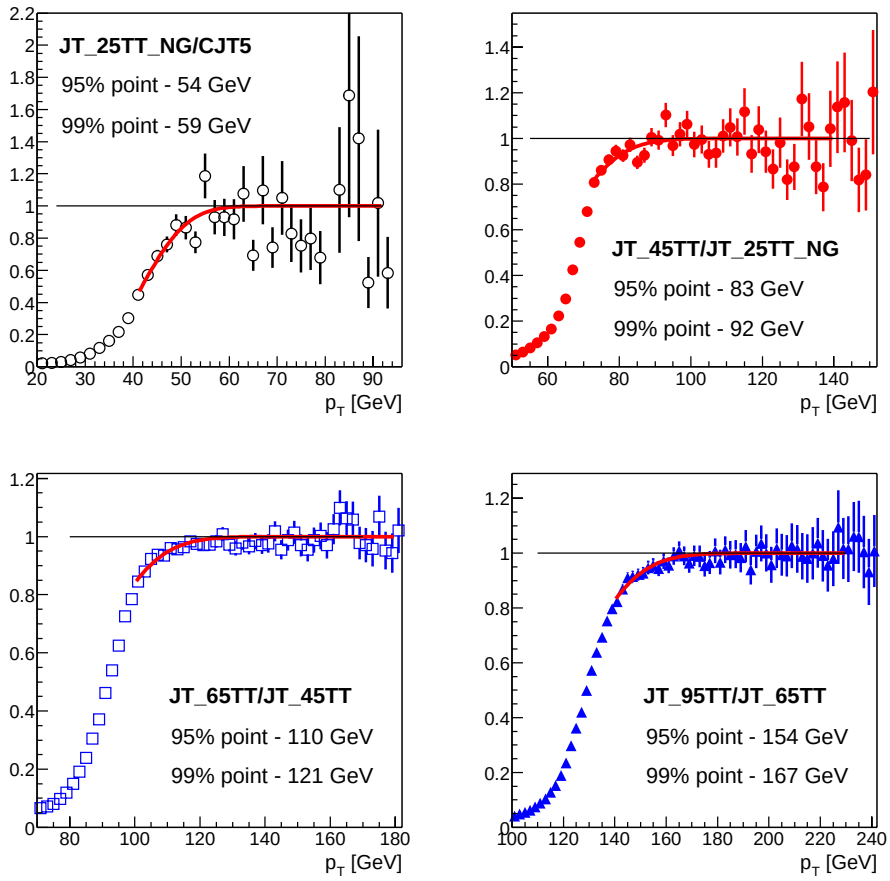

Figure 22: Ratio of inclusive p_T spectra in the two subsequent jet triggers. Solid lines represent the fit from Eq. 32.

they do not represent the final inclusive p_T cross sections because the only correction that is applied is jet energy scale. Since the remaining corrections (except trigger efficiencies) are smooth functions of p_T, the p_T spectrum in a given trigger is expected to start to match the lower p_T trigger spectra once a trigger becomes effective.

The logarithmic scale on the y-axis in Fig. 21 allows only a rough estimate of trigger turn-on points. In order to obtain more precise numbers, the ratios of p_T spectra for the two subsequent triggers are plotted in Fig. 22. The ratio

Trigger	95% turn-on point	99% turn-on point
JT_25TT_NG	54 GeV	59 GeV
JT_45TT	83 GeV	92 GeV
JT_65TT	110 GeV	121 GeV
JT_95TT	154 GeV	167 GeV

Table 3: The 95% and 99% turn on points for jet triggers in the central region of calorimeter ($|y_{jet}| < 0.5$).

is fitted using

$$\varepsilon(p_T) = \frac{1}{2}\left[1 + \mathrm{Erf}\left(a_0 p_T - a_1\right)\right], \tag{32}$$

where

$$\mathrm{Erf}(x) = \frac{2}{\sqrt{\pi}} \int_0^x \mathrm{d}\xi \exp(-\xi^2) \tag{33}$$

is the error function. The 95% and 99% points in Fig. 22 correspond to transverse momenta at which the fit reaches 0.95 and 0.99 efficiency respectively. They are listed in Tab. 3. Trigger CJT5 is not present in the table because there is no other jet trigger with lower p_T cut. It serves as a monitor trigger for the efficiency of trigger JT_25TT_NG only and the events from this trigger are not used in further analysis.

8 Data sample

The data used in this analysis were taken between September 3, 2002 and January 12, 2003. Only runs with fully functional and operational calorimeter and tracking system were used, the details of the run selection can be found in [61]. The data were processed with releases p13.05.00 and p13.06.01 of the DØ reconstruction software. Various physics objects (jets, muons, electrons, ...) are built at this stage. Both k_T and cone algorithms with different sizes are run by the reconstruction software at this stage. This study focuses on jets reconstructed with the Improved Legacy Cone Algorithm with a cone size of $R = 0.7$. The event size in the output of the reconstruction software is $200 - 300\,\mathrm{kB}$. The inclusive jet sample consists of more than 5 million events which would mean to work with 1.5 TB of the data. The analysis is therefore performed on the so called thumbnail (or mini-DST) files. Only reduced and packed information about the reconstructed objects is kept in the thumbnail files. The event size is about 10 kB.

A set of four inclusive jet triggers (`JT_25TT_NG`, `JT_45TT`, `JT_65TT`, and `JT_95TT`) with different transverse momentum thresholds at L3 (25, 45, 65, and 95 GeV, respectively) is used in the analysis in order to obtain the inclusive dijet mass spectrum in a wide range of masses (see section 7 for more details). Another trigger `CJT5` serves as a monitoring trigger for `JT_25TT_NG`. The data from this trigger are not used in the further analysis.

A production rate of events with jets rapidly falls down with the increasing cut on jet p_T. Therefore, only the trigger with the largest p_T threshold (`JT_95TT`) was run with no prescale. This allows us to store on tapes all interesting events with high p_T jets. To keep a reasonable event rate, the triggers with lower thresholds had to be prescaled. Corresponding luminosities collected in the jet triggers are listed in Tab. 4. As was already described in section 7, the definition of jet triggers were changing during the period of data taking. These changes were minor and they were properly taken into account by using data from particular trigger only above its turn-on point.

Trigger	$\mathcal{L}$ [pb^{-}1]
JT_25TT_NG	0.300
JT_45TT	10.1
JT_65TT	37.0
JT_95TT	48.0

Table 4: Luminosity in jet triggers.

9 Event selection and associated efficiencies

This section starts with an overall definition of the central dijet sample used in the dijet mass spectrum analysis. The discussion of the individual event selection cuts together with associated efficiencies follows. In the last part, some basic jet distributions are examined in order to check the quality of the event selection.

9.1 Central dijet sample

The central dijet sample is a set of events that satisfy the following event selection criteria:

- **topological cuts**
  - events contain at least two jets reconstructed with the Run II Improved Legacy Cone Algorithm with a cone size of $R = 0.7$
  - the two leading jets (after jet energy scale correction) must be in the central part of calorimeter: $|y_{jet1}| < 0.5$ and $|y_{jet2}| < 0.5$
- **event quality cuts**
  - both leading jets have to pass the standard jet selection criteria
  - cut on missing E_T

    $$\not{E}_T < 0.7 p_T^{jet1} \quad \text{for} \quad p_T^{jet1} < 250\,\text{GeV}$$
    $$\not{E}_T < 175\,\text{GeV} \quad \text{for} \quad p_T^{jet1} > 250\,\text{GeV}$$

    where p_T^{jet1} is uncorrected transverse momentum of the leading jet
  - primary vertex has to have at least five associated tracks
  - z coordinate (along the beam axis) of the primary vertex is within 50 cm from the origin: $|z_{vtx}| < 50\,\text{cm}$
- **normalisation condition**
  - event must belong to the Luminosity Block with known luminosity

The first, topological, cuts define the inclusive central dijet sample. This sample is very clean because it is hard to produce two fake high p_T central jets with large invariant dijet mass. The level of background pollution would be much higher in the case of single jet inclusive sample. The event quality criteria are designed to remove remaining possible background of fake dijet-like events. They are discussed in the following.

9.2 Jet identification criteria

Not all the objects identified by the jet algorithm are true jets necessarily. For example, electrons and photons produce also calorimeter showers. In addition to these natural sources of jets, there is a large number of processes that may create jet-like objects in the calorimeter. Firstly, fake jet-like objects could be produced in events not associated with the hard $p\bar{p}$ collision itself like in cosmic event or in beam-gas interaction. The other source of fake jets comes from the hardware errors such as failure in baseline subtraction of calorimeter cell energy or hot cell due to high voltage discharge.

In order to eliminate those fake jets, standard jet identification criteria were developed by the DØ experiment [62]. They are based on longitudinal and transverse properties of calorimeter showers. In the following, for each individual cut, the distribution of the cut variable is given for the two leading jets from the dijet sample. All central dijet sample selection criteria except the jet identification cuts are applied for this purpose. The distributions are made for each jet trigger separately. Moreover, only events with a dijet mass above the trigger turn-on point are considered (see section 11.2).

Cut on electromagnetic fraction (EMF) Electromagnetic fraction is a fraction of jet transverse energy that was deposited in the EM part of the calorimeter. The EMF distributions for the two leading jets in the dijet sample are plotted in Fig. 23. A typical jet stores about 50% of its energy in the EM part of the calorimeter. This number agrees with an estimate $e^{-0.76} \approx 0.47$ derived from the known depth of the EM calorimeter which is

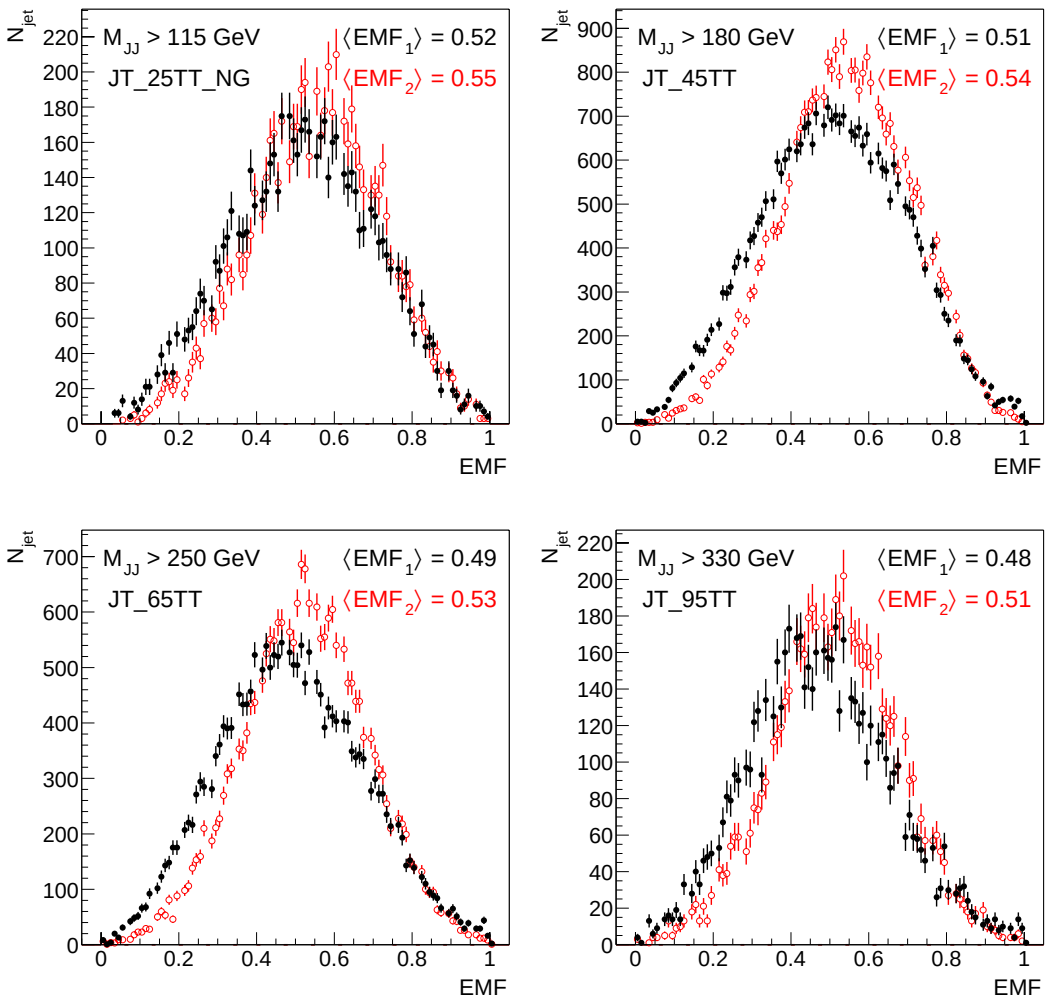

Figure 23: Electromagnetic fraction for jets from the dijet sample. Full circles are for the leading jet and open circles correspond to the second leading jet.

$0.76\lambda_I$. However, hadronic showers are subject of large fluctuations and jets with EMF < 0.15 or EMF > 0.85 are quite common. The leading and the second leading jets show slightly different behaviour. The EMF distribution is shifted consistently to the left in the case of the leading jet. The leading jet is usually the one that fired a given trigger. Its longitudinal and transversal shape can be therefore distorted by additional trigger conditions. This trigger bias explains partially the different properties of the leading and second leading jets. The other reason is the difference in the jet transverse momenta. The leading jets are more energetic than second leading jets naturally. There is a weak dependence of mean jet EMF on jet p_T; more energetic jets deposit in the EM part smaller fraction of their energy. However, it explains the difference between the leading jet and the second leading only partially.

Jets are required to have an electromagnetic fraction within the interval of $0.05-0.95$. No apparent anomaly is presented in the low EMF region (may be except the case of trigger `JT_25TT_NG`) and EMF > 0.05 cut removes only few events. On the other hand, there is a visible enhancement in the region around $EMF \sim 1$. This is the region where EM objects (electrons and photons) are expected to appear. Most of these objects are removed by the EMF < 0.95 cut.

Cut on coarse hadronic fraction (CHF) Coarse hadronic fraction is defined as a fraction of jet transverse energy that was deposited in the coarse hadronic part of the calorimeter. The CHF distributions for the two leading jets in the dijet sample are plotted in Fig. 24. A typical jet stores about 5% of its energy in the CH part of the calorimeter. Since the depth of material in front of the CH part is about $4\lambda_I$, jets are expected to deposit there only about 2% of energy on average. The discrepancy is probably caused by the noise in the CH part which is itself the noisiest part of the calorimeter. Noisy CH cells are picked up by the jet algorithm and they increase the jet CH energy nominally. The problem of CH noise is still under a study in the DØ experiment. New ideas how to avoid the problems were proposed

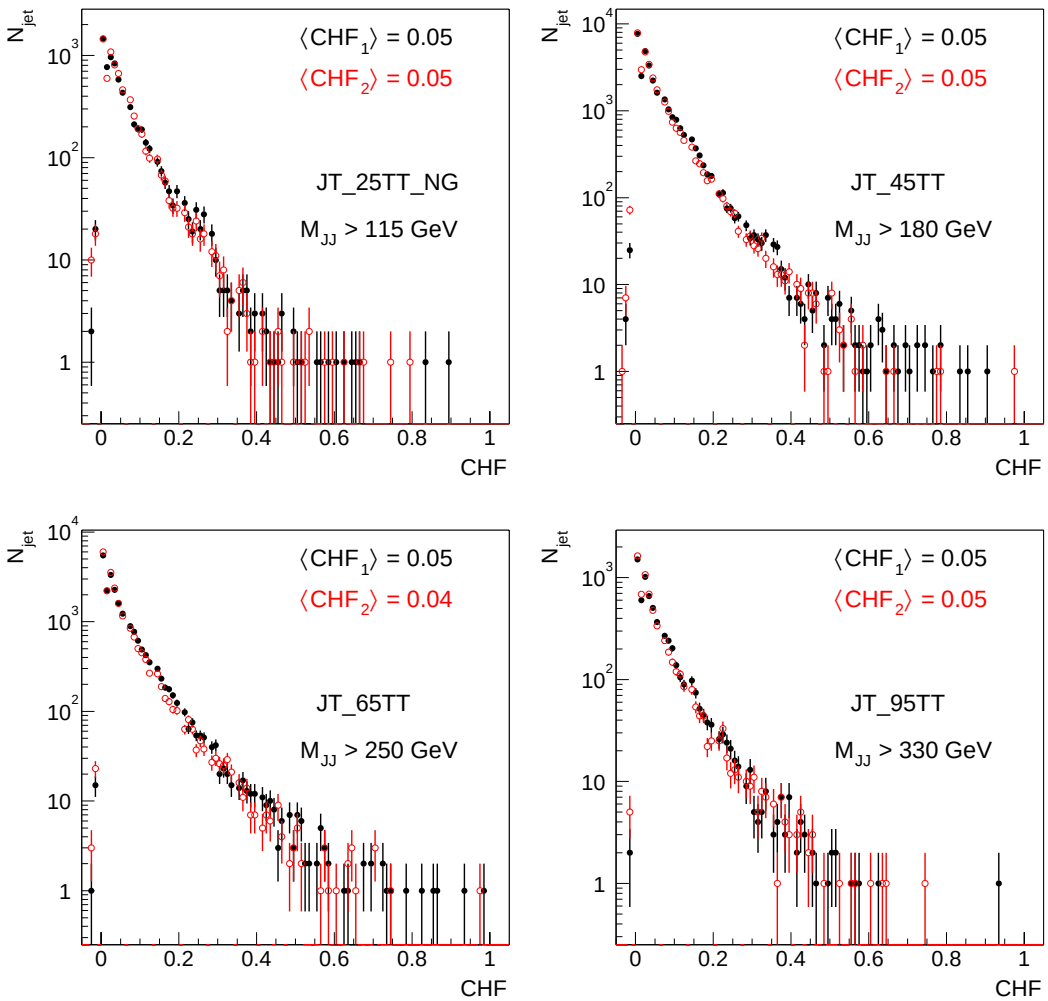

Figure 24: Coarse hadronic fraction for jets from the dijet sample. Full circles are for the leading jet and open circles correspond to the second leading jet.

recently. One of them removes CH cells from the starting seeds in the jet algorithm unless the signal from the CH cell is 4σ above the cell noise. The effect is important for low p_T jets but it is marginal for jets above 40 GeV from the dijet sample. As can be seen in Fig. 24, the CHF distributions for the two leading jets in the lowest p_T trigger do not show any peculiar behaviour at all.

The cut on CHF is loose. The jets are required to deposit in CH part less than 40% of their transverse energy: CHF < 0.4. The cut is intented to remove jets with noisy cells in the CH calorimeter layers.

Cut on hot cell fraction (HotF) Hot cell fraction is calculated as the ratio of the transverse energy of the leading cell in the jet to the transverse energy of the second leading cell. The HotF distributions for the two leading jets (Fig. 25) are steeply falling with increasing HotF. Jets formed by one hot cell are expected to have high HotF. Indeed, a plateau starts to appear at HotF ~ 10 indicating that the jets from the plateau are fake.

The cut on HotF is HotF < 10. It is designed to remove jets that are constituted by calorimeter hot cells not identified during the reconstruction by NADA (defined in section 3.1.4).

Cut on n90 variable The n90 variable is defined as a number of towers that contains 90% of jet transverse energy. For this purpose, the jet towers are ordered in transverse energy starting from the most energetic tower. The variable is connected with the transversal size of the jet. The n90 distributions for the two leading jets in the dijet sample are plotted in Fig. 26. The leading jets are slightly narrower than the second leading ones. It cannot be explained by different p_T of the two jets; even the second leading jets from `JT_95TT` sample with average p_T of ~ 150 GeV are wider than the leading jets from `JT_25TT_NG` sample with $p_T \sim 60$ GeV. There are two sources of the discrepancy. As in the case of EMF distribution, the difference could be caused by the trigger bias. The other explanation is that the second leading jets are more often merged during the jet reconstruction than the leading

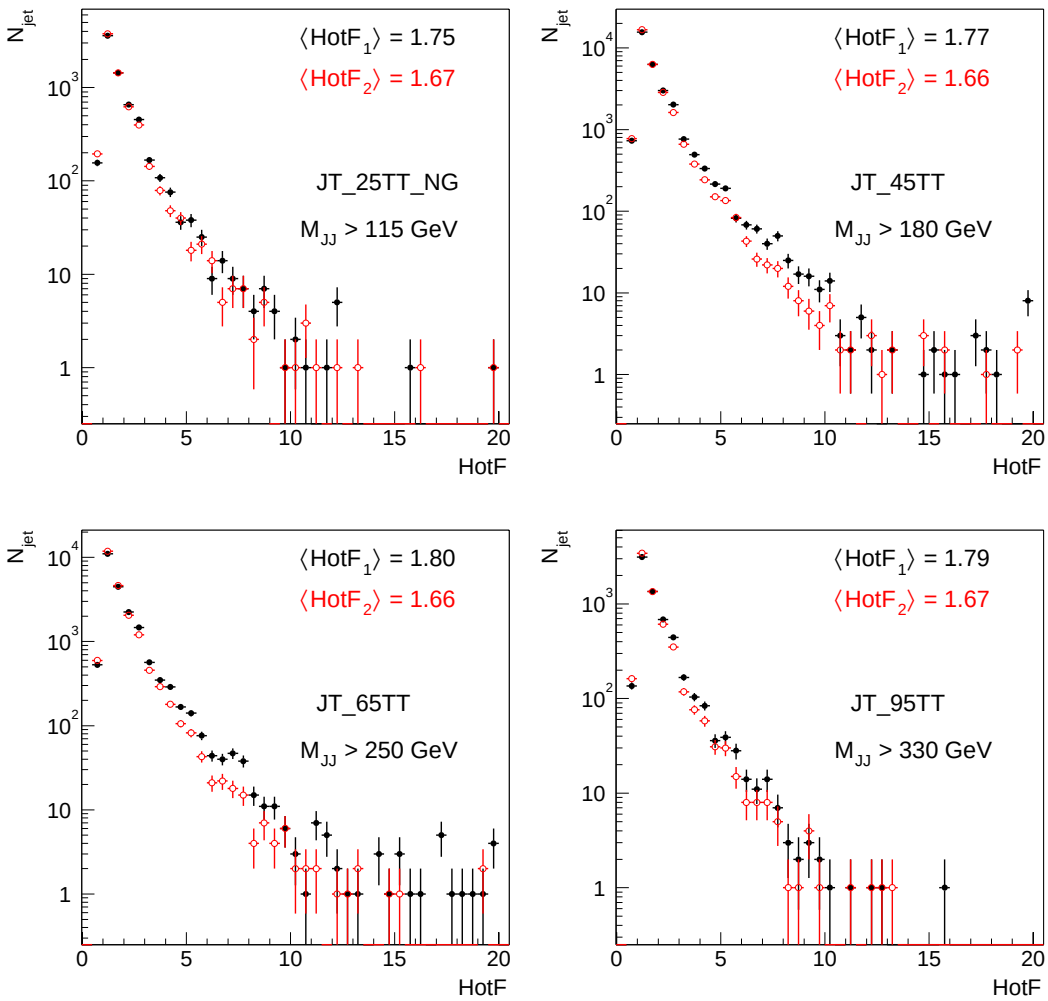

Figure 25: Hot cell fraction for jets from the dijet sample. Full circles are for the leading jet and open circles correspond to the second leading jet.

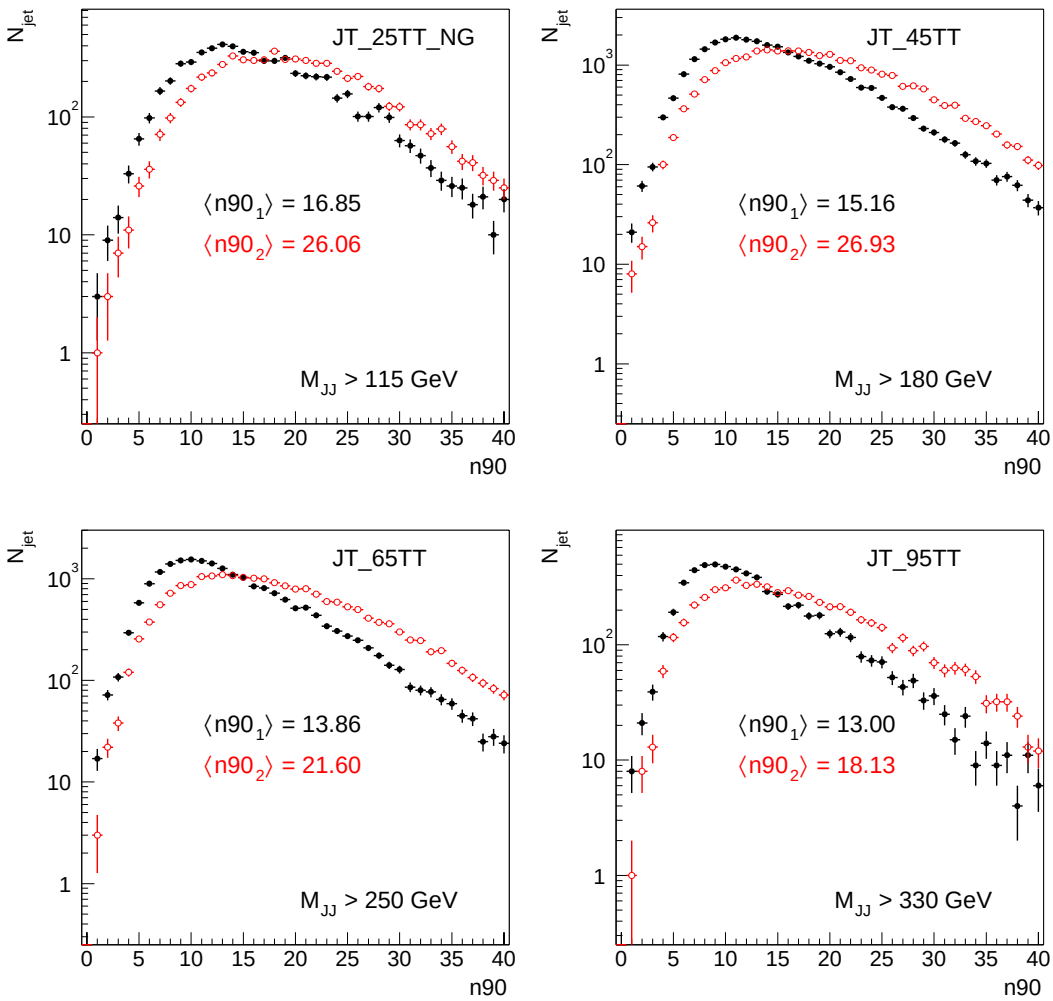

Figure 26: The distributions of n90 variable for jets from the dijet sample. Full circles are for the leading jet and open circles correspond to the second leading jet.

ones.

The cut on n90 variable is very loose; jets are required to have n90 > 1. It is intended to remove jets that are constituted by one hot tower. As can be seen in Fig. 26, the cut removes only few jets from the dijet sample.

Cut on f90ch variable The f90ch variable is defined as f90ch = f90 + 0.5 CHF, where f90 = n90/n_{towers} is fraction of jet towers carrying 90% of jet transverse energy. The f90ch distribution (Fig. 27) shows one distinct peak at ~ 0.3 and a flat tail above 0.6. Jets built from the CH noise are expected to have large CHF and n90, therefore high f90ch. However, merged jets are also expected to have large n90 and not all jets with high f90ch are fake necessarily.

Jets are required to have either CHF < 0.1 or f90ch < 0.8. The cut is intended to remove remaining fat jets built out of the CH noise that survived the CHF cut.

9.2.1 Efficiencies of jet selection criteria

Efficiencies of jet selection criteria are determined for each particular cut independently. The leading jet and second leading jet are treated separately since their properties are slightly different. Efficiency ε and its error σ_ε are calculated according to

$$\varepsilon = \frac{N_{all} - N_{cut}}{N_{all}}, \qquad \sigma_\varepsilon = \sqrt{\frac{\varepsilon\,(1-\varepsilon)}{N_{all}}}, \tag{34}$$

where N_{all} is a total number of jets in the distribution and N_{cut} is number of good jets that are rejected by the cut. This formula assumes that the contamination of bad events with fake jets is small. N_{cut} is estimated using a fit of a given jet identification variable near the actual value of the cut. But only the good jets (i.e. those satisfying the selection criterion) are considered in the fit. The fit is then extrapolated to the rejection region and N_{cut} is calculated from the integral of the fit over this region.

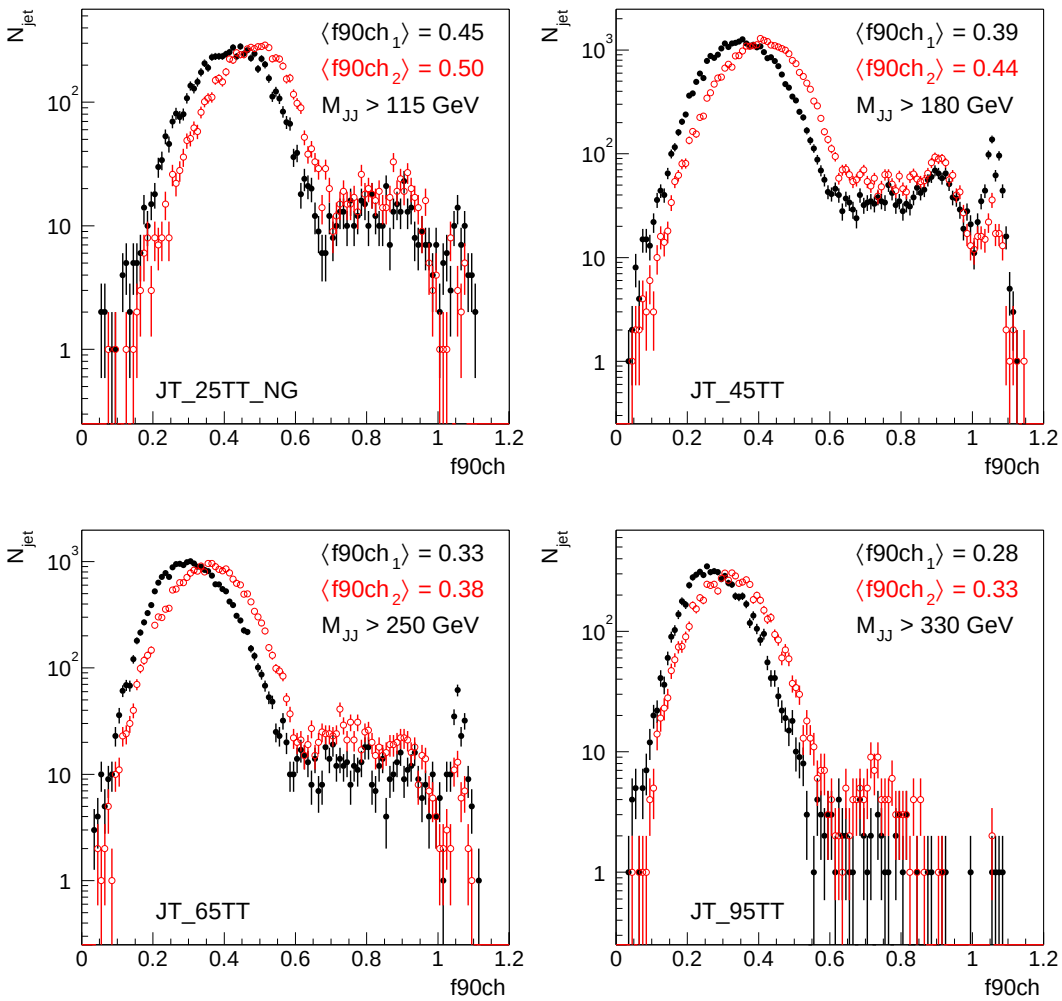

Figure 27: The distributions of f90ch variable for jets from the dijet sample. Full circles are for the leading jet and open circles correspond to the second leading jet.

The procedure is illustrated in Fig. 28 for the case of the leading jets in one particular p_T bin ($80 - 120$ GeV). In the first step, the EMF distribution is plotted for the leading jets in all central dijet events that satisfy only event selection criteria on vertex and missing E_T but no selection is applied on jet identification variables. $N_{<0.05}$ and $N_{>0.95}$ represent the number of jets with EMF < 0.05 and EMF > 0.95 respectively. The efficiencies ε_{min} calculated from these numbers correspond to the limit case as if all jets were considered good. Solid lines represent the fits around the cut values, $N^{fit}_{<0.05}$ and $N^{fit}_{>0.95}$ are the estimates of the number of good jets that did not pass the cuts. There is no apparent bump at the low EMF end of the distribution. Therefore, the fit gives roughly the same estimate on the number of good jets below the cut of 0.05 as the real number of jets in this region. On the contrary, due to presence of a bump at EMF ~ 1, the high EMF end fit leads to a significantly smaller number of good jets with EMF above 0.95 than the total number of jets above the cut. The difference between ε_{min} and the efficiency obtained from the fit is used as an estimate of systematic uncertainty.

In the second step, the CHF cut efficiency is determined from the CHF distribution which is drawn only for the jets that passed the cut on EMF. Again, the jets that satisfy the cuts on EMF and CHF are used to calculate the efficiency of HotF cut in the next step. No estimate is made for the cut on n90 variable since almost all jets with n90 $= 1$ are rejected by the hot cell fraction cut already. Thus, the efficiency of this cut is considered to be one. The efficiency of the cut on the f90ch variable is evaluated in the last step. The right plot on the bottom of Fig. 28 shows the f90ch distribution for jets that passed all previous cuts (solid line) and also the f90ch distribution for jets with CHF > 0.1 (dashed line) since only these jets might be rejected by the f90ch cut. As was discussed above, jets with f90ch > 0.8 are not bad necessarily. It is hard to estimate how many of them are really fake. The efficiency is calculated under the assumption that half of jets removed by the cut are good. The difference from one is then treaded as a systematic error.

The results on efficiencies of jet selection criteria for the leading jet are

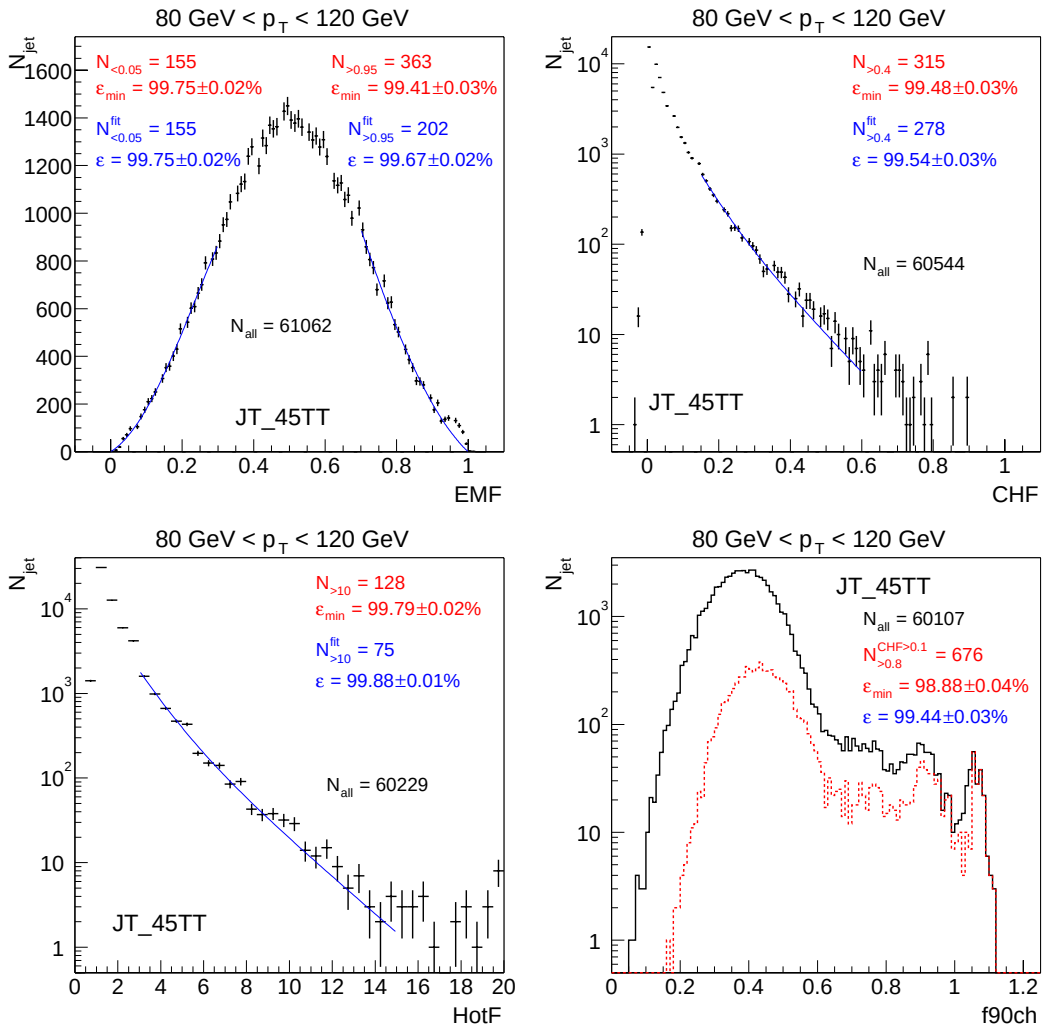

Figure 28: Efficiencies of jet selection criteria for the leading jet with p_T in the interval $80 - 120$ GeV from the dijet sample. Solid line in the bottom right plot represent the f90ch distribution for all jets passing the previous cuts. Dashed line corresponds to the jets with CHF > 0.1.

ε_{jet1}	p_T bin [GeV]			
	50 − 80	80 − 120	120 − 160	160 − 250
EMF > 0.05	0.9981(4)	0.9975(2)	0.9973(3)	0.9977(5)
sys. err.	0.0002	0.0000	0.0002	0.0003
EMF < 0.95	0.9959(5)	0.9967(2)	0.9963(4)	0.9976(5)
sys. err.	0.0003	0.0026	0.0021	0.0024
CHF < 0.4	0.9960(5)	0.9954(3)	0.9956(4)	0.9953(7)
sys. err.	0.0003	0.0006	0.0009	0.0008
HotF < 10	0.9992(2)	0.9988(1)	0.9989(2)	0.9991(3)
sys. err.	0.0010	0.0009	0.0008	0.0006
n90 > 1	1	1	1	1
f90ch < 0.8	0.9944(6)	0.9944(3)	0.9961(4)	0.9997(2)
sys. err.	0.0056	0.0056	0.0039	0.0003
total	**0.984(1)**	**0.9828(5)**	**0.9843(7)**	**0.989(1)**
sys. error	~ 0.006	~ 0.006	~ 0.005	~ 0.003

Table 5: Efficiencies of the jet selection criteria for the leading jet in the dijet sample as a function of jet p_T.

summarised in Tab. 5. Statistical errors are calculated according to Eq. 34. All efficiencies, except the one on f90ch cut, show almost no dependence on jet p_T. The efficiency for the f90ch cut itself increases from 99.4% in the lowest p_T bin to almost 100% in the highest p_T bin. As a result, the total efficiency, calculated as a product of efficiencies of all particular jet selection criteria, also improves with increasing p_T. The systematic error is dominated by the error on f90ch efficiency except the highest p_T bin.

Since the properties of the leading and the second leading jets are slightly different, the efficiencies for the second leading jet are not expected to be the same. Therefore, the whole procedure was repeated for the second leading jets in the dijet sample. The result is listed in Tab. 6. In general, EMF, CHF, and HotF cuts are more efficient in the case of the second leading jet. On the

ε_{jet2}	p_T bin [GeV]			
	50 − 80	80 − 120	120 − 160	160 − 250
EMF > 0.05	0.9998(2)	0.9998(1)	0.9995(2)	0.9995(4)
sys. err.	0.0002	0.0001	0.0002	0.0005
EMF < 0.95	0.9993(3)	0.9993(2)	0.9971(5)	0.9986(6)
sys. err.	0.0007	0.0007	0.0005	0.0009
CHF < 0.4	0.9986(5)	0.9974(3)	0.9966(6)	0.995(1)
sys. err.	0.0014	0.0001	0.0004	0.001
HotF < 10	0.9998(2)	0.9997(1)	0.9999(1)	0.9996(3)
sys. err.	0.0002	0.0003	0.0001	0.0001
n90 > 1	1	1	1	1
f90ch < 0.8	0.990(1)	0.9900(6)	0.9973(5)	0.9999(2)
sys. err.	0.010	0.010	0.0027	0.0001
total	**0.988(1)**	**0.9863(8)**	**0.9904(9)**	**0.993(1)**
sys. error	~ 0.01	~ 0.01	~ 0.003	~ 0.001

Table 6: Efficiencies of the jet selection criteria for the second leading jet in the dijet sample as a function of jet p_T.

contrary, f90ch cut removes more second leading jets with $p_T < 120$ GeV. In the end, the overall efficiency is almost the same for those jets as in the case of the leading jet efficiency.

The efficiency of jet selection criteria is applied event by event. Each event is weighted by factor of $1/(\varepsilon_{jet1}\varepsilon_{jet2})$, where ε_{jet1} and ε_{jet2} are efficiencies for the leading and second leading jets. The actual values of efficiencies are used as listed in Tab. 5 and Tab. 6. If the jet transverse momentum is smaller than 50 GeV the value from the lowest p_T bin is used. Analogously, the efficiency from the highest p_T bin is applied for jets with $p_T > 250$ GeV.

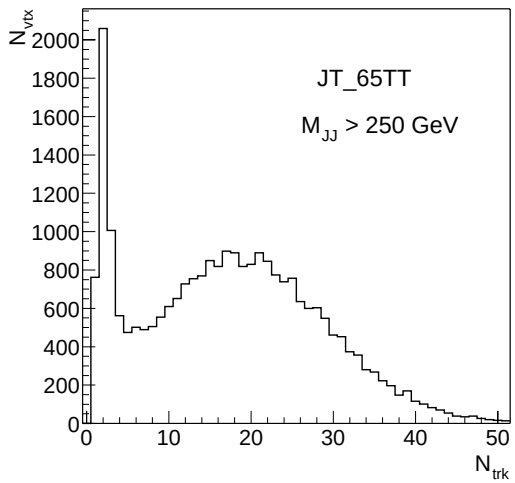

Figure 29: Distribution of the number of tracks associated with the main primary vertex in dijet events passing trigger `JT_65TT`.

9.3 Vertex cut

New DØ tracking system is able to distinguish two kinds of vertexes; *primary vertexes* are associated with the $p\bar{p}$ interactions, *secondary vertexes* correspond to the decays of relatively long living particles (Λ, b-mesons, etc.). While the position of the primary vertex matches the beam position, secondary vertexes are characterised by a displacement from the beam spot in the plane perpendicular to the beam.

Requiring a primary vertex yields a more pure selection of events and is necessary to compute correct jet rapidity and transverse momentum. There are two cuts applied on vertex. The first one ensures the good quality of primary vertex. As is shown in Fig. 29, an enhancement of primary vertexes with low track multiplicities (< 5) is observed in the data with a low precision on the vertex position. Therefore, only vertexes with at least 5 associated tracks are considered in the analysis. The second one is a cut on the primary vertex position. The vertex is required to be within 50 cm along the beam axis from the center of the detector, i.e $|z_{vtx}| < 50$ cm where z_{vtx} is the vertex

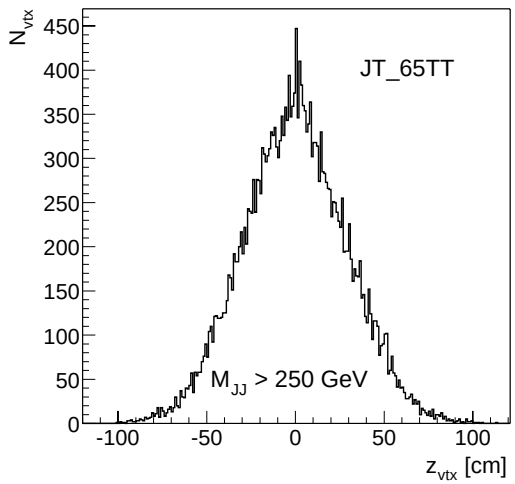

Figure 30: Distribution of the primary vertex z coordinate in the central dijet events passing the trigger `JT_65TT`.

z-coordinate. The distribution of the vertex z-position is displayed in Fig. 30. The cut is intended to remove events that occur in the edge of the central Silicon Microstrip Tracker. Another reason for this cut is that the calorimeter towers are no more projective in the case of events with large $|z_{vtx}|$.

Since several $p\bar{p}$ interaction may occur in one bunch crossing, more than one primary vertex might be identified in one event. On average, about 15% of events in the dijet sample contain at least two primary vertexes with at least five associated tracks. However, not all reconstructed primary vertexes correspond to different $p\bar{p}$ interactions. About 40% of them have almost identical z-position as the main primary vertex as is shown in Fig. 31, where the distance along the beam between the other primary vertexes and the main primary vertex is plotted for the dijet events passing trigger `JT_65TT`. The reason why so many duplicate primary vertexes are found in the data is that the p13 reconstruction software underestimates the tracking errors. Consequently, the errors on vertex positions are also underestimated which results in reconstruction of close but distinct vertexes although the tracks originate from the same physical vertex.

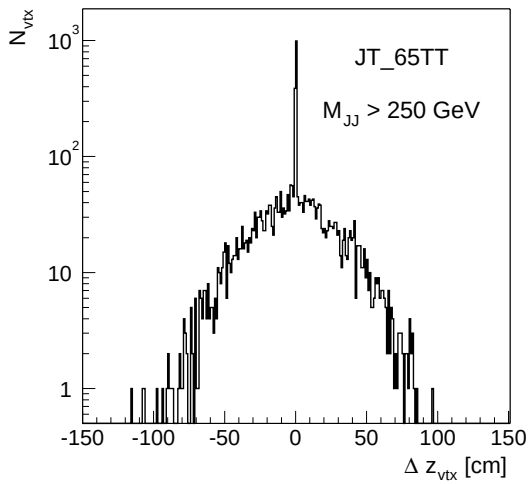

Figure 31: Distance along the beam between the other primary vertexes and the main primary vertex in the central dijet events passing the trigger `JT_65TT`. Only vertexes with at least five associated tracks were considered.

Ignoring those similar vertexes, about 9% of events show another primary vertex coming from different $p\bar{p}$ interaction. The additional $p\bar{p}$ interactions are not biased by trigger. They are therefore called *minimum bias* interactions. Typically, they are very soft since the $p\bar{p}$ cross section sharply peaks at low p_T. The question is how to recognise correct primary vertex that is associated with the hard interaction. The p13 release of the reconstruction software singles out the one with the largest value of the sum of $\log(p_T)$ of associated tracks. According to the study made by the vertex group on e+jet sample, the primary vertex of the hard interaction is not correctly assigned in 20% of the events. No such study was made on the dijet sample. But if the level of misidentification is similar then about 1.8% of dijet events have a wrong assignment of the primary vertex. A wrong selection of vertex also spoils the reconstruction of directions and transverse momenta of jets in the event. So, it has a direct impact on jet and dijet mass resolutions. Therefore, it is important to keep the same event selection criteria for the dijet sample in the dijet mass analysis as in the dijet sample in the case of the jet resolution

analysis. Both samples then contain the same mixture of events with wrong primary vertexes and the effect of vertex misidentification is, at least in the first order, corrected during the unsmearing procedure.

9.3.1 Vertex cut efficiency

The efficiency of the vertex cut is calculated as a ratio of the number of events from our dijet sample that satisfy all selection criteria, N_{cut}, to the number of events that satisfy all selection criteria except the cut on vertex, N_{all},

$$\varepsilon_{vtx} = \frac{N_{cut}}{N_{all}}\,, \qquad \Delta\varepsilon_{vtx} = \sqrt{\frac{\varepsilon\,(1-\varepsilon)}{N_{all}}}\,. \tag{35}$$

While not too many fake events (beam gas interaction, cosmic, etc.) are expected in the dijet sample when there is a primary vertex with at least 5 associated tracks, the sample with no reconstructed primary vertex or with vertex with less than 5 tracks may not be that clean and may contain a significant fraction of fake events. Thus it is important to distinguish the contribution coming directly from the z_{vtx} cut and the contribution due to the requirement of reconstructing a vertex with 5 tracks attached to it. For this purpose we define the following efficiencies

$$\varepsilon_{vtx1} = \frac{N_{cut}}{N_{5tr}}\,, \qquad \text{and} \qquad \varepsilon_{vtx2} = \frac{N_{5tr}}{N_{all}}\,, \tag{36}$$

where N_{5tr} is number of events from our dijet sample that satisfy all selection criteria except the cut on the z-position of the vertex (i.e. events with primary vertexes with at least 5 tracks).

For the purpose of study of potential dependence on dijet mass M_{JJ}, the vertex cut efficiency is obtained for every jet trigger independently. Only the events with dijet mass above the trigger turn-on points are considered in the calculation (the determination of dijet mass turn-on points is discussed later on in section 11.2).

Fig. 32 shows the z-position distribution of the primary vertex in dijet events for all primary vertexes (events with no vertex were put at $z_{vtx} = 0$),

trigger	M_{JJ} cut	ε_{vtx1}	ε_{vtx2}	ϵ_{vtx}
JT_25TT_NG	115 GeV	0.953 ± 0.003	0.825 ± 0.004	0.787 ± 0.005
JT_45TT	180 GeV	0.952 ± 0.001	0.827 ± 0.002	0.787 ± 0.002
JT_65TT	250 GeV	0.958 ± 0.001	0.825 ± 0.002	0.790 ± 0.003
JT_95TT	330 GeV	0.963 ± 0.002	0.818 ± 0.004	0.788 ± 0.005

Table 7: Vertex cut efficiency.

for events with a primary vertex with at least 5 tracks (blue hatch style histogram) and for events with a primary vertex with at least 5 tracks and with $|z_{vtx}| < 50\,\mathrm{cm}$ (shaded region). The efficiencies calculated from these plots are summarised in Table 7.

There is a small dijet mass dependence of the cut on vertex z-position in the data. However, the overall efficiency of vertex cut does not show any mass dependence. The efficiency values in different jet triggers are consistent with a constant number $\varepsilon = 0.788$. This sole number is therefore applied to correct for the vertex cut efficiency for all events.

9.4 Cut on missing transverse energy

An additional cut on overall p_T balance in the event is applied in order to clean up the dijet mass sample. The events from the dijet sample are required to fulfil a weak cut on missing transverse energy $\not{E}_T$

$$\not{E}_T < 0.7 p_T^{jet1} \quad \text{for} \quad p_T^{jet1} < 250\,\mathrm{GeV}\,,$$
$$\not{E}_T < 175\,\mathrm{GeV} \quad \text{for} \quad p_T^{jet1} > 250\,\mathrm{GeV}\,,$$

where p_T^{jet1} is the transverse momentum of the leading jet before jet energy scale correction. The cut $\not{E}_T < 175\,\mathrm{GeV}$ had to be introduced because the missing E_T value stored in thumbnail files is in packed format and there is a an upper limit on it. Missing E_T is calculated from calorimeter cells with

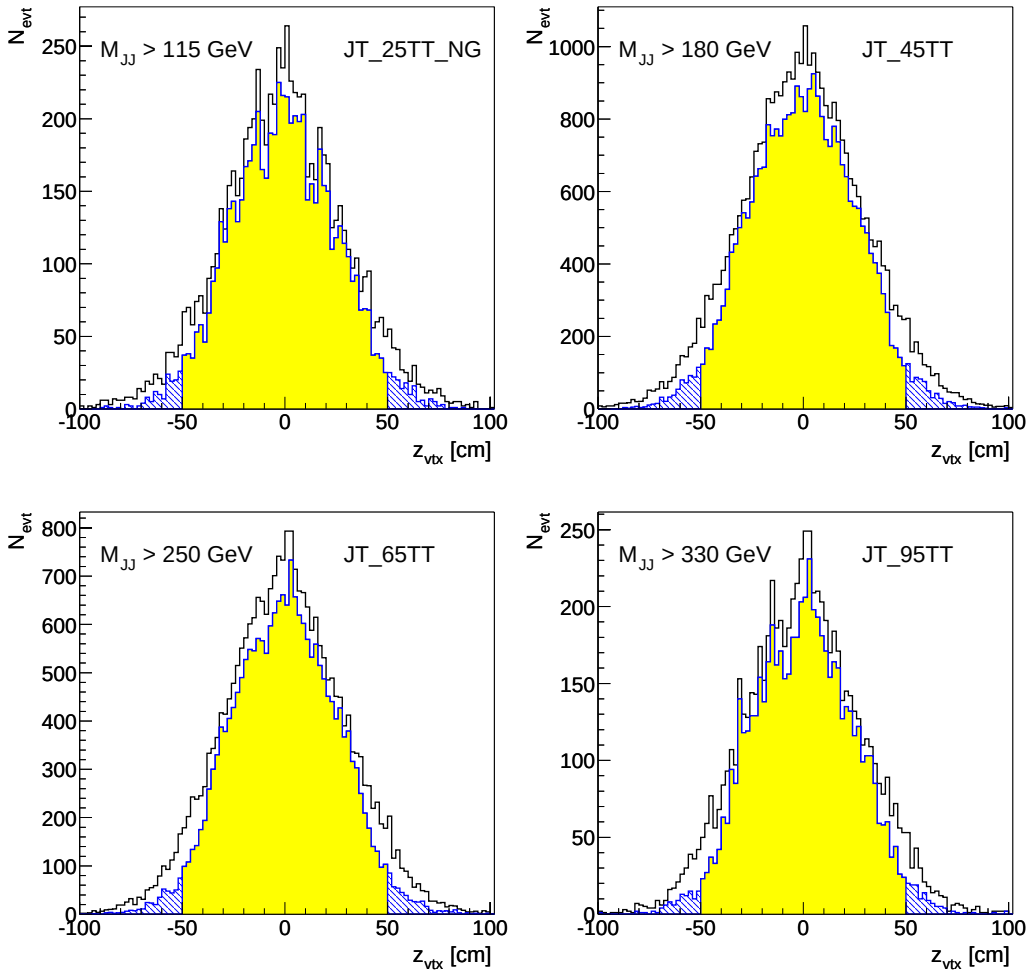

Figure 32: The z-position distribution of the primary vertex for the events from the dijet sample for all primary vertexes (solid line), for events with a primary vertex with at least 5 tracks (blue hatch style histogram) and for events with a primary vertex with at least 5 tracks and with $|z_{vtx}| < 50\,\mathrm{cm}$ (shaded region).

Trigger	M_{JJ} cut	$\langle M_{JJ} \rangle$	ε
JT_25TT_NG	115 GeV	148 GeV	0.9935 ± 0.0010
JT_45TT	180 GeV	225 GeV	0.9966 ± 0.0003
JT_65TT	250 GeV	305 GeV	0.9989 ± 0.0002
JT_95TT	330 GeV	393 GeV	1.0000 ± 0.0001

Table 8: Efficiency of the $\not\!\!E_T$ cut for central dijet events.

$E_T^{cell} > 100\,\mathrm{MeV}$ according to

$$\not\!\!E_T = |\sum_{E_T^{cell} > 0.1\,\mathrm{GeV}} \vec{E}_T^{cell}|\,, \tag{37}$$

where $\vec{E}_T^{cell} \equiv (E_x^{cell}, E_y^{cell}) = E_T^{cell}(\cos\phi^{cell}, \sin\phi^{cell})$ is the transverse energy vector of the cell. The cut is intended to remove events with large $\not\!\!E_T$. Possible sources could be cosmic events or events with hot cells which did not cause the leading two jets to be bad but which still spoiled $\not\!\!E_T$ in the event. However, the number of background events with large $\not\!\!E_T$ is already significantly reduced in the dijet sample by the requirement of two central jets with high invariant dijet mass.

The efficiency of the $\not\!\!E_T$ cut is determined in a similar way as in the case of jet identification cuts. Fig. 33 displays the $p_T^{jet1}/\not\!\!E_T$ distributions in the central dijet events with $p_T^{jet1} < 250\,\mathrm{GeV}$ for all four considered jet triggers. For this purpose, all cuts except the one on $\not\!\!E_T$ have been applied. Also, the dijet mass was required to be above the trigger turn-on point. Events rejected by the cut lie below the point of $1/0.7 \sim 1.43$. The efficiencies are summarised in Tab. 8. The strict 175 GeV cut on $\not\!\!E_T$ for events with leading jet transverse momentum above 250 GeV removes almost no event. There is only one event in the entire dijet sample that does not pass the cut. Therefore, the efficiency of this cut is assumed to be 1.

The efficiency shows small dependence on dijet mass. In order to obtain the efficiency as a smooth function of the mass, the four points from Tab. 8

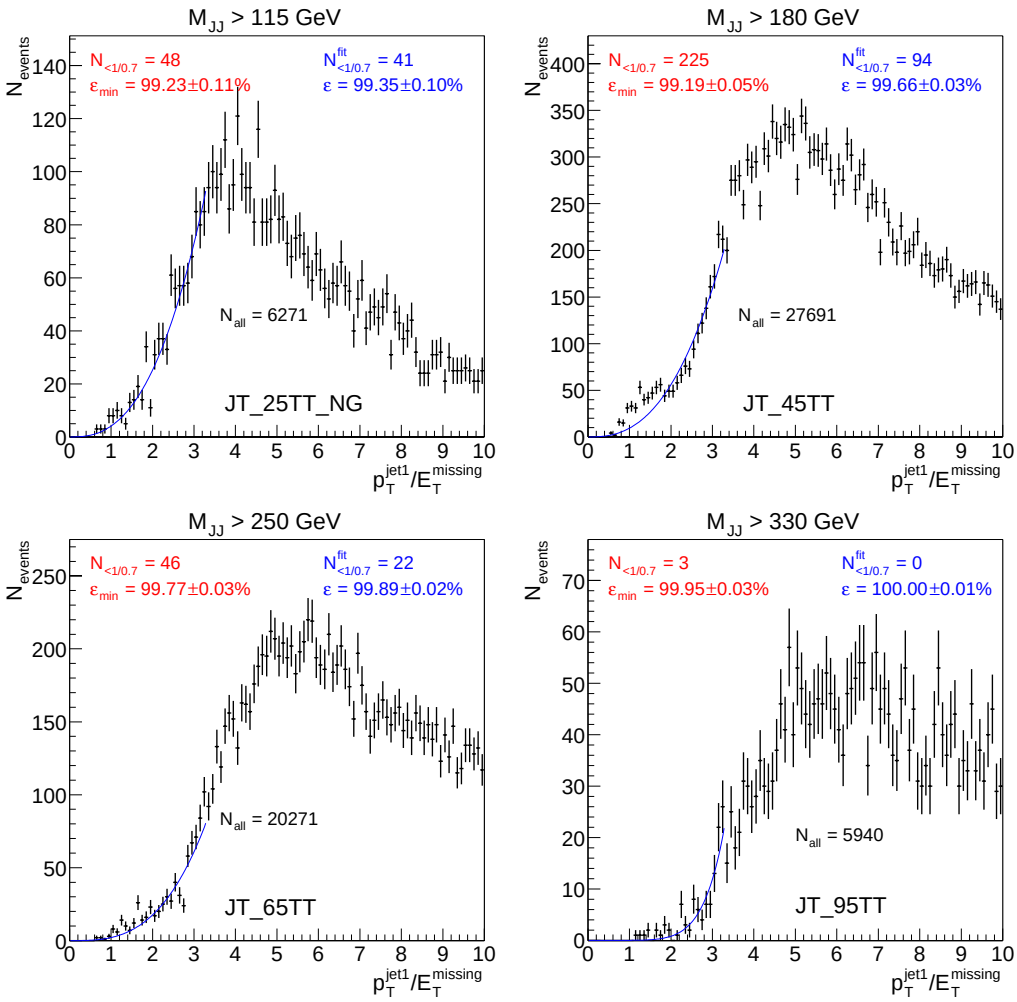

Figure 33: The distribution of the $p_T^{jet1}/\not{E}_T$ for events in the central dijet sample above trigger dijet mass turn-on points.

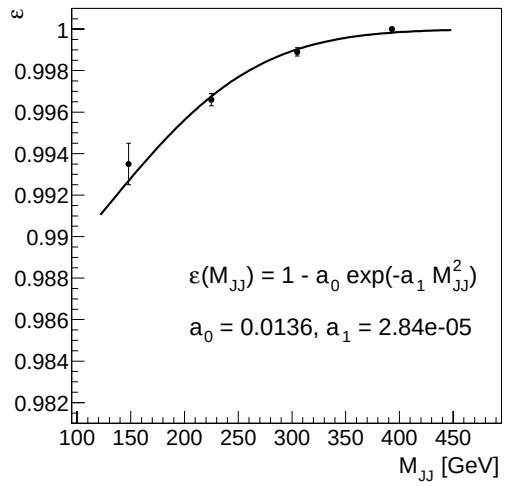

Figure 34: Efficiency of the cut on $\not\!\!E_T$ as a function of dijet mass. Solid line represents the fit from Eq. 38.

were fitted by

$$\varepsilon(M_{JJ}) = 1 - a_0 \exp(-a_1 M_{JJ}^2)\,. \tag{38}$$

The result of the fit is shown in Fig. 34. In the end, every event with dijet mass M_{JJ} is weighted by factor of $1/\varepsilon(M_{JJ})$ in order to take into account the efficiency of cut on $\not\!\!E_T$.

9.5 Jet distributions in the central dijet sample

Several basic jet distributions are checked for the events from the central dijet sample in this subsection.

The distribution of azimuthal angle ϕ for the two leading jets in the central dijet sample is displayed in Fig. 35. For this purpose, the distributions are made for the four jet triggers separately. Again, only the events with dijet mass above the trigger turn-on points are considered. As expected, the distribution is flat. However, the closer comparison with the constant line fit (solid line) reveals small anisotropy.

Fig. 36 shows the distribution of detector pseudorapidity η_{det} of the two

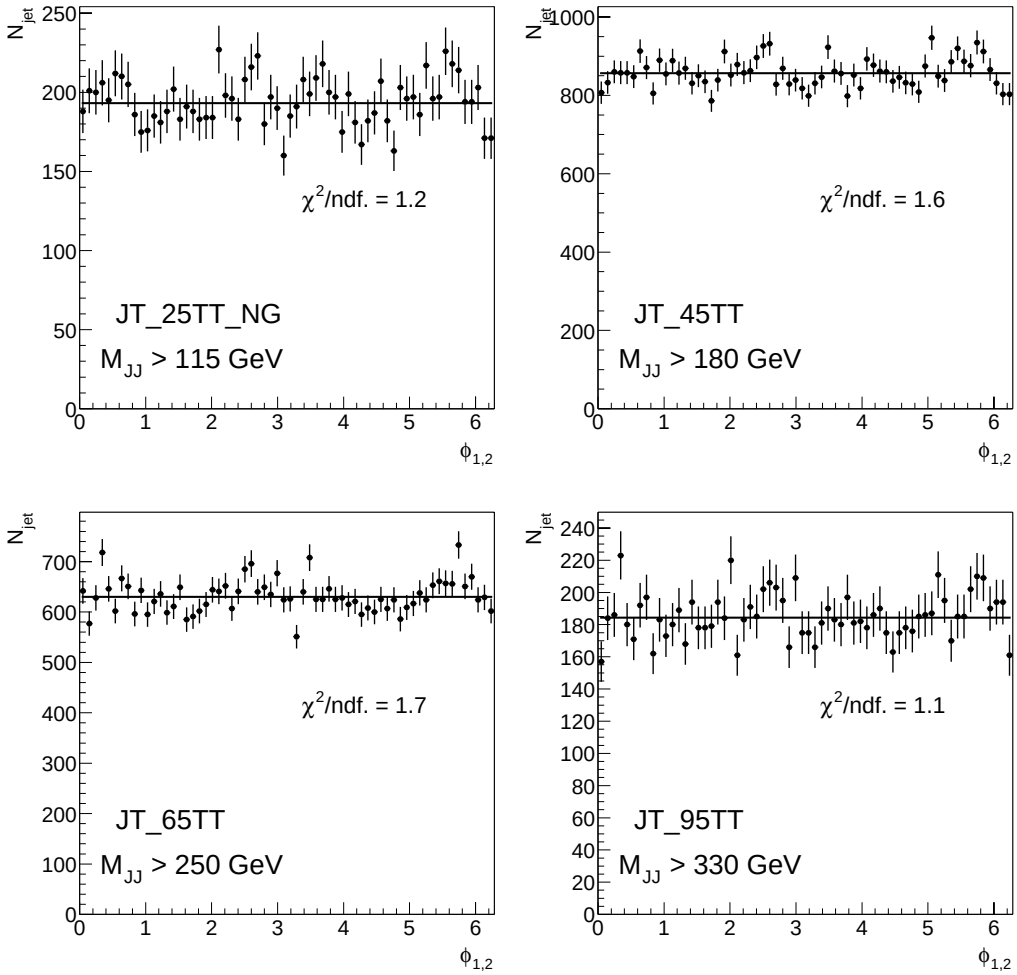

Figure 35: The distribution of azimuthal angle ϕ for the two leading jets in the selected events. Solid line represents the constant line fit.

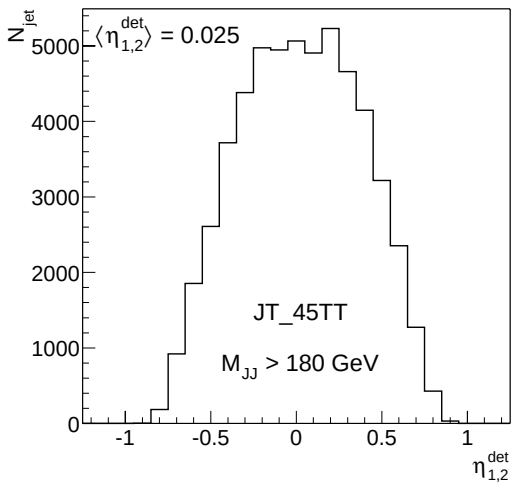

Figure 36: The distribution of detector pseudorapidity η_{det} of the two leading jets for events from the central dijet sample ($|y_{jet}| < 0.5$) that passed trigger JT_45TT.

leading jets for events from the dijet sample that passed trigger JT_45TT. The detector pseudorapidity is calculated from the polar angle ϑ that corresponds to the jet position as seen from the center of the detector (i.e. from $z = 0$ point). On the contrary, jet physics pseudorapidity η or rapidity y are calculated using the knowledge of the interaction vertex position. Physics (or true) rapidity is therefore suitable for physics analyses, while the detector coordinates determine the actual jet position in the detector. Although there is a cut on jet rapidities $|y_{jet}| < 0.5$, the tail in the detector pseudorapidity distribution goes up to $|\eta_{det}| \sim 0.9$. The reason why the analysis is restricted only to central jets with $|y_{jet}| < 0.5$ and why this region was not extended towards the higher values of rapidity is that already a small fraction of jets with $|y_{jet}| < 0.5$ started to touch the intercryostat region between the central and end-cap cryostats. As was discussed earlier, there is a known bug in the energy calibration of the Inter-Cryostat Detector which distorts the jet energy scale in the intercryostat region.

The detector pseudorapidity distribution is expected to be symmetric

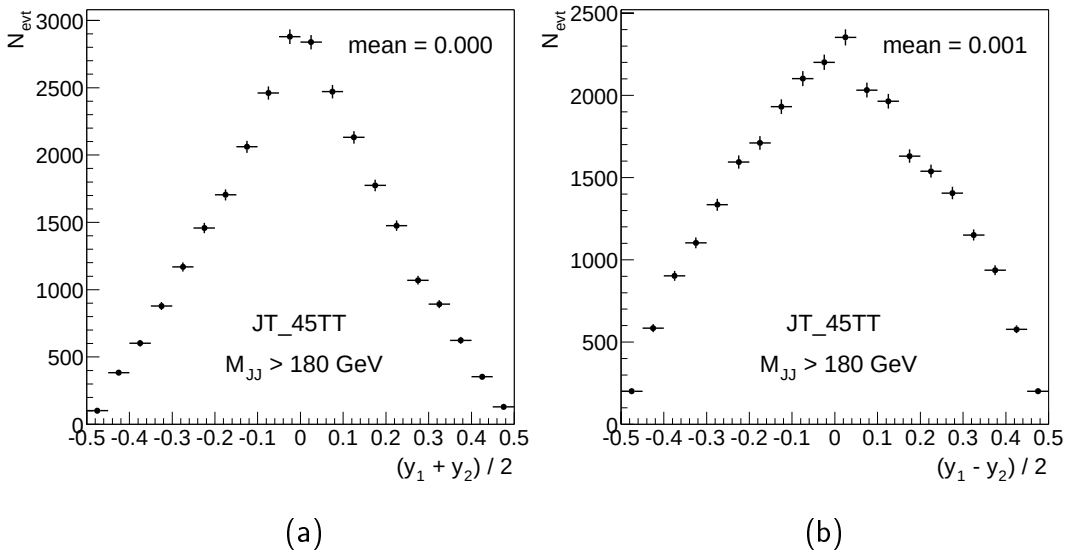

Figure 37: Average rapidity (a) and difference in jet rapidities (b) for the two leading jets in the central dijet sample in trigger `JT_45TT`.

according to y-axis. However, the mean value of the distribution is not zero but ~ 0.025. Moreover, the physics rapidity distributions, like the average dijet rapidity (Fig. 37a) or the difference in jet rapidities (Fig. 37b), do not show such asymmetry at all. The discrepancy is caused by a small shift of the calorimeter. Since the average distance of the jet center to the beam is about $\sim 1\,\mathrm{m}$, the magnitude of the shift is about $2.5\,\mathrm{cm}$. The DØ reconstruction software takes into account this shift. So, the physics quantities like jet rapidity are corrected for the shift.

The average dijet rapidity $(y_1 + y_2)/2$ corresponds to the rapidity of the centre of mass system (CMS) of the incident partons in the first approximation where the two jets are identified with the two outgoing partons in the hard matrix element. Similarly, the difference of jet rapidities $(y_1 - y_2)/2$ is directly connected to the scattering angle $\vartheta_\star$ of the outgoing partons in the CMS of the parton interaction. In the limit of massless jets, the pseudorapidity of the CMS is $\eta_{CMS} = (\eta_1 + \eta_2)/2$. The pseudorapidities of scattered

jets in CMS are then

$$\eta_{\star 1} = \eta_1 - \eta_{CMS} = \frac{\eta_1 - \eta_2}{2}\,, \quad \eta_{\star 2} = \eta_2 - \eta_{CMS} = -\frac{\eta_1 - \eta_2}{2}\,. \tag{39}$$

Scattering angle is connected with the jet pseudorapidity by

$$\cos\vartheta_\star = \tanh|\eta_\star| = \tanh\frac{|\eta_1 - \eta_2|}{2} \sim \tanh\frac{|y_1 - y_2|}{2}\,. \tag{40}$$

The last check is made on p_T spectra of the two leading jets. They are displayed in Fig. 38 for all four jet triggers. As expected, the distributions are steeply falling with increasing p_T with no obvious spikes.

Another distribution that was checked is the difference in azimuthal angle between the two leading jets: $\Delta\phi = |\phi_1 - \phi_2|$. The leading jets should be mostly back-to-back. Since the $\Delta\phi$ distribution is an interesting measurement that can be compared with pQCD predictions, it is discussed separately in section 12.

9.6 Instantaneous luminosity profile

A profile of the instantaneous luminosity per bunch crossing for events from the central dijet sample that passed trigger `JT_65TT` is given in Fig. 39. Each event represents one entry. In average, the instantaneous luminosity is $0.48 \times 10^{30}\,\mathrm{cm}^{-2}.\,\mathrm{s}^{-1}$ per bunch crossing. Corresponding mean number of interactions per bunch crossing can be calculated according to Eq. 26. In order to take into account all events (and not only those that would give a signal in the LM), the total $\mathrm{p\bar{p}}$ inelastic cross section $\sigma_{inel} = 58.8\,\mathrm{mb}$ has to be used instead of the effective $\mathrm{p\bar{p}}$ cross section σ_{eff}. Since the instantaneous luminosity is calculated per bunch crossing the beam crossing frequency in Eq. 26 has to be replaced by the revolution frequency $f_r = 47.713\,\mathrm{kHz}$. The formula for mean number of interactions per bunch crossing reads

$$\mu = \frac{\mathcal{L}\sigma_{inel}}{f_r}\,. \tag{41}$$

The actual value of μ that corresponds to the measured average instantaneous luminosity is then $\mu = 0.59$. Probability that high p_T event is accompanied

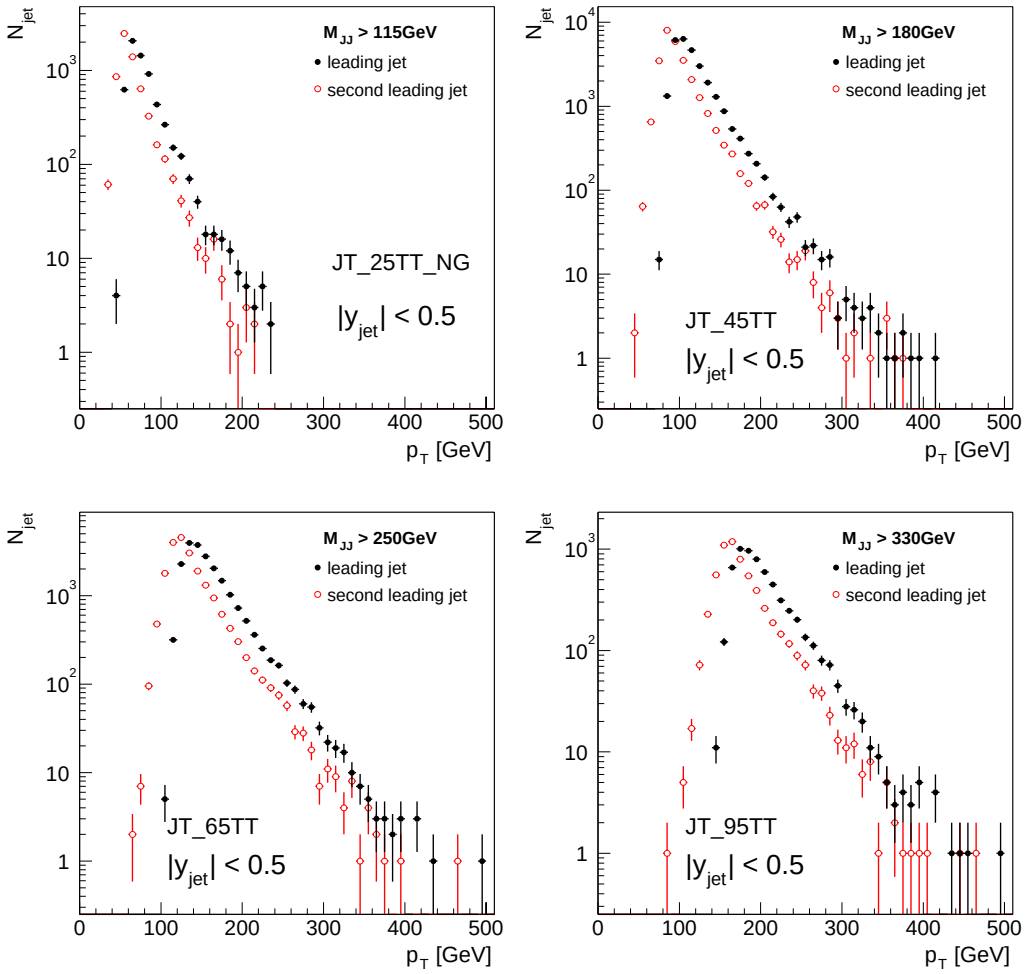

Figure 38: The transverse momentum distributions for the two leading jets from the central dijet sample in jet triggers.

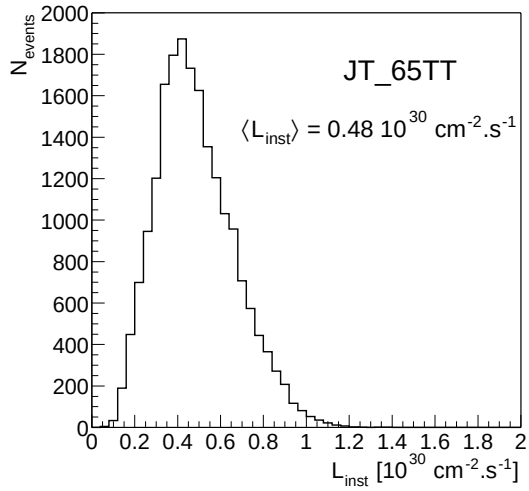

Figure 39: Profile of the instantaneous luminosity $\mathcal{L}_{inst}$ per bunch crossing for events from the central dijet sample that passed trigger `JT_65TT`.

by another interaction is

$$P(n > 1|n > 0) = \frac{P(n > 1)}{P(n > 0)} = \frac{1 - P(0) - P(1)}{1 - P(0)} = \frac{1 - e^{-\mu} - \mu e^{-\mu}}{1 - e^{-\mu}} \,. \quad (42)$$

In the case of central dijet events passing `JT_65TT` trigger, about 27% of events contain at least one additional minimum bias interaction.

Equations 41 and 42 allow us to estimate the level of the dijet sample contamination caused by two overlapping independent events with central jets. The largest contamination is in the low mass region. The dijet mass spectrum is measured from mass of 115 GeV. Fig. 38 shows that p_T of the two leading jets in events passing the trigger `JT_25TT_NG` is above 40 GeV. The cross section σ_{40} for production of a central jet with $p_T > 40$ GeV can be roughly obtained from Fig. 21; the estimate is $\sigma_{40} \sim 8 \times 10^{-4}$ mb. According to Eq. 41, a mean number of interactions having a central jet with p_T above 40 GeV is $\mu_{40} \sim 8 \times 10^{-6}$. A probability that such an interaction is accompanied by another one with central jet with $p_T > 40$ GeV is then about 4×10^{-6}. Number of events that fired trigger `JT_25TT_NG` and that have a central jet with $p_T > 40$ GeV was $\sim 2 \times 10^5$, which gives an estimate

that there is roughly one event in the entire `JT_25TT_NG` sample for which the central two leading jets with $p_T > 40\,\mathrm{GeV}$ come from different $\mathrm{p\bar{p}}$ interactions. This is an upper limit on the contamination of dijet sample, since not all such events would have dijet mass above $115\,\mathrm{GeV}$. The conclusion is that the contamination of the dijet sample from the additional minimum bias interactions is negligible.

10 Jet and dijet mass resolutions

The measured dijet mass spectrum is affected by the finite detector resolution. It is essential to know the dijet mass resolution in order to correct the data for detector effects. Since no sharp resonance, that would provide the direct input for such determination, is present in the spectrum at high masses, the mass resolution has to be determined from the data indirectly. The dijet mass M_{JJ}, defined as an invariant mass of the dijet system, is calculated according to

$$M_{JJ}^2 = (P_{jet1} + P_{jet2})^2 = (E_{jet1} + E_{jet2})^2 - (\vec{p}_{jet1} + \vec{p}_{jet2})^2 \,, \qquad (43)$$

where $P_{jet} = (E_{jet}, \vec{p}_{jet})$ is the jet 4-momentum, E_{jet} the jet energy, and $\vec{p}_{jet}$ the jet momentum. In the limit of massless jets, the formula simplifies into

$$M_{JJ}^2 = 2E_T^{jet1} E_T^{jet2} \left[\cosh(\eta_{jet1} - \eta_{jet2}) - \cos(\phi_{jet1} - \phi_{jet2}) \right] \,, \qquad (44)$$

where E_T^{jet}, η_{jet}, and ϕ_{jet} are the jet transverse energy, pseudorapidity, and azimuthal angle respectively. We see that there are two sources of the dijet mass resolution; the smearing of the jet transverse energy and the smearing of jet direction. A dominant part coming from the jet transverse energy resolution can be obtained directly from the data looking at the transverse momentum imbalance in the dijet events. The description of the method together with the measurement is given in the next subsection 10.1. A determination of the angular jet resolutions in ϕ and η requires a full Monte Carlo simulation of the detector response. There are still significant discrepancies between the data and current MC simulations, especially in resolution (see subsection 10.1.6). However, as is discussed in subsection 10.2, the effect of the angular smearing on the mass resolution is negligible.

The final dijet mass resolution is determined by the propagation of the jet resolutions into the mass. This is done by smearing the properties of jets generated by particle level generators and by comparing the original dijet mass with the mass after the smearing. The details of the method and the results are given in subsection 10.3.

10.1 Jet transverse momentum resolution

Since only two jets (partons) are present in the final state at LO QCD calculations they should be balanced in transverse momentum due to momentum conservation. However, this relation does not hold exactly due to initial transverse momentum kick-off of the interacting partons. Also parton showering and subsequent hadronization spoil the p_T balance of the two leading jets. This p_T imbalance can be studied on particle level using MC generators. As is shown in subsection 10.1.4, it is much smaller than the p_T imbalance of jets measured in the calorimeter. Thus the p_T imbalance in the dijet events can be used to measure the jet transverse momentum resolution.

The method to determine the jet transverse momentum resolution used in this analysis is the same as the method used in Run I [63, 64]. The main advantage of the method is the complete independence on full MC simulation of the detector. It can be used to test an agreement between MC detector simulation and real data. As is discussed in subsection 10.1.6, there is a significant difference between resolutions in the current MC simulations and in data.

The first step is to measure the dijet transverse momentum asymmetry $\mathcal{A}$ which is defined as

$$\mathcal{A} = \frac{|p_T^{jet1} - p_T^{jet2}|}{p_T^{jet1} + p_T^{jet2}} \,. \tag{45}$$

Since the jet resolution depends on jet transverse momentum, the asymmetry distribution is measured in several bins of

$$p_T^{event} = \frac{p_T^{jet1} + p_T^{jet2}}{2} \,. \tag{46}$$

In the ideal case of p_T balanced jets, $p_T^{jet1} = p_T^{jet2} = p_T$, the width $\sigma_{\mathcal{A}}$ of the asymmetry variable distribution is directly connected to the jet p_T resolution σ_{p_T} by relation

$$\sigma_{\mathcal{A}}^2 = \left(\frac{\partial \mathcal{A}}{\partial p_T^{jet1}}\right)_{p_T}^2 \sigma_{p_T}^2 + \left(\frac{\partial \mathcal{A}}{\partial p_T^{jet2}}\right)_{p_T}^2 \sigma_{p_T}^2 \,, \tag{47}$$

which can be simplified to

$$\frac{\sigma_{p_T}}{p_T} = \sqrt{2}\,\sigma_{\mathcal{A}}\,. \tag{48}$$

This formula is used to calculate the raw uncorrected jet p_T resolution from the width of the asymmetry distribution $\sigma_{\mathcal{A}}$. The important feature of the compensated calorimeters is their Gaussian response to the jet. The DØ detector has such nearly compensated calorimeter. The asymmetry distribution is therefore expected to have Gaussian shape. The width $\sigma_{\mathcal{A}}$ of the asymmetry distribution can be obtained from a Gaussian fit with a mean value set to zero

$$G_0(\mathcal{A}) = \alpha \exp\left(-\frac{\mathcal{A}^2}{2\sigma_{\mathcal{A}}^2}\right)\,. \tag{49}$$

As was mentioned before, the leading two jets need not to be p_T balanced necessary. Although only two jets are explicitly required in the final state the balance can be spoiled by radiation of an additional soft jets below the 8 GeV cutoff used in the Run II cone jet algorithm. Raw jet resolution, measured according to Eq. 48, has to be corrected for this effect. The result is still biased by the fact that the jets on particle level are not p_T balanced even after the soft radiation correction. Since we are interested in the smearing of jet transverse momentum in the detector only the particle jet imbalance has to be subtracted.

At the end the final jet transverse momentum resolution is parametrised using the standard form

$$\frac{\sigma_{p_T}}{p_T} = \sqrt{\frac{N^2}{p_T^2} + \frac{S^2}{p_T} + C^2}\,, \tag{50}$$

where N/p_T, $S/\sqrt{p_T}$, and C correspond to the noise, sampling, and constant terms respectively.

10.1.1 Data sample and event selection criteria

The jet p_T resolution is measured on almost exactly the same data sample as the inclusive dijet mass cross section. Also the set of used jet triggers remains the same. There is a small difference in variable the defines the central dijet

sample. Resolution measurement is using the cut on jet pseudorapidity while the dijet mass spectrum analysis is using the cut on jet rapidity. Since this cut just defines the central calorimeter region and jet rapidity is almost the same as pseudorapidity it has almost no influence on the resulted resolutions. Because this is not a cross section measurement, no requirement is applied on the Luminosity Block the event belongs to.

The following cuts and event selection criteria were applied in order to select nice dijet events:

- only events with two cone $R = 0.7$ jets were considered
- kinematic cuts
  - both jets must be in the same region of calorimeter, $|\eta_{jet}| < 0.5$
  - selected two jets must be back-to-back, $\Delta\phi > 175°$
- event quality criteria
  - both jets have to pass the standard jet selection criteria
    - $0.05 < \mathrm{EMF} < 0.95$
    - $\mathrm{CHF} < 0.4$
    - $\mathrm{HotF} < 10$
    - $\mathrm{n90} > 1$
    - if $\mathrm{CHF} > 0.1$ then $\mathrm{f90} + 0.5\,\mathrm{CHF} < 0.8$
  - cut on missing E_T

    $$\not{E}_T < 0.7 p_T^{jet1} \quad \text{for} \quad p_T^{jet1} < 250\,\mathrm{GeV}$$
    $$\not{E}_T < 175\,\mathrm{GeV} \quad \text{for} \quad p_T^{jet1} > 250\,\mathrm{GeV}$$

    where p_T^{jet1} is the uncorrected transverse momentum of the leading jet
  - primary vertex has to have at least five associated tracks
  - z coordinate (along the beam axis) of the primary vertex is within 50 cm from the origin, $|z_{vtx}| < 50\,\mathrm{cm}$

For the purpose of determination of the soft radiation correction, an additional third jet is allowed to be present with a transverse momentum below some cut (10, 12, 15, and 20 GeV). This third jet must obey the jet selection criteria also.

Resulting jet resolutions depend on the event quality cuts. For example, the cut on missing E_T directly influences the overall p_T balance in the event. Jet p_T is also a function of the vertex z-position. Thus the vertex cuts have direct impact on the jet resolution. Moreover, there can be more than one primary vertex in the event due to multiple $p\bar{p}$ interactions in one bunch crossing. A misidentification of the primary vertex corresponding to the hard interaction leads to a wrong measurement of jet p_T. Therefore, it is important that the event quality criteria are exactly the same as in the case of the inclusive dijet mass spectrum analysis sample.

All jet energies were corrected using jet energy scale provided by `jetcorr` package, version `v04-01-00`, see [49].

10.1.2 Raw jet p_T resolution

In the first step, the jet p_T resolution σ_{p_T}/p_T was measured according to Eq. 48 for each considered jet trigger independently. The result is displayed on Fig. 40. The resolution in a given trigger coincides with the resolution for the trigger with the lower p_T threshold once the trigger is turned on. A behaviour of the asymmetry distribution is illustrated in Fig. 41 in the case of the `JT_45TT` trigger. While the distribution does not peak at zero in the p_T bin below the trigger turn-on (Fig. 41a) it shows a Gaussian shape above the turn-on point (Fig. 41b).

The following criteria were considered in order to determine which trigger should be used in a given p_T bin. Bin in transverse momentum must be above the p_T trigger turn-on point (Tab. 3). Also a good quality in terms of χ^2 per number of degrees of freedom (ndf.) is required for the Gaussian fit (Eq. 49). If more triggers satisfy the above criteria the one with higher statistics is chosen at the end. In any case, at least 54 entries in the asymmetry dis-

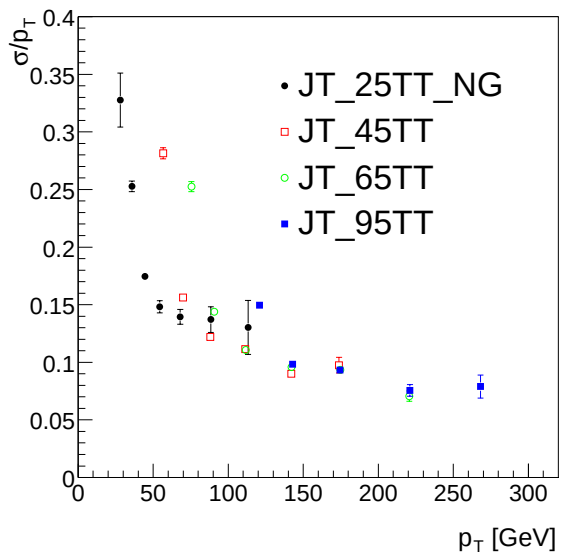

Figure 40: Uncorrected jet p_T resolution measured in different jet triggers for the cone $R = 0.7$ jets in the central region of the calorimeter, $|\eta_{jet}| < 0.5$.

tribution plot are required in order to consider the resolution measurement in a given p_T bin at all. Tab. 9 summarises the results for uncorrected jet p_T resolutions and also shows which particular trigger was used in a given p_T bin. The quoted errors are statistical only and they are coming from the error on the Gaussian fit.

10.1.3 Soft radiation correction

Although only dijet events were taken into account in the previous step, there might be still some soft activity in the event that can spoil the dijet p_T balance. Namely, the Run II cone algorithm introduces a strict 8 GeV cut on jet p_T and the softer jets are removed from the final list of jets.

In order to study the influence of the soft radiation, the raw jet resolution is measured also in events where the third jet below some p_T^{cut} is allowed to be present in the final state. The following values of p_T^{cut} were used: 10, 12, 15, and 20 GeV. The explicit dijet sample, considered in the first step,

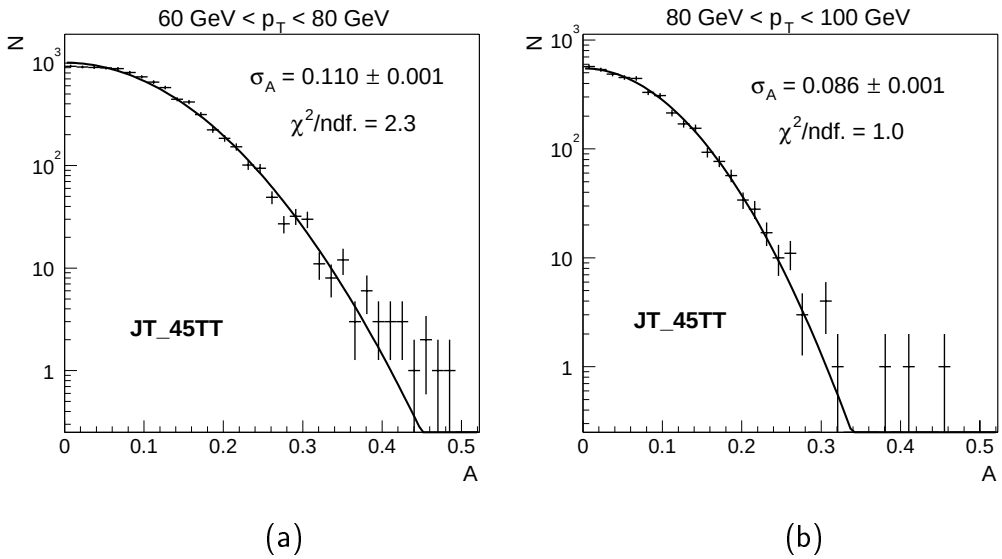

Figure 41: Asymmetry variable distribution for events passing the JT_45TT trigger in two p_T bins. One bin (a) is below and the other (b) above the trigger turn-on point.

p_T [GeV]	trigger	N_{evt}	$\langle p_T \rangle$	σ_{p_T}/p_T	χ^2/ndf
$50-60$	JT_25TT_NG	646	54.4 GeV	0.1483 ± 0.0053	1.2
$60-80$	JT_25TT_NG	417	68.0 GeV	0.1395 ± 0.0064	1.0
$80-100$	JT_45TT	4008	88.1 GeV	0.1221 ± 0.0015	1.0
$100-130$	JT_45TT	1778	111 GeV	0.1114 ± 0.0022	1.4
$130-160$	JT_65TT	1853	142 GeV	0.0958 ± 0.0018	1.3
$160-200$	JT_95TT	855	175 GeV	0.0932 ± 0.0023	0.9
$200-250$	JT_95TT	260	221 GeV	0.0756 ± 0.0051	1.2
$250-300$	JT_95TT	70	268 GeV	0.0789 ± 0.0100	1.2

Table 9: Uncorrected jet p_T resolutions for cone $R = 0.7$ in the central calorimeter region, $|\eta_{jet}| < 0.5$. The quoted errors are statistical only and they are coming from the error on the Gaussian fit.

correponds to $p_T^{cut} = 8\,\mathrm{GeV}$. The obtained jet resolution as a function of p_T^{cut} is displayed on Fig. 42 for several p_T bins. As expected, the dijet p_T balance gets worse with the increasing value of p_T^{cut}. Low p_T bins are also more sensitive to the change of this cut. The observed dependence on p_T^{cut} is consistent with the linear fit (solid lines in Fig. 42)

$$(\sigma_{p_T}/p_T) = a + b\, p_T^{cut}\,. \tag{51}$$

This fit is used to extrapolate the jet resolution to $p_T^{cut} = 0\,\mathrm{GeV}$ and its intersection with the y-axis (parameter a) can be interpreted as jet resolution corrected for soft radiation.

However, this approach is not applied directly. One reason is connected with a difficulty of an error calculation on parameter a. The error on jet resolution at one particular value of p_T^{cut} in Fig. 42 comes from the fit on the asymmetry distribution width $\sigma_{\mathcal{A}}$. Since the same data sample was used in all measurements of the jet p_T imbalance at different values of p_T^{cut}, the data points are strongly correlated. A correct determination of the error would require the knowledge of these correlations. Another reason is that the soft correction is rather poorly measured at large p_T. The correction itself is small and also the statistics drops down. Soft radiation correction is therefore rather applied as an multiplicative factor K_{soft} to the jet resolution measured in the pure dijet sample. Based on this definition, the correction factor is connected to the parameters of the linear fit (Eq. 51) by the relation

$$K_{soft} = \frac{(\sigma_{p_T}/p_T)|_{p_T^{cut}=0}}{(\sigma_{p_T}/p_T)|_{p_T^{cut}=8}} = \frac{a}{a+8b} = \frac{1}{1+\frac{8b}{a}}\,. \tag{52}$$

The factor is determined for each p_T bin according to this equation. Since the soft correction is measured poorly, the p_T dependence is smoothed using the fit of the functional form

$$K_{soft}(p_T) = 1 - \exp(-a_0 - a_1\, p_T). \tag{53}$$

This form reflects our expectations on p_T behaviour of the factor K_{soft}. It is a small correction vanishing at large momenta.

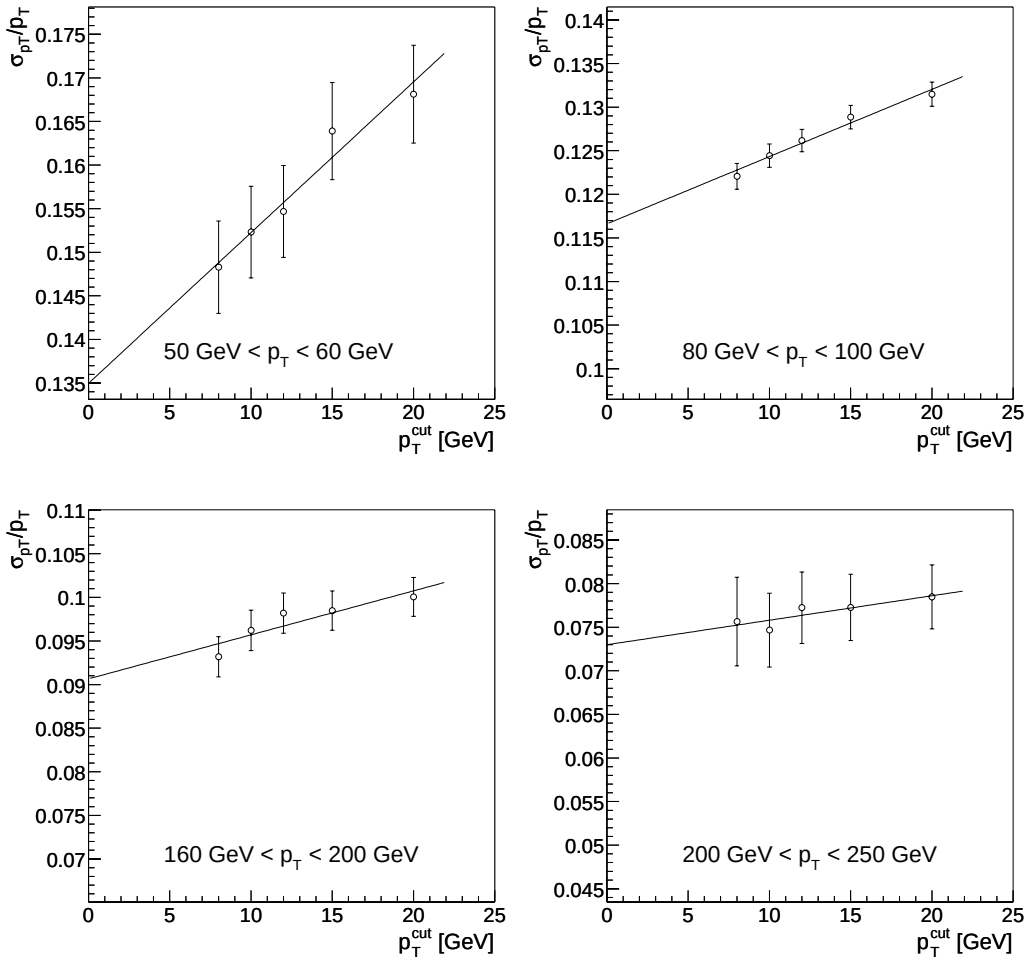

Figure 42: Jet p_T resolution as a function of a cut on p_T of the additional third jet. Solid line represents the linear fit.

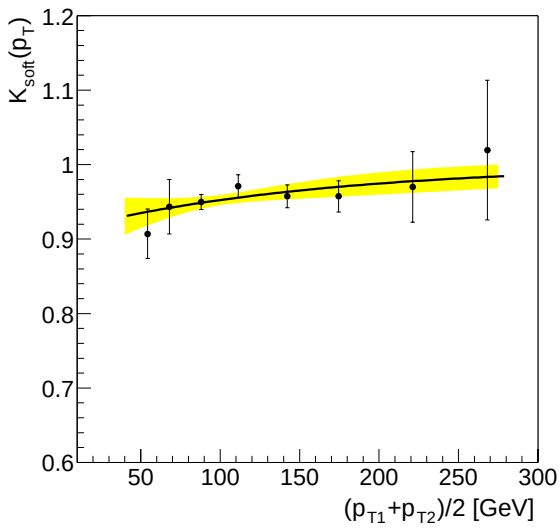

Figure 43: Soft radiation correction for cone $R = 0.7$ in the central calorimeter region, $|\eta_{jet}| < 0.5$. Solid line represents the fit of the function on the right side of Eq. 53. Shaded region is for the error of the fit.

Figure 43 shows the fit together with the measured points. The results on soft radiation correction are summarised in Tab. 10. The errors on the soft radiation correction K_{soft} in a given p_T bin were calculated from Eq. 52 using the covariance matrix of the linear fit. Quoted errors do not take into account correlations between the data points at various p_T^{cut}. Therefore they represent the upper error limits on K_{soft}. K_{soft}^{fit} corresponds to the result of the p_T dependence fit using functional form Eq. 53. Correlations between the a_0 and a_1 parameters are properly taken into to account in the evaluation of the error of the fit. Parameters of the fit are

$$a_0 = 2.42\,, \qquad a_1 = 0.00626\,\mathrm{GeV}^{-1}\,. \tag{54}$$

Finally, $\sigma_{p_T}^{corr.}/p_T$ is jet resolution corrected for the soft radiation. The error is calculated from the error on raw jet resolution and the fit error on $K_{soft}(p_T)$. It is more a conservative estimate rather than a true error. The last column (Err_{min}) represents the error on the corrected resolution if no error on K_{soft} is

p_T [GeV]	$\langle p_T \rangle$	K_{soft}	K_{soft}^{fit}	$\sigma_{p_T}^{corr.}/p_T$	Err_{min}
$50-60$	54.4 GeV	0.907±0.033	0.937±0.018	0.1389±0.0057	0.0050
$60-80$	68.0 GeV	0.943±0.036	0.942±0.013	0.1314±0.0063	0.0060
$80-100$	88.1 GeV	0.950±0.010	0.949±0.008	0.1158±0.0017	0.0014
$100-130$	111 GeV	0.971±0.015	0.956±0.008	0.1065±0.0022	0.0021
$130-160$	142 GeV	0.957±0.015	0.963±0.010	0.0923±0.0020	0.0017
$160-200$	175 GeV	0.957±0.021	0.970±0.013	0.0904±0.0026	0.0022
$200-250$	221 GeV	0.970±0.047	0.978±0.016	0.0740±0.0051	0.0050
$250-300$	268 GeV	1.019±0.094	0.983±0.016	0.0776±0.0100	0.0098

Table 10: Soft radiation correction K_{soft} from the linear fit for given p_T bins.

taken into account. It shows that the overall error is dominated by the error on raw resolution. Precise knowledge of the error on K_{soft} is not crucial. At the end, the conservative upper limit error on K_{soft} was used.

10.1.4 Particle jet imbalance

The method is based on the assumption that the particle jets entering the detector are p_T balanced. However, this is not true even in the explicit dijet events due to the initial transverse momentum kick-off of the interacting partons, parton showering, hadronization and the out-of-cone particle radiation. The measured resolution is a convolution of the detector resolution and p_T imbalance of jets on the particle level.

The particle jet imbalance was studied on a QCD sample generated by Pythia 6.202 [26, 27] with different cuts on transverse momentum of scattered partons in the hard matrix element[13]. In particular, samples with p_T cuts between 20 and 225 GeV were used. Particle jet imbalance is estimated from MC particle jets using exactly the same method as for the data, i.e. the raw

[13]Pythia cardfile comes from `cardfile` package in the DØ Run II release p13.05.00 from file `np/pythia_qcd_incl.cards`. The Run II cone algorithm with $R = 0.7$ was run on particle level by `jetanalyze` package.

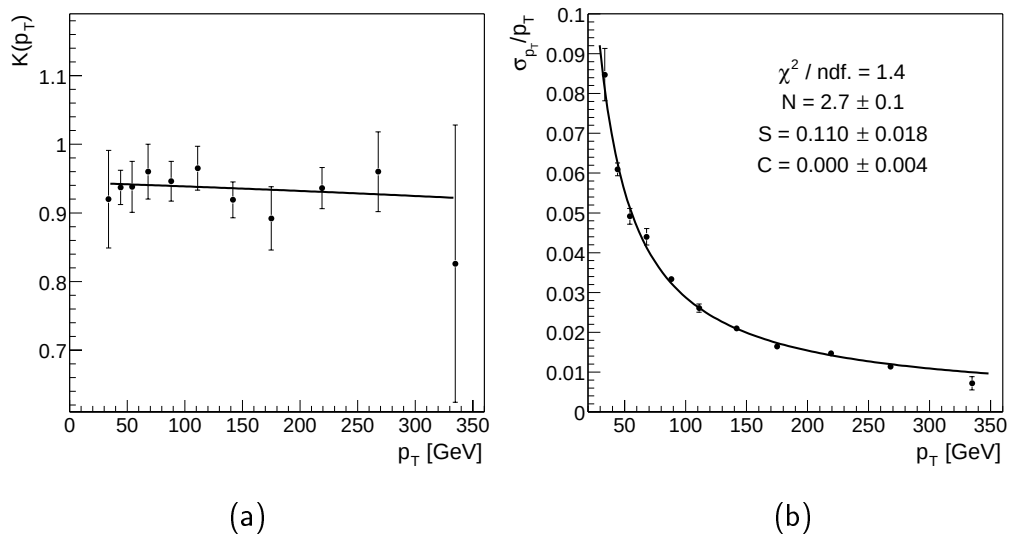

Figure 44: Soft radiation correction (a) and jet p_T imbalance (b) for cone jet $R = 0.7$ on particle level in the central calorimeter region.

jet resolution is determined from a sample of explicit dijet events in the first step and the result is corrected for soft radiation. Results for soft radiation correction and final particle jet imbalance are shown on Fig 44. The solid line in Fig 44b represents the fit using the functional form Eq. 50.

10.1.5 Jet resolution - final result

The particle jet imbalance has to be decoupled from the measured resolution in order to obtain pure detector resolution. Since the detector smearing is independent on the particle jet imbalance, the final jet resolution is calculated according to

$$\left(\frac{\sigma_{p_T}}{p_T}\right)^2 = \left(\frac{\sigma_{p_T}}{p_T}\right)^2_{corr} - \left(\frac{\sigma_{p_T}}{p_T}\right)^2_{MC}, \tag{55}$$

where $(\sigma_{p_T}/p_T)_{corr}$ is the jet resolution measured in data after soft radiation correction and $(\sigma_{p_T}/p_T)_{MC}$ is the jet particle imbalance. The result is displayed in Fig. 45 and summarised in Tab. 11 (systematic errors are discussed in the following). The fit and its error in Fig. 45 are extended to the low and

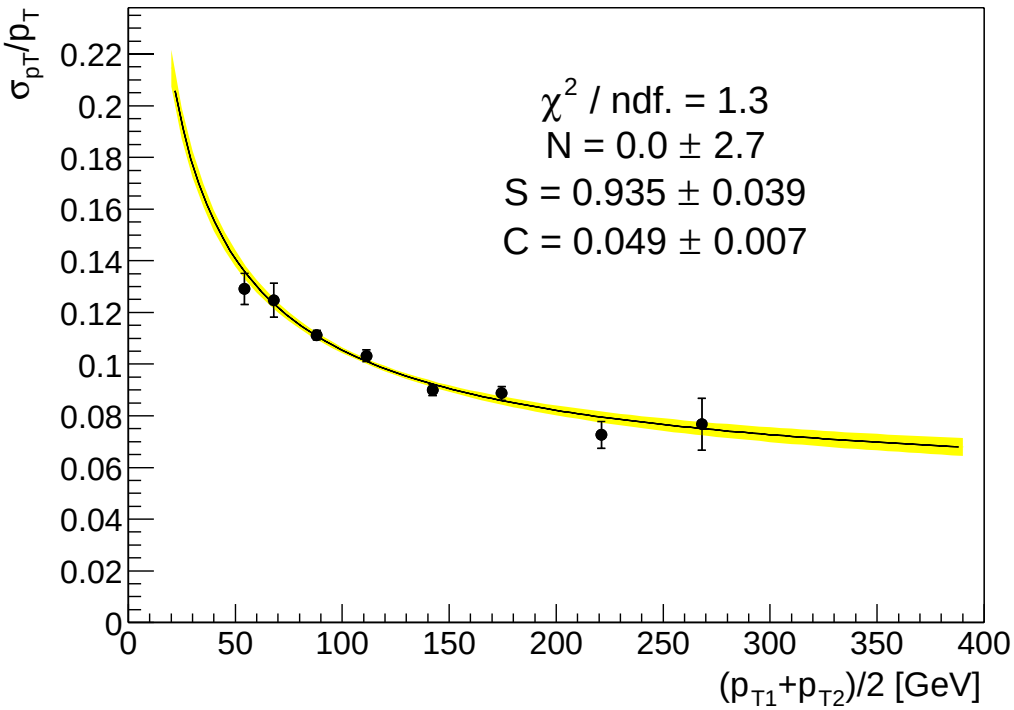

Figure 45: Corrected jet p_T resolution for the cone $R = 0.7$ in the central calorimeter region, $|\eta_{jet}| < 0.5$. Solid line represents the standard fit (Eq. 50), shaded region is the error on resolution coming from the fit.

p_T [GeV]	$\langle p_T \rangle$	σ_{p_T}/p_T	sys. error
$50-60$	54.4 GeV	0.1291±0.0061	0.0065
$60-80$	68.0 GeV	0.1248±0.0066	0.0062
$80-100$	88.1 GeV	0.1112±0.0018	0.0056
$100-130$	111 GeV	0.1032±0.0023	0.0052
$130-160$	142 GeV	0.0899±0.0021	0.0045
$160-200$	175 GeV	0.0887±0.0026	0.0044
$200-250$	221 GeV	0.0726±0.0052	0.0036
$250-300$	268 GeV	0.077±0.010	0.004

Table 11: Corrected jet p_T resolution for the cone $R = 0.7$ algorithm in the central calorimeter region, $|\eta_{jet}| < 0.5$.

$$N = 0.0 \pm 2.7\,\mathrm{GeV}$$
$$S = 0.935 \pm 0.039\,\mathrm{GeV}^{1/2}$$
$$C = 0.0487 \pm 0.0066$$

	N	S	C
N	1	-0.003	0.001
S	-0.003	1	-0.951
C	0.001	-0.951	1

Table 12: Results of the fit (Eq. 50) for the corrected jet energy resolution for the cone $R = 0.7$ in the central calorimeter region, $|\eta_{jet}| < 0.5$.

high p_T regions where no data point is present.

The measured p_T dependence of the resolution was parametrized using Eq. 50. The result of the fit on the parameters together with the correlation matrix is given in Tab. 12. Correlations between the fitted parameters where taken into account in the error calculation of the fit (shaded region in Fig. 45). The noise term has some influence only at the low p_T end. Since the lowest bin starts at 50 GeV, the data points do not constrain the noise term and the N parameter is not measured at all.

The only "free" parameter of the method is the cut on dijet distance in azimuthal angle $\Delta\phi > 175°$. The other event selection criteria are fixed by the event selection in the dijet mass analysis. For the purpose of the evaluation

of the systematic error, the whole analysis was redone with a slightly looser cut $\Delta\phi > 165°$. The difference between jet resolutions after soft radiation correction is small and hard to measure. On average, the jet resolution is consistently slightly higher in the case of $\Delta\phi > 165°$ cut. The shift is about 0.001 and it is treated as one part of an estimate of the systematic error.

10.1.6 Closure test

The method of the determination of the jet p_T resolution from the dijet p_T imbalance is tested on the full Monte Carlo (MC) simulation of the DØ detector. For this purpose, QCD samples generated with Pythia with several cuts on p_T in the hard matrix element at parton level were used. The detector response was simulated with the `p13.08.00` release of the DØ Run II software. In one case, the resolution was determined from MC calorimeter jets in exactly the same way as the jet p_T resolution in the data. It means that the soft radiation and particle jet imbalance corrections were performed. The resulted resolution is displayed in Fig. 46a (full circles) together with the fit using Eq. 50 (full line). Jet p_T resolution was also obtained directly by comparing the transverse momenta of matched particle and detector jets. The result is displayed in Fig. 46a as dashed line. The relative difference between these two resolutions is plotted in Fig. 46b. It is smaller than 5% except the high p_T end where it reaches the level of 8%. Based on these numbers, a 5% error is assigned to the jet p_T resolution as a systematic error connected with the method. It is added to the systematic error of the final jet p_T resolution (see Tab. 11).

The MC resolution is compared to the resolution obtained from the data in Fig. 47. The resolution in MC is much better than in the data. In fact the MC resolution is only slightly worse than the Run I resolution. It was expected because there is more uninstrumented material in front of the calorimeter in Run II, namely new magnet and tracking system. However, it is not know why the calorimeter performance is much worse than in MC simulations. This problem is still under study. The discrepancy between MC

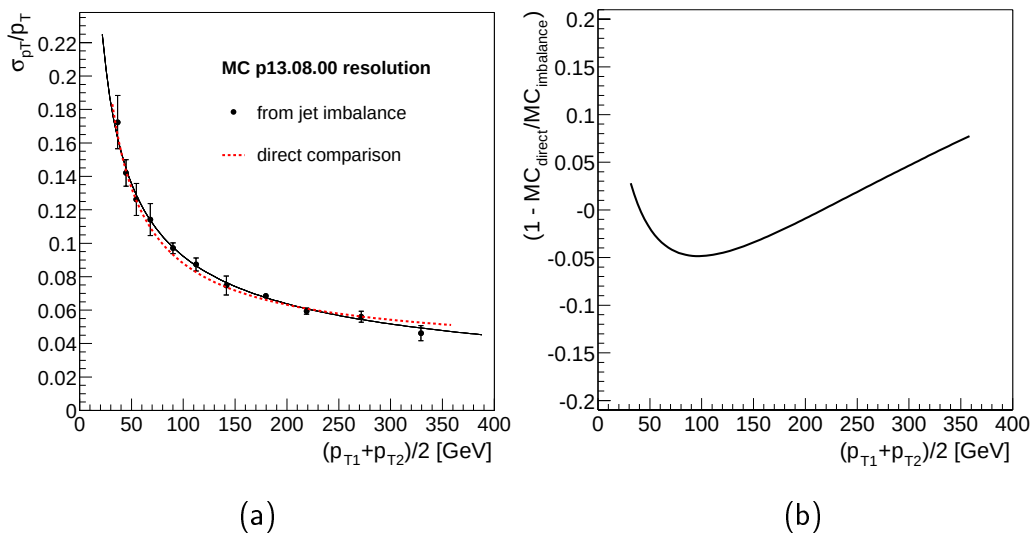

Figure 46: Jet p_T resolution in the central calorimeter region ($|\eta_{jet}| < 0.5$) determined from the full simulation of the DØ detector response. Full circles in the left plot represent the resolution derived from the particle jet imbalance, solid line then corresponds to the fit of Eq. 50. Dashed line represent jet resolution obtained from direct comparison of matched particle and detector jets. The right plot shows the relative difference between these two resolutions.

and real calorimeter performance is one of the reasons why MC was not used more extensively in this analysis.

10.2 Jet angular resolution

Full MC simulation of the detector response is required in order to determine jet angular resolutions. Jets on detector level are matched with particle jets using the following criterium: the closest particle jet within the distance $\Delta R = \sqrt{\Delta\phi^2 + \Delta\eta^2} < 0.2$ is assigned to a particular detector jet. Angular ϕ and η resolutions were obtained as a width of Gaussian fit on $\Delta\phi$ and $\Delta\eta$ distributions. The result is displayed on Fig. 48. The same MC QCD

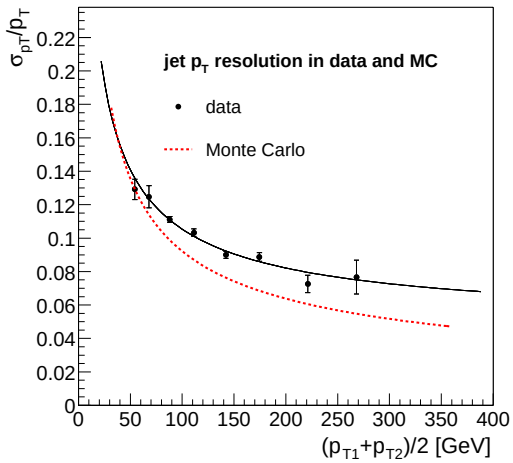

Figure 47: Comparison of jet p_T resolution measured from jet p_T imbalance in the data (full circles and solid line) and Monte Carlo (dashed line).

samples were used as in the case of closure test of the jet p_T resolution.

Obtained η and ϕ resolutions are similar. Also their p_T dependence is the same, it is about 0.03 at 40 GeV and it drops down to 0.01 at about 140 GeV. The contributions of the jet angular smearings σ_M^η and σ_M^ϕ to dijet mass resolution can be estimated from Eq. 44

$$\frac{\sigma_M^\eta}{M_{JJ}} = \frac{1}{2}\frac{|\sinh\Delta\eta|}{\cosh\Delta\eta - \cos\Delta\phi}\,\sigma_{\Delta\eta}\,, \tag{56}$$

$$\frac{\sigma_M^\phi}{M_{JJ}} = \frac{1}{2}\frac{|\sin\Delta\phi|}{\cosh\Delta\eta - \cos\Delta\phi}\,\sigma_{\Delta\phi}\,, \tag{57}$$

where $\Delta\eta = \eta_{jet1} - \eta_{jet2}$ and $\Delta\phi = \phi_{jet1} - \phi_{jet2}$. In the typical jet configuration, the jets are back-to-back $\Delta\phi \sim \pi$ and their difference in η is about $|\Delta\eta| \sim 0.5$. The denominator could be approximated by 2 in this case. The above relations are then simplified into

$$\frac{\sigma_M^\eta}{M_{JJ}} \sim \frac{|\Delta\eta|}{2\sqrt{2}}\,\sigma_\eta\,, \tag{58}$$

$$\frac{\sigma_M^\phi}{M_{JJ}} \sim \frac{\pi - \Delta\phi}{2\sqrt{2}}\,\sigma_\phi\,. \tag{59}$$

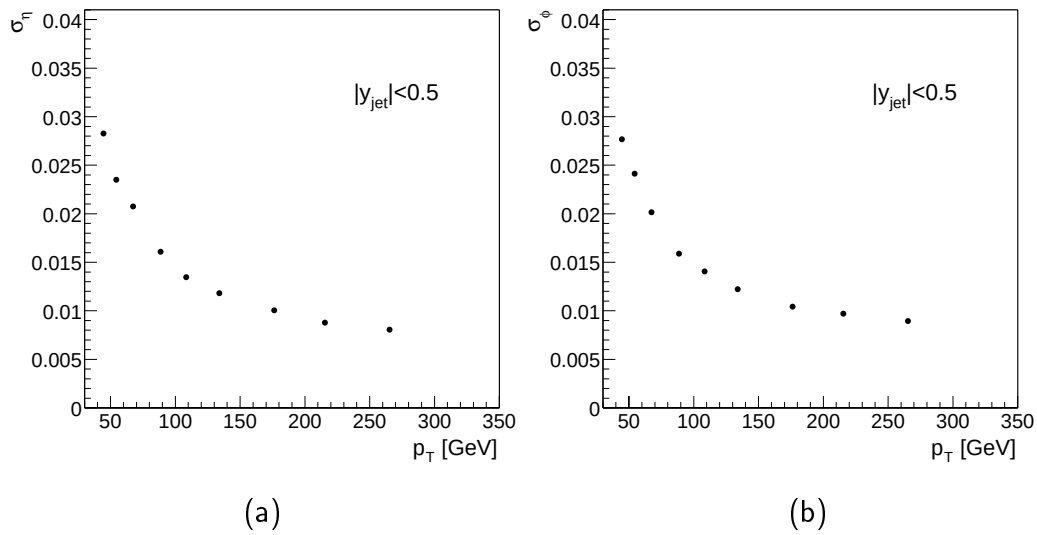

Figure 48: Jet angular resolution in the central calorimeter region as a function of jet transverse momentum. Left plot (a) corresponds to η resolution, right (b) to ϕ resolution.

Resolutions $\sigma_{\Delta\eta}$ and $\sigma_{\Delta\phi}$ were rewritten in terms of the angular resolutions: $\sigma_{\Delta\eta} = \sqrt{2}\sigma_\eta$ and $\sigma_{\Delta\phi} = \sqrt{2}\sigma_\phi$. An influence of the smearing in azimuthal angle is strongly suppressed due to back-to-back jet configuration. A contribution of smearing in pseudorapidity η estimated from Eq. 58 is $\sim 0.5\%$ for 40 GeV jets and $\sim 0.2\%$ for 120 GeV jets. According to Eq. 44, jet p_T smearing contributes to the dijet mass resolution as

$$\frac{\sigma_M^{p_T}}{M_{JJ}} = \frac{1}{\sqrt{2}} \frac{\sigma_{p_T}}{p_T}\,, \tag{60}$$

in the case when both jets have the same transverse momentum. It is about 11% for $p_T = 40\,\mathrm{GeV}$ ($\sim 80\,\mathrm{GeV}$ mass) and about 7% for 120 GeV jets. These numbers are much higher than in the case of the η resolution. This leads to the conclusion that the effect of angular smearing on the dijet mass resolution is negligible.

10.3 Dijet mass resolution

The dijet mass resolution is determined by the propagation of the jet resolutions into the mass distribution. Eq. 60 gives a hint how the mass resolution is connected to the p_T resolution. However, a correct determination requires the knowledge of the angular and the transverse momentum distributions of the two leading jets. The same MC QCD samples generated with Pythia were used for this purpose as in the case of particle jet imbalance studies.

In the first step, the particle jet momenta are smeared according to the measured jet p_T resolution. The angular smearing is not considered because the effect on dijet mass resolution is negligible as was shown in the previous section. The smeared dijet mass M'_{JJ} is then compared with the original unsmeared mass M_{JJ}. The width of Gaussian fit on $M'_{JJ}/M_{JJ}-1$ distribution corresponds to the relative dijet mass resolution. This is done in several bins of M_{JJ} which were chosen in such a way that the p_T distribution of the two leading jets was well above the p_T cut applied on parton level in MC generation. Fig. 49 shows an example of $M'_{JJ}/M_{JJ} - 1$ distribution at one particular mass bin ($460-520\,\mathrm{GeV}$). The shape of the distribution does not deviate from the Gaussian one. This may not be true and tails in the distribution may occur due to the change of jet p_T ordering caused by jet momentum smearing. Nevertheless, no such tails are observed.

In the second step, all dijet mass resolutions in particular mass bins are combined into one plot (Fig. 50a). The resolution dependence on dijet mass is then parametrised using the following form

$$\frac{\sigma_{M_{JJ}}}{M_{JJ}} = \sqrt{\frac{N^2}{M_{JJ}^2} + \frac{S^2}{M_{JJ}} + C^2}\,. \tag{61}$$

The result of the fit is

$$N = 0.8 \pm 3.6\,\mathrm{GeV}\,, \quad S = 0.954 \pm 0.031\,\mathrm{GeV}^{1/2}, \quad C = 0.036 \pm 0.001\,. \tag{62}$$

The dashed line in Fig. 50a corresponds to the estimation of dijet mass resolution based on Eq. 60, i.e. under the assumption that both jets have the

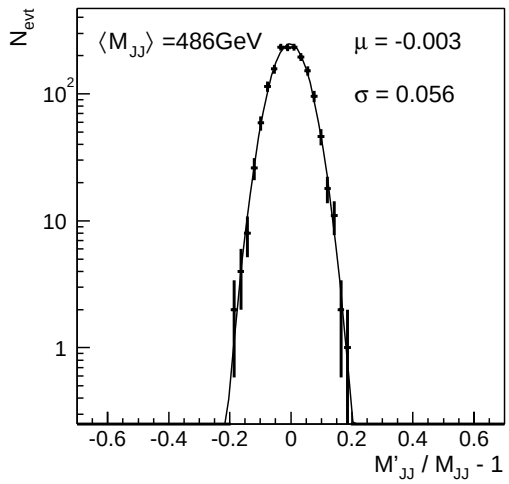

Figure 49: Distribution of the relative difference between smeared (M'_{JJ}) and unsmeared (M_{JJ}) dijet masses. Unsmeared mass is from the 460 – 520 GeV interval.

same transverse momentum and that $M_{JJ} \sim 2p_T$. It is slightly below the resolution obtained from MC but the difference is small. The correct description of jet p_T distribution (coming from MC simulation) does not therefore play a crucial role in the determination of dijet mass resolution. This is because the transverse momenta of the two leading jets are anti-correlated. The leading jet p_T is above $M_{JJ}/2$ the second jet is below usually. The leading jet has slightly better p_T resolution and the second leading slightly worse. These effects compensate in the calculation of mass resolution.

In order to obtain the error on dijet mass resolution, the jets were smeared according to the upper and lower error jet resolution curve. The result is represented by the shaded region in Fig. 50b. Data points are between 50 and 300 GeV in the jet p_T resolution plot. This means that the dijet mass resolution is measured in the region of 100 – 600 GeV. The resolution outside the region is an extrapolation based on Eq. 61.

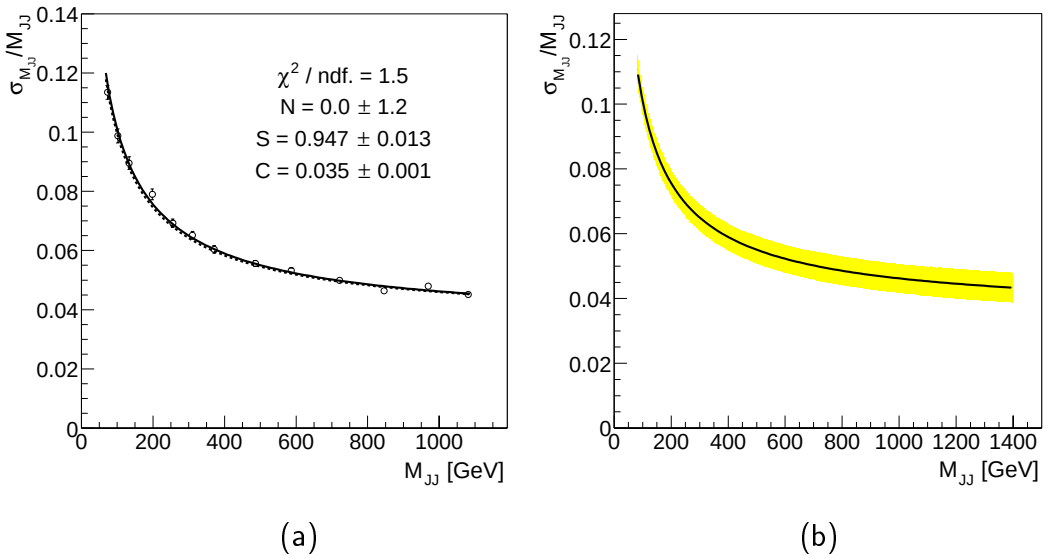

Figure 50: Dijet mass resolution in the central calorimeter region ($|\eta_{jet}| < 0.5$) for the cone $R = 0.7$ algorithm from smearing MC particle jets (a). Solid line corresponds to the fit Eq. 61. Dashed line is the dijet mass resolution estimation based on Eq. 60. The shaded region on the right plot shows the error on dijet mass resolution propagated from the error on jet p_T resolution.

11 Inclusive dijet mass cross section

Final results on dijet mass spectrum for central dijet events with $|y_{jet}| < 0.5$ are presented in this section. The definition of inclusive dijet mass cross section is given in the first part. The next step describes the determination of the dijet mass trigger turn-on points. The data are then corrected for the effects of detector resolution. Finally, the result is compared to the NLO QCD predictions based on two different sets of proton structure functions.

11.1 Master formula

The inclusive dijet mass cross section averaged over the mass bin is computed using the following formula

$$\left\langle \frac{\mathrm{d}\sigma}{\mathrm{d}M_{JJ}} \right\rangle_{bin} = \frac{N_{evt}}{\mathcal{L}} \frac{1}{\varepsilon_{eff}} C_{unsmear} \frac{1}{\Delta M_{JJ}} , \tag{63}$$

where N_{evt}, $\mathcal{L}$, ε_{eff}, $C_{unsmear}$, ΔM_{JJ} represent the number of events in the bin, the luminosity, the jet and event cut efficiencies, the unsmearing, and the dijet mass bin width respectively. Dijet mass M_{JJ} is calculated from the 4-momenta of the two leading jets according to Eq. 43. The events are required to fulfil the same event selection criteria that define the central dijet sample as is discussed in section 9.1. The overall jet and event cut efficiency ε_{eff} is calculated as a product of efficiencies of jet selection criteria ε_{jetID}, cut on vertex ε_{vtx}, and cut on missing transverse energy ε_{MET}

$$\varepsilon_{eff} = \varepsilon_{jetID}\, \varepsilon_{vtx}\, \varepsilon_{MET} \,. \tag{64}$$

These particular efficiencies were discussed in section 9.

11.2 Raw dijet mass spectrum – trigger turn-on points

Regions of dijet mass where the jet triggers are almost 100% efficient are determined in the same way as p_T turn-on points in section 7.1. Raw uncorrected inclusive dijet mass spectra are displayed in Fig. 51. Only jet energy

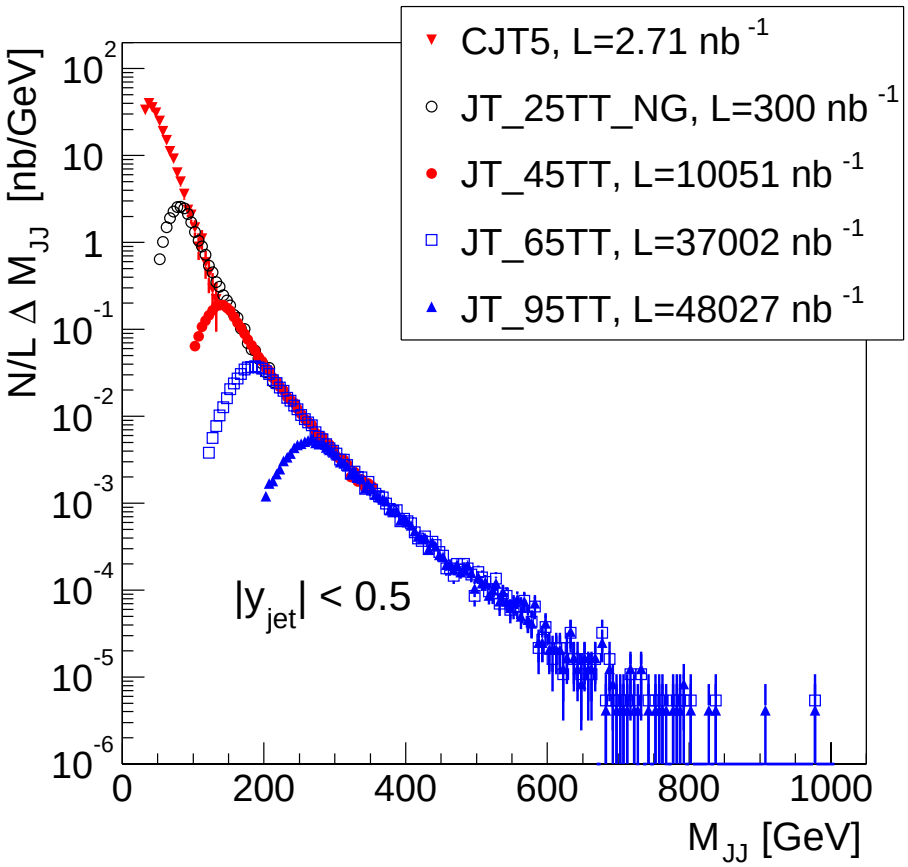

Figure 51: Uncorrected inclusive dijet mass spectra in the central region of calorimeter for jet triggers.

Trigger	95% turn-on point	99% turn-on point	M_{JJ} range [GeV]
JT_25TT_NG	103 GeV	112 GeV	$115-180$
JT_45TT	166 GeV	183 GeV	$180-250$
JT_65TT	217 GeV	250 GeV	$250-330$
JT_95TT	297 GeV	314 GeV	$330-1400$

Table 13: The 95% and 99% dijet mass turn-on points for jet triggers in the central region of calorimeter ($|y_{jet}| < 0.5$).

scale correction was applied for this purpose. Once the trigger becomes efficient the dijet mass spectrum starts to match the spectrum from the next jet trigger with the lower p_T threshold.

As in the case of p_T turn-on points, the more precise determination of dijet mass turn-on points is made from the ratio of spectra in the two subsequent triggers (Fig. 52). Founded positions of the 95% and 99% turn-on points are summarised in Tab. 13. The table also shows the mass ranges in which the triggers were used to calculate the dijet mass cross section. The lower interval limits are set by the 99% turn-on points. No correction for trigger efficiency is therefore made in the cross section calculation. Systematic error of 1% is assigned to the final cross section due to the trigger inefficiency.

11.3 Calorimeter east-west asymmetry

In order to reveal possible discrepancies in the data, north-south and east-west calorimeter symmetry is checked on the dijet mass spectrum. The number of events N_{+-} in particular dijet mass bin with the leading jet in the south part and the second leading jet in the north part should be the same as the number of events N_{-+} with the leading jet in the north part and the second leading jet in the south part of calorimeter. As is illustrated in Fig. 53a, no asymmetry between the north and south parts of calorimeter is observed in the data. However, if the leading jet in the south part is also

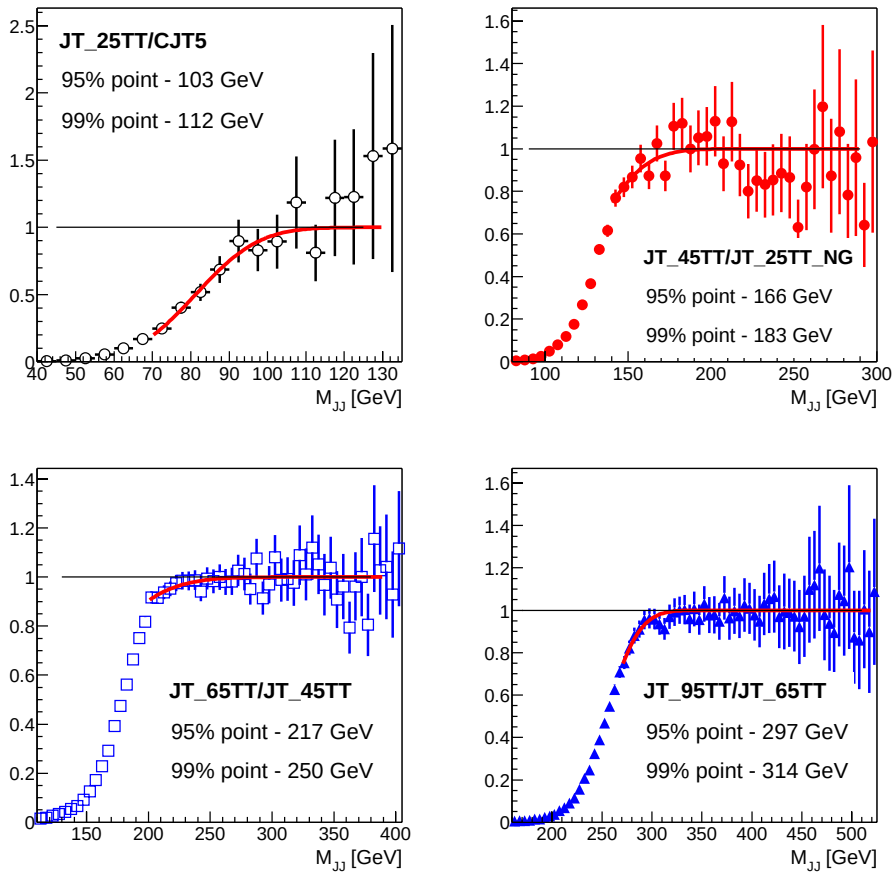

Figure 52: Ratio of inclusive dijet mass spectra in the two subsequent jet triggers for events from the central ($|y_{jet}| < 0.5$) dijet sample. Solid lines represent the fit from Eq. 32.

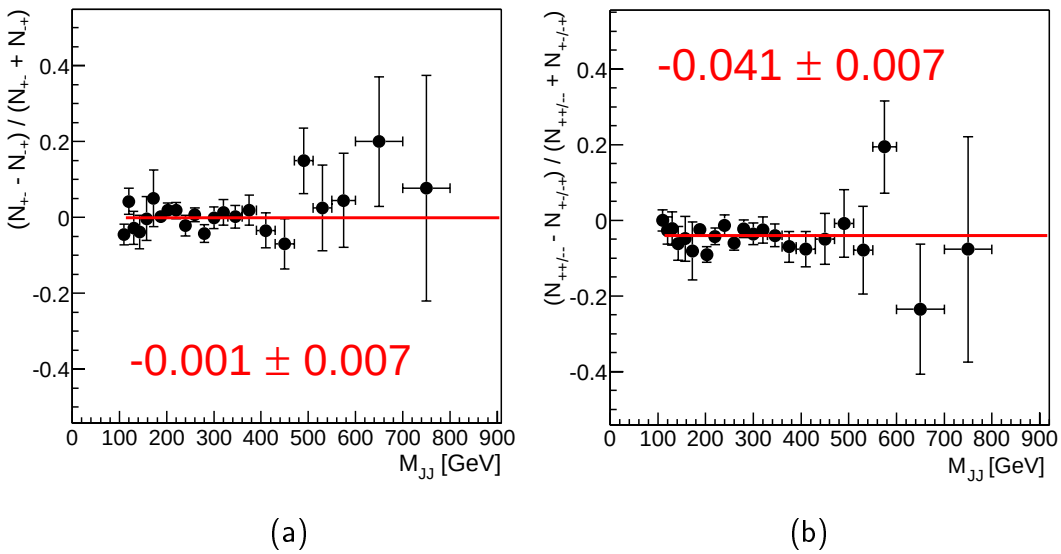

Figure 53: North-south (a) and east-west (b) asymmetry in the central dijet mass spectrum.

required to be in the east part of calorimeter ($p_x > 0$) and the second leading jet in the northwest part then the number of events $N_{++|--}$ is smaller than in the case when the leading jet is in the southwest part and the second leading jet in the northeast part ($N_{+-|-+}$). The observed 4% asymmetry (Fig. 53b) points out that the calorimeter response is not isotropic in azimuthal angle ϕ or that some hot or warm calorimeter zone appeared during the data taking.

11.4 Unsmearing method

Measured dijet mass cross section is smeared due to finite detector resolution. In order to obtained the original distribution at particle level, the effect of the resolution must be unfolded from the data. Such a procedure is called *unsmearing* or *unfolding*.

This analysis is using the same technique as was applied in the Run I dijet mass cross section measurement [64]. The method is based on a priory knowledge of the functional form of the unsmeared dijet mass spectrum.

This *ansatz* function is meant to describe the original dijet mass spectrum at particle level. As we will see in the following, the form

$$f\left(M_{JJ}|N,\alpha,\beta\right) = N M_{JJ}^{-\alpha}\left(1-\frac{M_{JJ}}{\sqrt{s}}\right)^{\beta}, \tag{65}$$

gives a good description of the data, where N, α, and β are parameters of the function and $\sqrt{s} = 1.96\,\mathrm{TeV}$ is the center of mass energy of the proton anti-proton collision. The unsmearing proceeds in the following steps.

1. The ansatz function (Eq. 65) is smeared according to dijet mass resolution for a given set of parameters

$$F(M_{JJ}) = \int_0^{\sqrt{s}} \mathrm{d}M'_{JJ}\, f(M'_{JJ})\, G(M'_{JJ} - M_{JJ}, M'_{JJ})\,. \tag{66}$$

   The Gaussian form of the dijet mass resolution is assumed

$$G(M'_{JJ} - M_{JJ}, M'_{JJ}) = \frac{1}{\sqrt{2\pi}\,\sigma_{M'_{JJ}}} \exp\left[-\frac{\left(M'_{JJ} - M_{JJ}\right)^2}{2\sigma^2_{M'_{JJ}}}\right], \tag{67}$$

   where $\sigma_{M'_{JJ}}$ is the dijet mass resolution at dijet mass M'_{JJ} calculated from Eq. 61.

2. A prediction is made on dijet mass cross section for each mass bin according to

$$\left\langle \frac{\mathrm{d}\sigma}{\mathrm{d}M_{JJ}} \right\rangle_{bin}^{pred} = \frac{1}{\Delta M_{JJ}} \int_{bin} \mathrm{d}M_{JJ}\, F\left(M_{JJ}\right), \tag{68}$$

   where ΔM_{JJ} is the bin width.

3. The χ^2 of the resulting smeared distribution with respect to the one measured in data is computed according to

$$\chi^2(N,\alpha,\beta) = \sum_{bin} \chi^2_{bin} = \sum_{bin} \left[\frac{\left\langle \frac{\mathrm{d}\sigma}{\mathrm{d}M_{JJ}} \right\rangle_{bin}^{pred} - \left\langle \frac{\mathrm{d}\sigma}{\mathrm{d}M_{JJ}} \right\rangle_{bin}^{raw}}{\Delta \left\langle \frac{\mathrm{d}\sigma}{\mathrm{d}M_{JJ}} \right\rangle_{bin}^{raw}}\right]^2. \tag{69}$$

   Raw cross section $\langle \mathrm{d}\sigma/\mathrm{d}M_{JJ}\rangle_{bin}^{raw}$ is calculated from Eq. 63 but the unsmearing correction is set to one (i.e. all corrections are applied except the unsmearing one). $\Delta\langle \mathrm{d}\sigma/\mathrm{d}M_{JJ}\rangle_{bin}^{raw}$ in Eq. 69 represents statistical error on the cross section.

4. Parameters N, α, and β are fitted to minimise χ^2 in Eq. 69.

5. The unsmearing correction is then obtained per bin as a ratio of unsmeared cross section calculated from the ansatz function to the smeared cross section (Eq. 68)

$$C^{bin}_{unsmear} = \frac{\int_{bin} \mathrm{d}M_{JJ}\, f(M_{JJ})}{\int_{bin} \mathrm{d}M_{JJ}\, F(M_{JJ})}\,. \tag{70}$$

The main advantage of the method is the independence on Monte Carlo simulation of the detector. However this approach has a few disadvantages. It depends on the factorisation hypothesis, namely that smearing effects are independent on the selection cuts. Or in other words, that the smearing effects are also the same for jets rejected by jet and event selection cuts. Ideally, this hypothesis should be tested using Monte Carlo and the difference between unsmearing factors treated as systematics. Since the the same jet and event selection criteria were used in the dijet mass resolution analysis, the potential bias is minimised. Moreover, this effect is negligible compared to the systematics due to energy scale corrections.

The unsmearing correction is made bin by bin. Therefore the final selection of mass bins must be finalised before the unsmearing procedure. A natural bin size is driven by the mass resolution. This rule was roughly followed in the low mass region where the statistics is large. However, the highest mass bins had to be made larger in order to keep reasonable amount of events in them. The other restriction is given by the requirement that bins cannot cross the boundaries between the trigger intervals as specified in Tab. 13. Finally, one more low mass bin ($105 - 115\,\mathrm{GeV}$) below the `JT_25TT_NG` turn-on point is kept for the purpose of unsmearing. It helps to constrain the low mass behaviour of the ansatz function. This bin is not reported in the final result.

Fig. 54 demonstrates the quality of the fit using the ansatz function (Eq. 65). The relative difference between data and prediction given by Eq. 68 is plotted there. The error bars correspond to statistical errors only. The

reduced χ^2 of the fit is close to one. It indicates that the input distribution describes the measurement reasonably well. The values of the fit parameters are

$$N = 4.698 \,.\, 10^9 \,, \quad \alpha = 4.602 \,, \quad \text{and} \quad \beta = 8.340 \,. \tag{71}$$

The unsmearing corrections together with the errors are given in Fig. 55. The correction factors vary between 83% and 95%. The biggest smearing effect is due to the smearing from low masses to higher masses because of the steep decrease of the dijet mass cross section with increasing mass. Consequently, all correction factors are less than 1.

One part of the systematic error on unsmearing comes from the choice of the ansatz function. To estimate this systematics the unsmearing was performed using another input function

$$f(M) = N M^{-\alpha} \exp\left[-\beta\left(\frac{M}{100}\right) - \gamma\left(\frac{M}{100}\right)^2\right] \tag{72}$$

The corresponding unsmearing correction is represented by the dashed line in Fig. 55a. The difference between the unsmearing factors from the two ansatz functions is smaller than 1%. This difference is treated as a contribution to the systematic error of the unsmearing procedure.

The most important contribution to the error on unsmearing comes from the error on the dijet mass resolution. Fig. 55b displays the unsmearing correction obtained using the upper (dashed line) and lower (dotted line) limits on the dijet mass resolution as was shown in Fig. 50b. The error is at the level of $1 - 2\%$.

The actual values of unsmearing factors together with the systematic errors are summarised in Tab. 14. Knowledge of the ansatz function allows also to compute for a given bin such a value of the dijet mass for which the cross section is the same as the average over the bin defined by the master equation. The position of this point is called *bin center*. It is also listed in Tab. 14.

mass bin [GeV]	bin center [GeV]	$C_{unsmear}$	systematic error
$115-125$	119.8	0.919	0.012
$125-135$	129.8	0.923	0.011
$135-150$	142.1	0.927	0.011
$150-165$	157.1	0.931	0.011
$165-180$	172.2	0.934	0.011
$180-195$	187.2	0.937	0.010
$195-210$	202.2	0.939	0.010
$210-230$	219.5	0.941	0.010
$230-250$	239.5	0.943	0.010
$250-270$	259.6	0.944	0.011
$270-290$	279.6	0.945	0.011
$290-310$	299.6	0.946	0.011
$310-330$	319.6	0.947	0.011
$330-360$	344.2	0.947	0.011
$360-390$	374.3	0.947	0.012
$390-430$	408.8	0.946	0.012
$430-470$	448.9	0.945	0.013
$470-510$	488.9	0.944	0.014
$510-550$	529.0	0.942	0.015
$550-600$	573.5	0.939	0.020
$600-700$	644.3	0.934	0.019
$700-800$	744.6	0.897	0.013
$800-1400$	958.4	0.827	0.008

Table 14: Unsmearing corrections and bin center positions.

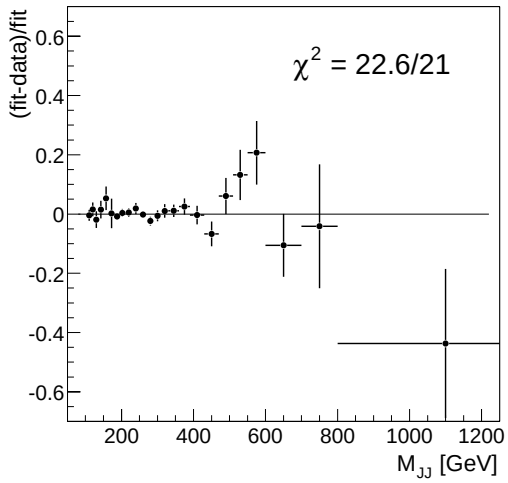

Figure 54: Relative difference between the data and prediction coming from the smeared ansatz function (Eq. 65).

11.5 Results

The inclusive dijet mass cross section in the central region of calorimeter ($|y_{jet}| < 0.5$) was calculated according to Eq. 63. The final spectrum was put toghether from the cross section measurements in four jet triggers with different p_T thresholds in the mass intervals as listed in Tab. 13. The cross section is given in Tab. 15 and plotted in Fig. 56. The data are represented by solid horizontal lines that correspond to the bin averaged cross sections determined from the master formula. The error bar on the data points is the total error calculated as statistical and systematic errors added in quadrature. A fully correlated $\sim 10\%$ error on luminosity measurement is not shown. Small perpendicular lines represent the statistical errors only. The error bars are positioned in the bin centers.

Dominant source of systematic uncertainty comes from the error on jet energy scale. For the purpose of the determination of this error, the whole analysis was repeated twice with the jet energy scale increased and lowered by the magnitude of the energy scale error. Relative difference of the dijet

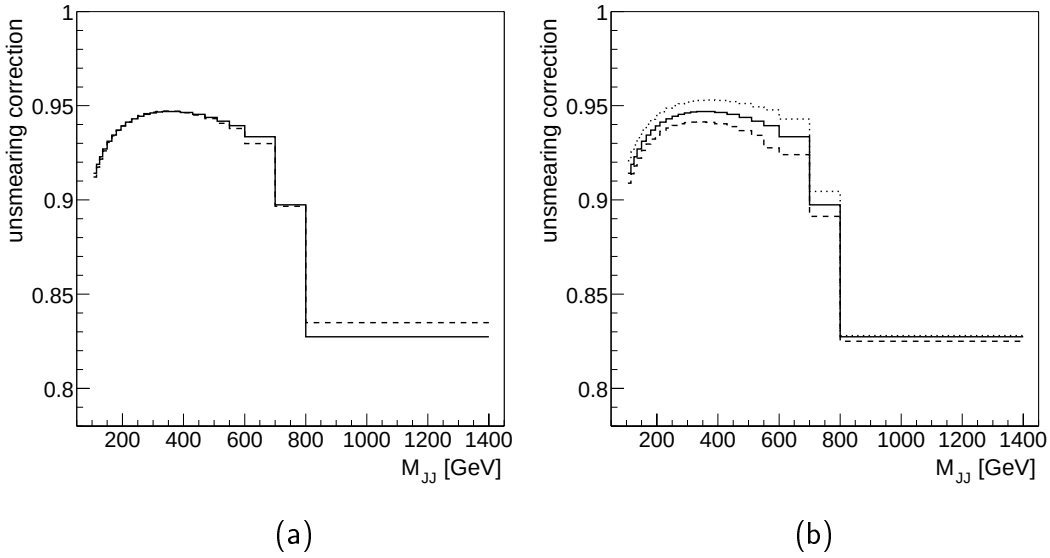

Figure 55: Uncertainties of the unsmearing correction. Solid line in the left plot (a) corresponds to the ansatz function in Eq. 65, dashed line to the ansatz function in Eq. 72. The right plot (b) shows the error on unsmearing corrections due to error on dijet mass resolution. Solid line corresponds to the measured mass resolution, dashed and dotted lines correspond to the unsmearing corrections using upper and lower errors on mass resolution.

mass bin [GeV]	bin center [GeV]	number of events	$< d\sigma/dM_{JJ} >$ $\pm$ stat. error [nb.GeV^{-1}]	sys. error Low [%]	High [%]
115 – 125	119.8	1894	$(7.66 \pm 0.18) \times 10^{-1}$	36	48
125 – 135	129.8	1204	$(4.89 \pm 0.14) \times 10^{-1}$	36	48
135 – 150	142.1	1160	$(3.15 \pm 0.09) \times 10^{-1}$	36	49
150 – 165	157.1	704	$(1.92 \pm 0.07) \times 10^{-1}$	37	49
165 – 180	172.2	409	$(1.12 \pm 0.06) \times 10^{-1}$	37	50
180 – 195	187.2	8587	$(7.02 \pm 0.08) \times 10^{-2}$	37	51
195 – 210	202.2	5667	$(4.64 \pm 0.06) \times 10^{-2}$	38	52
210 – 230	219.5	4770	$(2.94 \pm 0.04) \times 10^{-2}$	38	53
230 – 250	239.5	2934	$(1.81 \pm 0.03) \times 10^{-2}$	39	54
250 – 270	259.6	6663	$(1.11 \pm 0.01) \times 10^{-2}$	40	56
270 – 290	279.6	4201	$(6.98 \pm 0.11) \times 10^{-3}$	40	57
290 – 310	299.6	2820	$(4.68 \pm 0.09) \times 10^{-3}$	41	59
310 – 330	319.6	1927	$(3.19 \pm 0.07) \times 10^{-3}$	42	61
330 – 360	344.2	2352	$(2.00 \pm 0.04) \times 10^{-3}$	43	63
360 – 390	374.3	1390	$(1.18 \pm 0.03) \times 10^{-3}$	45	66
390 – 430	408.8	1000	$(6.37 \pm 0.20) \times 10^{-4}$	47	70
430 – 470	448.9	490	$(3.12 \pm 0.14) \times 10^{-4}$	49	74
470 – 510	488.9	301	$(1.91 \pm 0.11) \times 10^{-4}$	51	79
510 – 550	529.0	178	$(1.13 \pm 0.08) \times 10^{-4}$	53	85
550 – 600	573.5	126	$(6.37 \pm 0.57) \times 10^{-5}$	55	91
600 – 700	644.3	71	$(1.78 \pm 0.21) \times 10^{-5}$	59	102
700 – 800	744.6	21	$(5.07 \pm 1.11) \times 10^{-6}$	64	120
800 – 1400	958.4	5	$(1.85 \pm 0.83) \times 10^{-7}$	71	154

Table 15: Inclusive dijet mass cross section for cone jets of radius $R = 0.7$ for $|y_{jet}| < 0.5$. Systematic error is quadrature sum over all particular sources except the 10% error on luminosity.

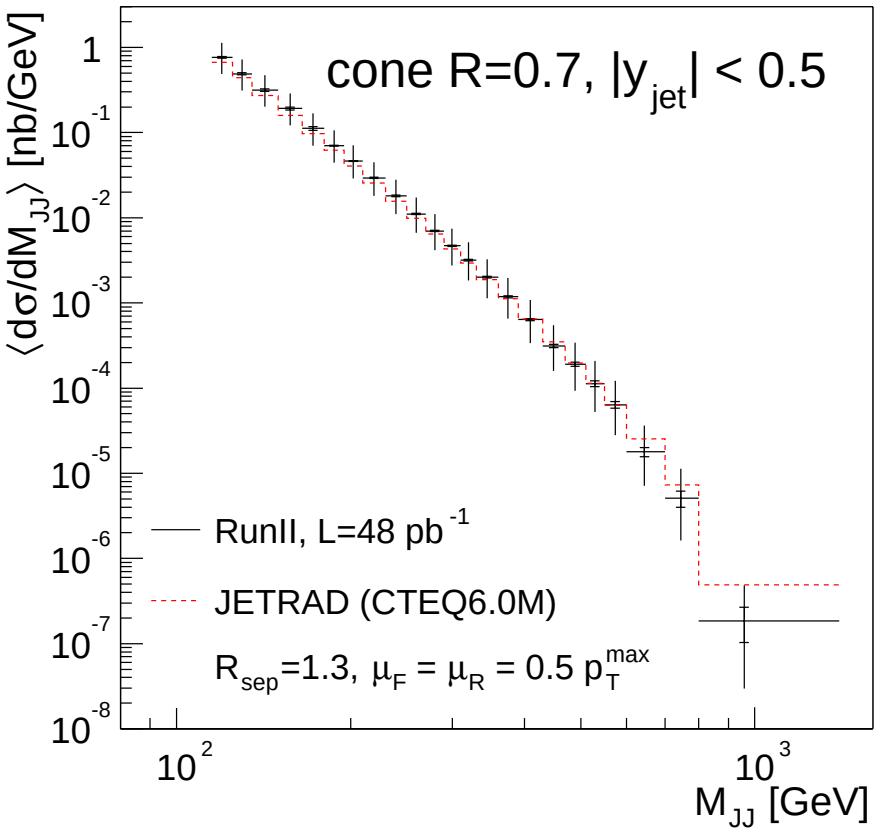

Figure 56: Inclusive dijet mass cross section for cone jets of radius $R = 0.7$ for $|y_{jet}| < 0.5$. The error bars represent the total error (except the fully correlated error on luminosity), small perpendicular lines correspond to statistical errors only. NLO QCD prediction calculated with JETRAD v2.0 with newly implemented E-scheme recombination is plotted as a dashed line.

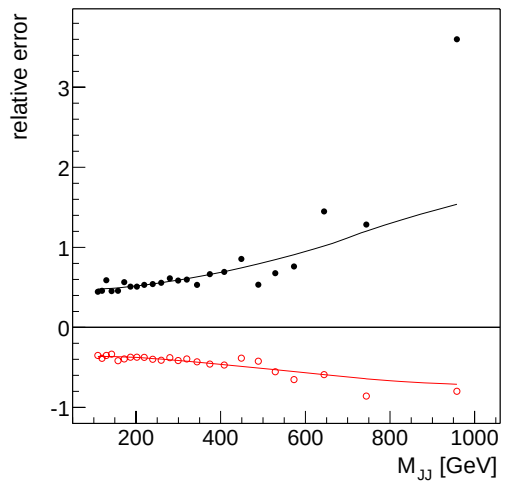

Figure 57: Relative difference of the dijet mass spectra in the case when the upper error (full circles) and the lower error (open circles) values of JES were used to the dijet mass spectrum obtained for the nominal JES. Solid lines correspond to the relative difference between the ansatz functions.

mass spectra is plotted in Fig. 57. In the end, the error on dijet mass cross section was obtained from the difference between the fitted ansatz functions. This approach was chosen because it produces smoothly behaving errors and eliminates large fluctuations in high mass bins due to small statistics. In the low mass region, the method reproduces the numbers obtained from the direct comparisson of the mass spectra. Since the dijet mass spectrum is steeply falling function, the 9% error on JES induces about 45% error on the cross section for $M_{JJ} \lesssim 400$ GeV. Jet energy scale is measured up to energy of 200 GeV which roughly corresponds to dijet mass of $M_{JJ} \sim 400$ GeV. The correction at high energies is given by the extrapolation which means that the error on JES is also increasing in this region (Fig. 16b). The error on the cross section therefore starts to increase rapidly at masses above 400 GeV.

The other sources of the error are plotted in Fig. 58. They do no exceed the 3% level. They are therefore negligible compared to the error from the jet energy scale and the error on luminosity. The errors from jet and events

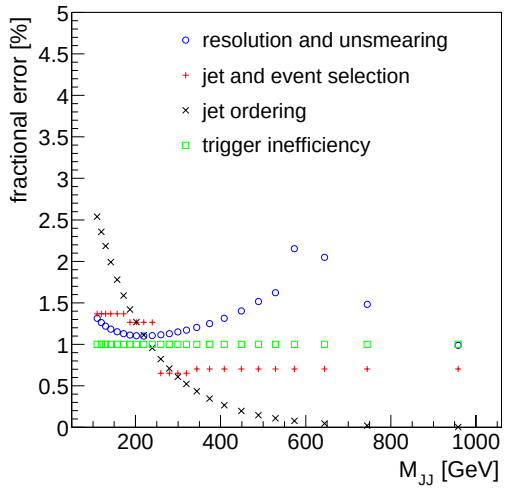

Figure 58: Other sources of systematic error on the dijet mass spectrum.

selection and from jet resolution and unsmearing procedure were already discussed. Another contribution comes from the jet ordering. Although the analysis is restricted to the central calorimeter region only, it is still sensitive to the calorimeter response outside this region. The sensitivity is introduced by the requirement that the two leading jets have $|y_{jet}| < 0.5$. However, the two leading jets can be misidentified if the jet energy scale outside the region is systematically shifted with respect to the scale in the central region. To evaluate this effect, the errors on JES were applied only during the jet ordering but not in the dijet mass calculation. The worst case scenario was considered. Namely, the central jets with $|\eta_{det}| < 0.6$ were corrected using normal value of JES while the $\pm 1\sigma$ values on JES were applied for jets with $|\eta_{det}| > 0.6$. The error was then calculated from the difference in the dijet mass spectra between the cases when the energy scale was increased/decreased by the JES error. It was found that the effect on jet ordering affected significantly only the low mass region. The error on the cross is negligible at masses higher above 400 GeV.

Compared to the former DØ Run I results [64], the lower range of dijet mass was extended from 150 GeV down to 115 GeV in this new Run II mea-

surement. Due to increased beam energy, the Run II sample is statistically comparable with the Run I sample. However, the results presented in this analysis do not reach the Run I precision yet. The main reason is rather poor knowledge of jet energy scale in this early stage of Run II. The error is about 13% for jets with energy of 400 GeV while the final Run I energy scale error was only about 2.3% [64]. Better understanding of jet energy scale is essential for further improvement of quality of Run II data.

11.6 NLO calculation of the dijet mass cross section

NLO QCD theoretical predicition is represented by the dashed line in Fig. 56. It was calculated with JETRAD v2.0 with a newly implemented E-scheme recombination that corresponds to the Run II cone jet algorithm scheme. CTEQ6.0M structure function was used as an input for this particular calculation. The factorization and renormalization scales were set to $\mu_F = \mu_R = 0.5 p_T^{max}$. Phenomenological parameter R_{sep} that models splitting and merging procedure on NLO parton level was set to 1.3.

The inclusive dijet mass cross section was calculated in the range between 90 and 1600 GeV in bins of 10 GeV size. This cross section was then fitted using functional form of

$$\alpha M_{JJ}^{-\beta} \left(1 - \frac{M_{JJ}}{\sqrt{s}}\right)^{\gamma} \left[1 + a_1 \frac{M_{JJ}}{\sqrt{s}} + \ldots + a_4 \left(\frac{M_{JJ}}{\sqrt{s}}\right)^4\right] . \qquad (73)$$

Ratio between the cross section calculated directly from JETRAD and the fit is shown in Fig. 59. The precision of the cross section calculation is already smaller than 1% in all mass bins. The fit further reduces the statistical fluctuations and the final precision is much better (roughly $\sim 0.3\%$).

As was discussed in section 4.2 on jet algorithms, there is an uncertainty connected with the modelling of splitting and merging mechanism at NLO (three jet) level. In order to estimate how the theoretical prediction is affected by the change in the R_{sep} parameter, the NLO QCD predictions of the inclusive dijet mass cross section in the central region of the calorimeter

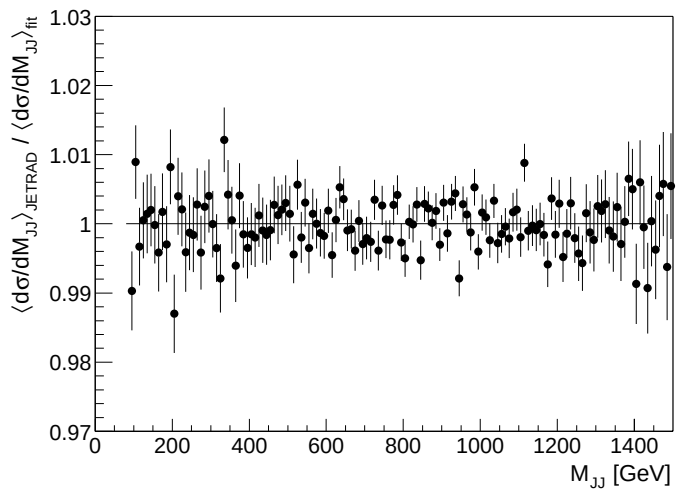

Figure 59: Ratio between the inclusive dijet mass cross section calculated directly from JETRAD and fit 73. The error bars correspond to the statistical error claimed by JETRAD.

are computed for several values of R_{sep}. The ratios of the dijet mass cross sections to the cross section calculated with $R_{sep} = 1.3$ are shown in Fig. 60. Again, the renormalization scale μ_R and factorization scale μ_F were set to $\mu_R = \mu_F = 0.5p_T^{max}$. We can conclude from the plot that the error on the theoretical prediction connected with the uncertainty on the R_{sep} parameter is about 4%.

Another source of uncertainty comes from a selection of renormalization and factorization scales. Observable quantities, like cross sections, do not depend on those two scales if all terms in the perturbative expansion are summed. However, this is not true if the sum is truncated at particular order of α_S. Fig. 61 shows relative differences between NLO calculations of the central inclusive dijet mass cross section for several settings of renormalization and factorization scales and the cross section calculated using nominal values $\mu_F = \mu_R = 0.5p_T^{jet1}$. The uncertainty of the theoretical NLO prediction of the inclusive dijet mass cross section at 1 TeV is roughly $20 - 30\%$.

The CTEQ6.0M set of PDFs also allows us to compute the error on dijet

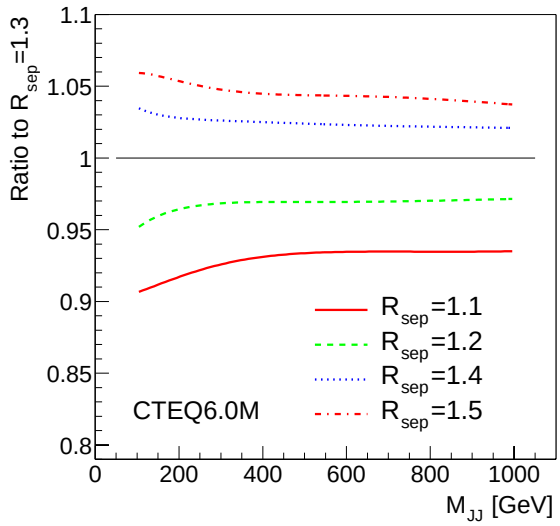

Figure 60: Ratio of NLO QCD predictions of the inclusive dijet mass cross section in the central region of calorimeter ($|y_{jet}| < 0.5$) for different values of R_{sep} to NLO QCD prediction for $R_{sep} = 1.3$.

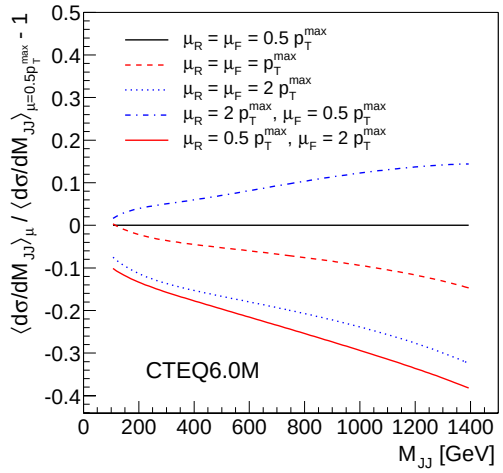

Figure 61: Relative difference between NLO prediction of the central dijet mass cross section ($|y_{jet}| < 0.5$) for several settings of renormalization and factorization scales.

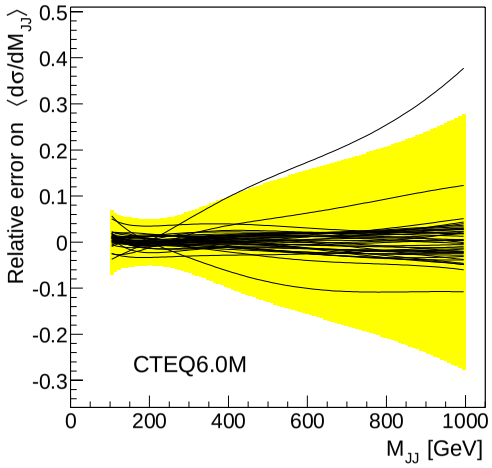

Figure 62: Relative error on dijet mass cross section ($|y_{jet}| < 0.5$) coming from the PDF uncertainties. Solid lines correspond to the cross sections calculated using the 40 sets of PDFs from CTEQ6.0M. Shaded region is the error on cross section calculated according to Eq. 7.

mass cross section connected with the uncertainty of the global fit of PDFs. The error, calculated according to Eq. 7, is displayed on Fig. 62 as a shaded region. It is about 5% in the low mass end and 25% at mass of 1000 GeV.

11.7 Comparison with theory

Relative differences between the measured inclusive dijet mass cross section and the theoretical prediction are given in Fig. 63 in the case of CTEQ6.0M and MRST2001 [30] parton distribution functions.

In both cases, the theory is in agreement with the data. Prediction based on MRST2001 agrees with the data better than prediction based on CTEQ6M. However, it is hard to make a quantitative statement about which distribution function is preferred by the data due to large systematic errors coming from the error on jet energy scale.

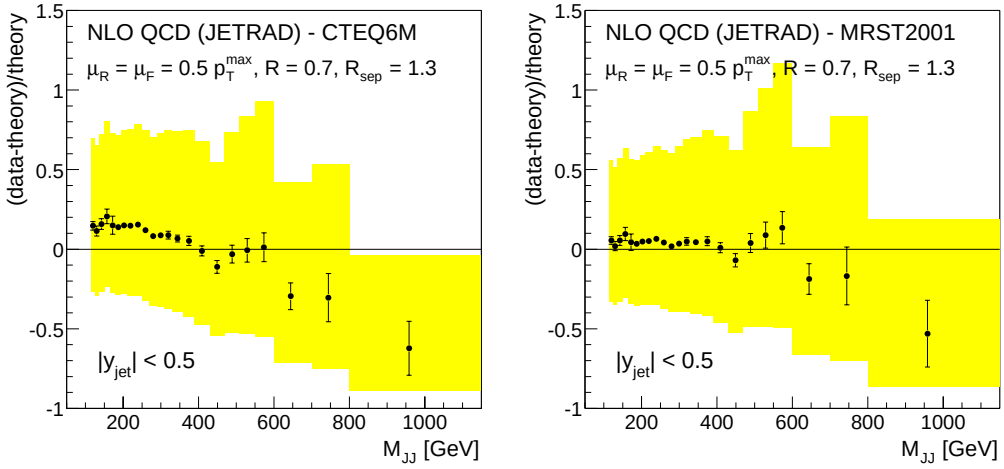

(a) (b)

Figure 63: Relative differences between the measured dijet mass cross section and NLO theoretical predictions for CTEQ6M (a) and MRST2001 (b) parton distribution functions. The errors are statistical only. The shaded regions represent overall systematic error except the additional 10% uncertainty in the normalisation.

12 $\Delta\phi$ distribution

There are many interesting distributions that can be studied on the inclusive dijet sample, not just the dijet mass cross section. For instance, the dijet angular distribution [3] or the 2-dimensional dijet thrust distribution [65] (publication in preparation) were studied in the DØ Run I data. Another interesting property of the two leading jets is their anti-correlation in the azimuthal angle ϕ. Preliminary results on measurement of the difference between azimuthal angles of the two leading jets $\Delta\phi = |\phi_1 - \phi_2|$ are presented in this section. As will follow from the discussion, understanding the multi-jet final states is important for the theoretical description of the $\Delta\phi$ distribution. Either at $\Delta\phi \sim \pi$, where the resummation of soft gluon emission is needed, or at $\Delta\phi < 2\pi/3$, where at least 4 partons are required in order to produce such a small difference in ϕ.

The $\Delta\phi$ distribution for events from the dijet sample is presented in Fig. 64. The event selection is exactly the same as in the case of the inclusive dijet mass spectrum. The $\Delta\phi$ distribution is given for four dijet mass intervals which correspond to the fully efficient mass intervals of four jet triggers as listed in Tab. 13. It means that exactly the same events enter the plot as in the case of the dijet mass spectrum. The data are normalised by the overall luminosity collected in the particular jet trigger (see Tab. 4). The data are not fully corrected. Jet energy scale together with efficiencies of the event selection criteria are applied but no unfolding procedure is performed. For this, we need to rely on full Monte Carlo simulations of the DØ detector. The angular resolution was studied in current MC in the section 10.2. However, there is still a discrepancy in jet p_T resolutions between MC and data which is still not understood. We don't have enough confidence that angular resolution is the same in the data and current MC.

JETRAD prediction is overlaid with the data in Fig. 64. It was calculated using CTEQ6.0M parton distribution function. Factorization and renormalization scales were set to $\mu_R = \mu_F = 0.5 p_T^{max}$ and the R_{sep} parameter was set to 1.3. The first non trivial description of the $\Delta\phi$ distribution is provided by

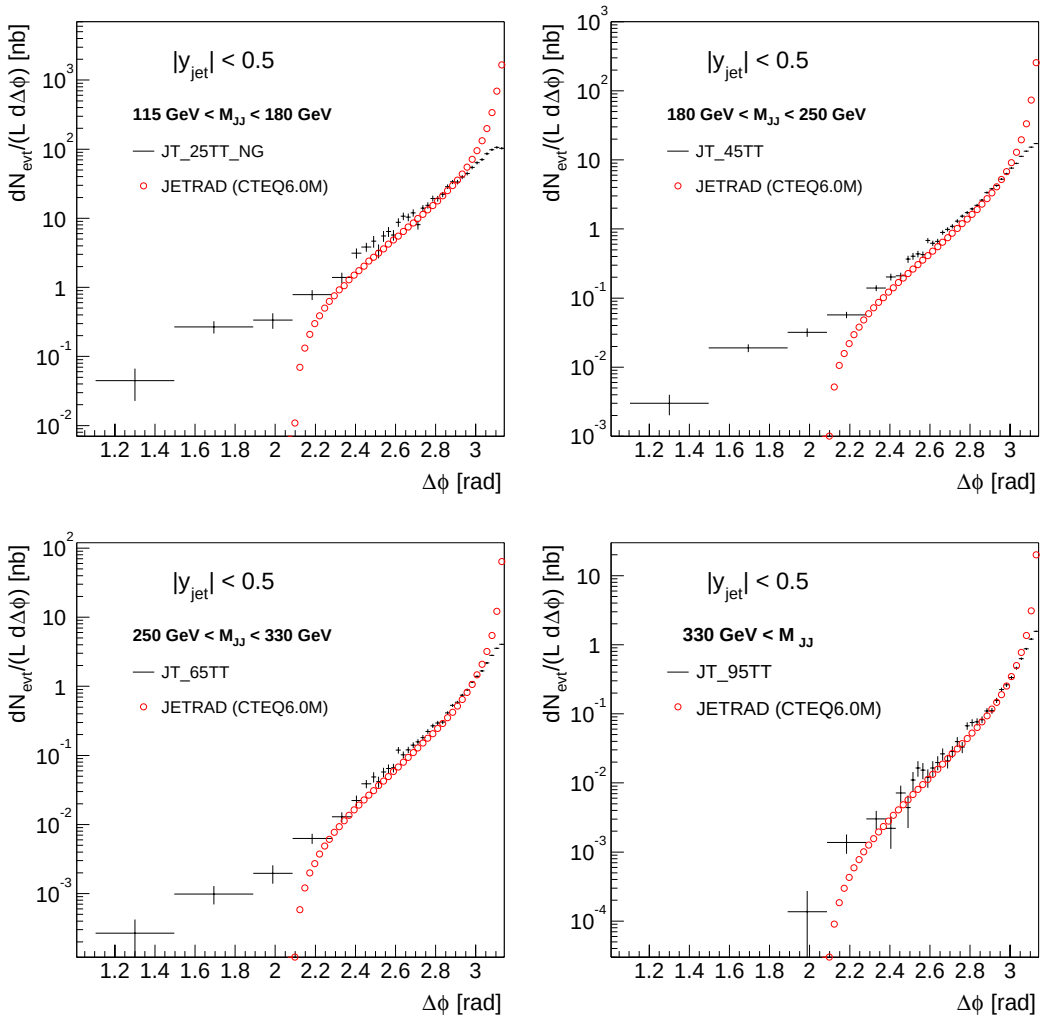

Figure 64: Raw, partially corrected, $\Delta\phi$ distribution for the central dijet sample for a cone size of $R = 0.7$. The error bars correspond to the statistical errors only. JETRAD prediction (open circles) is calculated using CTEQ6.0M PDF with factorization and renormalization scales set to $\mu_F = \mu_R = 0.5 p_T^{max}$ and with $R_{sep} = 1.3$.

LO $2 \to 3$ partons matrix element. JETRAD calculates NLO cross section for the 2-jet production. It therefore contains this LO $2 \to 3$ matrix element. JETRAD thus provide the LO description of the $\Delta\phi$ distribution.

JETRAD fails to describe the data in the two regions: $\Delta\phi \sim \pi$ and $\Delta\phi < 2\pi/3$. The discrepancy in the $\Delta\phi \sim \pi$ region is connected with the divergence of the LO $2 \to 3$ cross section in case one of the partons is soft or collinear with another one. The $\Delta\phi$ distribution is not sensitive to the collinear emission because such partons still belongs to the same jets. On the other hand, it is sensitive to the soft radiation that can occur even at large angles. In order to provide theoretical description of the $\Delta\phi$ distribution in this region, the resummation of soft parton radiation needs to be performed. The other region in which the LO $2 \to 3$ calculation fails to describe the data at all is $\Delta\phi < 2\pi/3$. Simply because it is not possible to create an event with $\Delta\phi < 2\pi/3$ with only three partons in the final state. LO $2 \to 4$ partons calculations are required to describe the $\Delta\phi$ distribution for $\Delta\phi < 2\pi/3$.

From this point of view, the $\Delta\phi$ distribution is similar to 2-dimensional jet thrust distributions that was studied in Run I data [65]. Thrust T is one of the standard event shape variables. In case of e^+e^- interactions, it is defined as

$$T = \max_{|\vec{n}|=1} \frac{\sum_i |\vec{p}_i.\vec{n}|}{\sum_i |\vec{p}_i|}\,, \tag{74}$$

where direction $\vec{n}$ maximises the ratio on the right side and $\vec{p}_i$ is a momentum of i-th particle. Thrust characterises the sphericity of the event; pencil-like events have $T \sim 1$, while events with isotropic distribution of particles have $T = 1/2$.

In the busy proton anti-proton collider environment, the particles are exchanged by jets. Also, instead of momenta only 2-dimensional jet transverse momenta are considered due to Lorentz boost of interacting parton-parton CMS along the beam. The Run I analysis introduces 2-jet thrust

$$T_2^T = \max_{|\vec{n}|=1} \frac{\sum_{jet=1,2} |\vec{p}_{\perp jet}.\vec{n}|}{\sum_{jet=1,2} |\vec{p}_{\perp jet}|}\,. \tag{75}$$

As in the case of the $\Delta\phi$ distribution, the fixed order calculations diverge as

$T_2^T \to 1$. Resummation of soft and collinear parton radiation is needed in order to provide the description of the data in this region. Three partons final states cannot yield $T_2^T < \sqrt{3}/2$. Again $2 \to 4$ matrix element is needed to describe this region. Thrust T_2^T is similar to $\Delta\phi$ but not exactly the same. Calculation of T_2^T requires knowledge of JES because jet transverse momenta enter explicitly the formula. Although, the dependence on JES and JES error is eliminated because the jet momenta are also in the denominator. On the other hand, JES affects the $\Delta\phi$ calculation only implicitly through the cut on dijet mass and through the jet ordering.

13 Summary

The first part of the thesis concerns the measurement of the jet transverse momentum resolution using the dijet p_T imbalance. The result serves as an input for determination of the dijet mass resolution and for unfolding the detector smearing from the measured dijet mass cross section. It is also used in other DØ analyses, like in the measurement of inclusive jet p_T cross section [66]. The method does not require a full Monte Carlo simulation of the DØ detector. The measured resolution can be therefore used to test the correspondence between the detector simulations and data. This analysis shows that there is a significant discrepancy between current MC resolution and resolution in data.

The measurement of inclusive dijet mass cross in $p\bar{p}$ collisions at $\sqrt{s} = 1.96\,\text{TeV}$ was presented in this analysis. It was performed on $48.0\,\text{pb}^{-1}$ of DØ Run II data for jets in the central region of the calorimeter ($|y_{jet}| < 0.5$). The cross section drops by about six orders of magnitude from mass of 115 GeV to $\sim 1000\,\text{GeV}$. The results are in good agreement with NLO QCD predictions based on CTEQ6.0M and MRST2001 parton distribution functions.

It is the first measurement of the dijet mass cross section using DØ Run II data. Compared to the former DØ Run I results [64], the lower range of dijet mass was extended from 150 GeV down to 115 GeV. However, the results presented in this analysis do not reach the Run I precision yet. The dominant contribution to the error comes from the error on jet energy scale.

Another distribution that was studied in the central dijet sample was the difference in azimuthal angle $\Delta\phi$ between two leading jets. This measurement was not made by the DØ collaboration in Run I. Preliminary measurements, not corrected for the detector smearing, of the $\Delta\phi$ distribution in four different mass bins were presented. It was shown that pQCD predictions of the order of $\mathcal{O}(\alpha_S^3)$ completely fail to describe the $\Delta\phi$ distribution in regions $\Delta\phi \sim \pi$ and $\Delta\phi < 2\pi/3$.

References

[1] H. L. Lai *et al.*, Phys. Rev. **D55**, 1280 (1997), hep-ph/9606399.

[2] CDF Collaboration, F. Abe *et al.*, Phys. Rev. Lett. **77**, 438 (1996), hep-ex/9601008.

[3] DØ Collaboration, B. Abbott *et al.*, Phys. Rev. Lett. **80**, 666 (1998), hep-ex/9707016.

[4] DØ Collaboration, B. Abbott *et al.*, Phys. Rev. Lett. **82**, 2457 (1999), hep-ex/9807014.

[5] CDF Collaboration, F. Abe *et al.*, Phys. Rev. Lett. **77**, 5336 (1996), hep-ex/9609011.

[6] UA2 Collaboration, J. Alitti *et al.*, Nucl. Phys. **B400**, 3 (1993).

[7] CDF Collaboration, F. Abe *et al.*, Phys. Rev. **D55**, 5263 (1997), hep-ex/9702004.

[8] C. L. Hebert, Search for new particles decaying to two - jets with the DØ detector, FERMILAB-THESIS-2003-06, 2003, Paper in preparation.

[9] W. T. Giele, E. W. N. Glover, and D. A. Kosower, Nucl. Phys. **B403**, 633 (1993), hep-ph/9302225.

[10] J. Pumplin *et al.*, JHEP **07**, 012 (2002), hep-ph/0201195.

[11] J. Chýla, Quarks, partons and Quantum Chromodynamics, Study text. Available at http://www-hep.fzu.cz/Theory/notes/text.pdf, 2003.

[12] J. Hořejší, Historie standartního modelu mikrosvěta., Study text. Available at http://www-hep.fzu.cz/Centrum/smodel/smodel.ps.gz, 2003.

[13] G. Zweig, An SU(3) model for strong interaction symmetry and its breaking, CERN preprint 8419/TH.412, 1964.

[14] M. Gell-Mann, Phys. Lett. **B8**, 214 (1964).

[15] M. Greenberg, Phys. Rev. Lett. **13**, 598 (1964).

[16] Y. Nambu, in Proc. Second Coral Gables Conference on Symmetry Principles at High Energy, University of Miami, 1965.

[17] Y. Nambu, in Perludes in theoretical physics, eds. A. de-Shalit, H. Heschbach, and L. van Hove, North Holland, Amsterdam, 1965.

[18] E. D. Bloom *et al.*, Phys. Rev. Lett. **23**, 930 (1969).

[19] M. Breidenbach *et al.*, Phys. Rev. Lett. **23**, 935 (1969).

[20] D. J. Gross and F. Wilczek, Phys. Rev. Lett. **30**, 1343 (1973).

[21] H. D. Politzer, Phys. Rev. Lett. **30**, 1346 (1973).

[22] D. J. Gross and F. Wilczek, Phys. Rev. **D8**, 3633 (1973).

[23] S. Bethke, α_S 2002, E-print, hep-ex/0211012, 2002, hep-ex/0211012.

[24] R. D. Field, *Applications of Perturbative QCD* , Redwood City, USA: Addison-Wesley (1989) 366 p. (Frontiers in physics, 77).

[25] W. T. Giele and E. W. N. Glover, Phys. Rev. **D46**, 1980 (1992).

[26] T. Sjöstrand, Comput. Phys. Commun. **82**, 74 (1994).

[27] T. Sjöstrand *et al.*, Comput. Phys. Commun. **135**, 238 (2001), hep-ph/0010017.

[28] G. Corcella *et al.*, JHEP **01**, 010 (2001), hep-ph/0011363.

[29] H. Baer, F. E. Paige, S. D. Protopopescu, and X. Tata, ISAJET 7.48: A Monte Carlo event generator for pp, p$\bar{\text{p}}$, and e^+e^- reactions, E-print, hep-ph/0001086, 1999, hep-ph/0001086.

[30] A. D. Martin, R. G. Roberts, W. J. Stirling, and R. S. Thorne, Eur. Phys. J. **C23**, 73 (2002), hep-ph/0110215.

[31] DØ Collaboration, S. Abachi *et al.*, Nucl. Instrum. Meth. **A338**, 185 (1994).

[32] DØ Collaboration, B. Abbott *et al.*, Nucl. Instrum. Meth. **A424**, 352 (1999), hep-ex/9805009.

[33] D. Schamberger, Calorimeter Electronics Upgrade, DØ Note 1116, 1991.

[34] D. Schamberger *et al.*, Calorimeter Electronics Upgrade for Run 2. Technical design report, text is available at *http://www-d0.fnal.gov/~d0upgrad/calelec/intro/tdr/tdr17.pdf*, 1998.

[35] G. Bernardi, B. Olivier, B. Knuteson, and M. Strovink, NADA: A New Event by Event Hot Cell Killer, DØ Note 3687, 1999.

[36] G. Bernardi and S. Trincaz-Duvoid, Improvement of the NADA Algorithm: Hot Cell Killing in DØ Run II Data, DØ Note 4057, 2002.

[37] J. Huth *et al.*, Report of the QCD and standard model working group, in *Proceedings of Research Directions For The Decade: Snowmass 1990*, p. p. 134, World Scientific, Singapore, 1992, 1990.

[38] S. D. Ellis, Z. Kunszt, and D. E. Soper, Phys. Rev. Lett. **69**, 3615 (1992), hep-ph/9208249.

[39] DØ Collaboration, V. M. Abazov *et al.*, Phys. Lett. **B525**, 211 (2002), hep-ex/0109041.

[40] DØ Collaboration, V. M. Abazov *et al.*, Phys. Rev. **D65**, 052008 (2002), hep-ex/0108054.

[41] S. Catani, Y. L. Dokshitzer, M. H. Seymour, and B. R. Webber, Nucl. Phys. **B406**, 187 (1993).

[42] S. Catani, Y. L. Dokshitzer, and B. R. Webber, Phys. Lett. **B285**, 291 (1992).

[43] S. D. Ellis and D. E. Soper, Phys. Rev. **D48**, 3160 (1993), hep-ph/9305266.

[44] G. C. Blazey *et al.*, Run II jet physics, E-print, hep-ex/0005012, 2000, hep-ex/0005012.

[45] C. Catani *et al.*, Report of the QCD and standard model working group, for the Workshop *Physics at TeV Colliders*, Les Houches, France, 1999.

[46] W. Giele *et al.*, The QCD/SM working group: Summary report, E-print, hep-ph/0204316, 2002, hep-ph/0204316.

[47] M. H. Seymour, Nucl. Phys. **B513**, 269 (1998), hep-ph/9707338.

[48] B. Abbott, M. Bhattacharjee, D. Elvira, F. Nang, and H. Weerts, Fixed Cone Jet Definitions in DØ and R_{sep}, DØ Note 2885, 1996.

[49] J. Coss *et al.*, Jet Energy Scale and Resolution for p13 Data and Monte Carlo, DØ Note 4115, 2003.

[50] M. Begel *et al.*, DØ Luminosity in Run 2 : Delivered, DØ Note 3970, 2003.

[51] M. Begel *et al.*, DØ Luminosity in Run 2 : Triggered, DØ Note 3971, 2003.

[52] M. Begel, DØ Luminosity in Run 2 : Recorded, DØ Note 3972, 2003.

[53] M. Begel *et al.*, Luminosity and Performance of DØ during the First Year of Run 2, DØ Note 3973, 2002.

[54] V. White *et al.*, The DØ data handling system, Prepared for CHEP'01: Computing in High-Energy Physics and Nuclear, Beijing, China, 3-7 Sep 2001.

[55] A. Kupčo *et al.*, Accessing Triggered Luminosity Information via Flat Files, DØ Note 3969, 2003.

[56] H. Schellman *et al.*, User Interface to Find the Luminosity Blocks Corresponding to Data Files, DØ Note 3937, 2003.

[57] E710 Collaboration, N. A. Amos *et al.*, Phys. Lett. **B243**, 158 (1990).

[58] CDF Collaboration, F. Abe *et al.*, Phys. Rev. **D50**, 5550 (1994).

[59] E811 Collaboration, C. Avila *et al.*, Phys. Lett. **B445**, 419 (1999).

[60] M. Begel, Private communication.

[61] A. Kupčo, P. Demine, C. Royon, and M. Zieliński, Measurement of the dijet mass cross section, DØ Note 4145, 2003.

[62] G. Bernardi *et al.*, Jets in Run II, DØ Note 3985, 2002.

[63] DØ Collaboration, B. Abbott *et al.*, Phys. Rev. Lett. **86**, 1707 (2001), hep-ex/0011036.

[64] DØ Collaboration, B. Abbott *et al.*, Phys. Rev. **D64**, 032003 (2001), hep-ex/0012046.

[65] V. Sorin, D. Elvira, and R. Piegaia, Measurement of Dijet Transverse Thrust cross sections, DØ Note 3920, 2001.

[66] G. A. Davis *et al.*, First D0 Measurement of the Inclusive Jet Cross Section in RunII, DØ Note 4157, 2003.